SYNTHESIS OF CARBON DOTS FROM POLYURETHANE AND NATURAL RUBBER FOR METAL ION SENSING AND ENERGY STORAGE APPLICATION

BY

KULPRIYA PHETCHAREE

A DISSERTATION SUBMITTED IN PARTIAL FULFILLMENT
OF THE REQUIREMENTS FOR THE DEGREE OF
DOCTOR OF PHILOSOPHY (CHEMISTRY)
DEPARTMENT OF CHEMISTRY
FACULTY OF SCIENCE AND TECHNOLOGY
THAMMASAT UNIVERSITY
ACADEMIC YEAR 2021

THAMMASAT UNIVERSITY
FACULTY OF SCIENCE AND TECHNOLOGY

DISSERTATION

BY

KULPRIYA PHETCHAREE

ENTITLED

SYNTHESIS OF CARBON DOTS FROM POLYURETHANE AND NATURAL RUBBER FOR METAL ION SENSING AND ENERGY STORAGE APPLICATION

was approved as partial fulfillment of the requirements for the degree of Doctor of Philosophy (Chemistry)

on June 28 , 2022

Chairman _____
(Panichakorn Jaiyong, Ph.D.)

Member and Advisor _____
(Associate Professor Peerasak Paoprasert, Ph.D.)

Member and Co-adviser _____
(Jedsada Manyam, Ph.D.)

Member _____
(Natee Sirisit, Ph.D.)

Member _____
(Chalathorn Chanthad, Ph.D.)

Dean _____
(Associate Professor Nuttanont Hongwarittorrn, Ph.D.)

Dissertation Title	SYNTHESIS OF CARBON DOTS FROM POLYURETHANE AND NATURAL RUBBER FOR METAL ION SENSING AND ENERGY STORAGE APPLICATION
Author	Kulpriya Phetcharee
Degree	Doctor of Philosophy (Chemistry)
Department/Faculty/University	Chemistry Faculty of Science and Technology Thammasat University
Dissertation Advisor	Associate Professor Peerasak Paoprasert
Dissertation Co-Advisor	Jedsada Manyam, Ph.D.
Academic Year	2021

ABSTRACT

Carbon dots are a new class of carbon-based materials, having interesting chemical, physical and biological properties. Due to these unique properties, they have been used in many applications, for example, bio-imaging probes, drug and gene delivery, sensors, fluorescent ink, optoelectronic devices, and photocatalysis. In this thesis, the carbon dots were synthesized through pyrolysis and hydrothermal methods from polyurethane and natural rubber as carbon-based precursors. The prepared carbon dots from polyurethane and natural rubber were used for metal ion sensing because of their selective binding ability with selected metal ions. In addition, the carbon dots will be applied for supercapacitor application. Zinc oxide is a metal oxide that is a promising candidate as the electrode of supercapacitors via redox reaction and Faradaic processes. However, it still has the shortcomings of poor performance because of its slow faradic reaction and low electron transportability at high current. The carbon dots are pseudo-capacitive materials because of the presence of heteroatoms whereas zinc oxide can generate oxygen-containing groups to enhance the charge storage by redox reactions. Moreover, carbon dots were modified using gamma irradiation in the presence of ethylenediamine to introduce surface passivation by ammonium groups in the carbon dot structure. Therefore, the gamma-irradiated carbon dots and zinc oxide will be used to

fabricate the composite electrodes in order to improve performances in supercapacitors. In summary, this thesis will demonstrate the versatility of carbon dots and their unique properties in various applications.

Keywords: Carbon dots, Polyurethane, Natural rubber, Hydrothermal, Pyrolysis, Zinc oxide, Metal ion sensing, Supercapacitors

ACKNOWLEDGEMENTS

Undertaking this Ph.D. has been a truly life-changing experience for me and I would like to take this opportunity to acknowledge and record the roles of several individuals who were instrumental in the completion of my Ph.D. journey.

I would like to express my deepest appreciation to my advisor, Associate Professor Dr.Peerasak Paoprasert, who expertly guided me through my Ph.D. research. His dedication and keen interest to help his students had mainly responsible for completing my work. Without his participation, meaningful assistance, constant help, and scientific approach, this dissertation would not have been possible.

I thank profusely all the committee members, Dr.Panichakorn Jaiyong, Dr.Natee Sirisit, Dr.Jedsada Manyum, and Dr.Chalathorn Chanthad, for letting my defense be an enjoyable moment and for their brilliant comments and suggestions. I also thank all members in the Department of Chemistry, Thammasat University for giving me valuable knowledge and rewarding experiences.

This study would not have been possible without the financial support from the Thailand Graduate Institute of Science and Technology (TGIST: SCA-CO-2559-2322-TH), National Science and Technology Development Agency (NSTDA). I am also thankful to the Department of Chemistry, Thammasat University for all facilities and instrumentation for advanced research.

Lastly, my thanks also go to my family, my friends, and lab member colleagues who have always supported me through every step of this journey.

Kulpriya Phetcharee

TABLE OF CONTENTS

LIST OF TABLES

LIST OF FIGURES

LIST OF ABBREVIATIONS

Symbols/Abbreviations	Terms
ω	Angular frequency
η	Refractive index
Φ	Quantum yield
Ґ	Surface coverage
Ω	Ohm
Ω·cm	Ohm centimeter
μL	Microliter(s)
μM	Micromolar
°	Degree
°C	Degree Celsius
°C·min^{-1}	Degree Celsius per minute
A	Electrode area
Å	Angstrom
C^0	Bulk concentration of analyte
C*	Concentration of electrolyte
cm^{-1}	Reciprocal centimeter
cm^2	Square centimeter
CDs	Carbon dots
CV	Cyclic voltammetry
Cs	Specific capacitance
D_o	Diffusion coefficient
DI water	Deionized water
DLS	Dynamic light scattering
EtOH	Ethanol
EXAFS	X-ray absorption fine structure
eV	Electronvolt
F	Faraday’s constant

Symbols/Abbreviations	Terms
FT-IR	Fourier transform infraredGram
G	Gram per liter
$g \cdot L^{-1}$	Graphene quantum dots
GQDs	Hour(s)
h	Nitric acid
HNO_3	Sulfuric acid
H_2SO_4	Inner filter effect
IFE	Peak current
I_p	Imaginary unit
j	Degree kelvin
K	Electron-transfer rate constant
k_o	Kilodalton
kDa	Limit of detection
LOD	Linear sweep voltammetry
LSV	Molar
M	Milligram per liter
$mg \cdot L^{-1}$	Minute(s)
min	Milliliter
mL	Millimolar
mM	Molecular weight cut-off
MWCO	Sodium hydroxide
NaOH	Nanometer
nm	Nanomolar
nM	Potential of hydrogen
pH	Photoluminescence
PL	Platinum
Pt	Poly(vinylidene fluoride)
PVDF	Quinine sulfate
QS	

Symbols/Abbreviations	Terms
	Ethylenediamine
EDA	Equivalent series resistance
ESR	Second
Sec	Time
t	Temperature
T	Transmission electron microscopy
TEM	Ultraviolet
UV	Voltage
V	Volume by volume
v/v	Watt
W	Weight percent
wt%	X-ray photoelectron spectroscopy
XPS	X-ray absorption near edge structure
XANES	Zinc oxide
ZnO	

CHAPTER 1
INTRODUCTION

1.1 Metal ion contamination

Heavy metal ions are widely existed in the industry, agriculture, and other areas. Due to the existence of the food chain, they can easily enter the human body. Thus, the contamination of heavy metal ions in the environment and water resources is extremely harmful to the environment and human health [1]. It would induce various diseases by damaging the organs like the liver, kidneys, bones, and teeth [2, 3]. Thus, it is of importance to develop a simple, fast, sensitive, and low-cost methodology that could analyze and simultaneously identify heavy metal ions. There are many techniques that can be used in the field for analyzing heavy metal ions, including atomic absorption spectroscopy [4] and inductively coupled plasma atomic emission spectroscopy [5], etc. Although these methods can detect metal ions with excellent sensitivity and selectivity, they still have some disadvantages, such as tedious sample preparation, high cost and large size of the instrument, and the requirement of specially trained users, which limit their applications in heavy metal ions detection.

Colorimetric method is also commonly used for metal ion sensing [6], but its sensitivity is usually not enough to investigate the contamination of heavy metals in real applications [7]. Compared with those methods, fluorescence sensing has the advantages of high sensitivity and simple operation. It becomes a popular method in the field of metal ion analysis [8]. Therefore, the development of alternative charming candidates based on fluorescence sensing with excellent sensitivity, selectivity, and ease of use is highly needed.

1.2 Energy shortage

The demand for fossil fuels (coal, petroleum, and natural gas) has continuously increased with the fast growth and development of the global economy. The need for total equivalent oils in the world was estimated to be around 13.7 billion

tons as of 2012 and will increase up to around 18 billion tons by 2035 according to the statistical report [9]. The depletion of fossil fuels and the occurrence global warming have already caused economic and environmental crisis, such as price fluctuations and unbalanced supply chains, resulting in intense research activity for the exploitation of environmental-friendly and limitless energy sources. Therefore, developing sustainable energy supplies and storage technologies can be achieved to overcome these problems. Recently, energy storage devices, such as supercapacitors, have received attention in various aspects, including renewable energy production plants, transportation, portable tools, and information storage systems [10]. However, the applications of energy storage devices are limited by the lack of appropriate electrodes with excellent electrochemical performance. Therefore, the creation and development of high-performing electrode materials are significant to boost the practicality of energy storage devices [11].

1.3 Carbon dots

Nanomaterials have experienced booming in scientific, technological, and commercial applications. For example, quantum dots are interesting nanomaterials having unique electrical and optical properties such as bright photoluminescence and size-dependent optoelectronic properties [12]. Quantum dots are normally composed of elements from groups III-V, II-VI, or IV-VI of the periodic table, such as cadmium and lead [13]. They have excellent fluorescence properties and are widely used in sensing applications. Due to their toxicity from toxic metals, it limits quantum dots for use as sensors for practical uses [14]. Graphene is a two-dimensional (2D) flat material that consists of monolayer carbon atoms. It possesses properties as for a range of thermal and mechanical properties and electrical conductivity [15]. However, graphene still showed toxic effects both *in vitro* and *in vivo*[16]. Carbon nanotubes (CNTs) are carbon-based nanomaterials with diameters ranging between 0.5–100 nm [17]. Although they have received attention in various fields from electronics, engineering, and medicine, they must be functionalized with the biocompatible surface coating to reduce the toxic effect in *in-vivo* [18].

Carbon dots, also known as carbon nanodots or carbon quantum dots, are a new class of carbon-based materials that were discovered via an accidental discovery during the separation and purification of SWCNTs from carbon soot by Xiaoyou Xu and co-workers in 2004 [19]. They are zero-dimensional carbon nanoparticles with a size less than 20 nm [20]. They consist of a combination of graphitic and disordered carbons and a high percentages of oxygen [21]. They offer interesting and unique properties, including photophysical properties, high photoluminescence, high photostability, high water solubility, low toxicity, and facile surface adsorption and binding [22-24]. Due to their beneficial properties, carbon dots have been considered to be promising candidates to solve the problem of toxic nanomaterials. Due to these advantages of carbon dots, they have been used in many applications such as optoelectronic devices [25], bio-imaging [26], sensors [27], drug delivery [28], and supercapacitors [29]. Furthermore, carbon dots can be synthesized from a number of materials that contain a high percentage of carbon. Many carbon-based materials were used as precursors for the synthesis of carbon dots in previous studies such as glucose [30], graphene [31], graphite [32], single-walled or multi-walled carbon fibers [33], candle soot [34], carbon nanotubes [35]. Carbon dots can be prepared through top-down and bottom-up methods. In the top-down route, carbon dots can be formed by breaking large carbon-rich materials. While in the bottom-up method, carbon dots were generated from small molecules under the thermal treatment.

In this study, we will synthesize highly fluorescent carbon dots from abundantly available and low-cost material that are polyurethane and natural rubber as precursors and explore their metal ion sensing and energy storage applications. Polyurethane and natural rubber are ones of the most important polymers used in daily life. Hence, their recycling has been of great interest. Carbon dots will be prepared using pyrolysis and hydrothermal methods to obtain the optimum conditions in terms of high product yields and high quantum yields. The structural and optical properties of carbon dots will be examined by routine characterization techniques. The obtained carbon dots will be applied in metal ion sensing and energy storage applications because of their properties including excellent binding ability with metal ion and pseudo-capacitive properties, respectively.

1.4 Research objectives

1.4.1 To synthesize carbon dots from polymers, including polyurethane and natural rubber.

1.4.2 To characterize properties of the resulting carbon dots.

1.4.3 To modify carbon dots derived from polyurethane using gamma irradiation.

1.4.4 To characterize properties of the gamma-irradiated carbon dots.

1.4.5 To apply carbon dots for the followings.

(1) Metal ion sensing

(2) Supercapacitor

1.5 Scope and limitation of the study

1.5.1 Synthesis of the carbon dots from polyurethane and natural rubber using pyrolysis and hydrothermal methods

1.5.2 Study of effects of fluorescence properties via the following parameters

(1) Type of acid

(2) Concentration of acid

(3) Reaction temperature

(4) Reaction time

1.5.3 Characterization of the resulting carbon dots

1.5.3.1 Optical properties

(1) UV-visible spectroscopy

(2) Fluorescence spectroscopy

1.5.3.2 Structure characterization

(1) Fourier transform infrared (FT-IR) spectroscopy

(2) X-ray photoelectron spectroscopy (XPS)

1.5.3.3 Size and morphology

(1) Dynamic light scattering (DLS) and zeta potential

(2) Transmission electron microscope (TEM)

CHAPTER 2
REVIEW OF LITERATURE

2.1 Carbon dots and their properties

Carbon dots, also known as carbon nanodots or carbon quantum dots, are a new class of carbon nanomaterials with a size less than 20 nm (Figure 2.2a) [36]. They are basically spherical particles with sp^2 and sp^3 hybridization as the carbon-core structure consists of hydrophilic functional groups, such as hydroxyl, carbonyl, and carboxylic acid groups (Figure 2.1). The presence of these oxygen-containing functional groups suggests the hydrophilicity of carbon dots as they are indeed highly soluble in water and aqueous solutions. Carbon dots are generally prepared using and solvothermal treatments, ultrasonication, and microwave-assisted techniques in the presence of acids as catalysts [37]. In the reaction with acid and high temperature, the raw materials are proposed to undergo dehydration, hydrolysis, polymerization, and carbonization to form the carbon dots with hydrophilic functional groups on their surfaces [38].

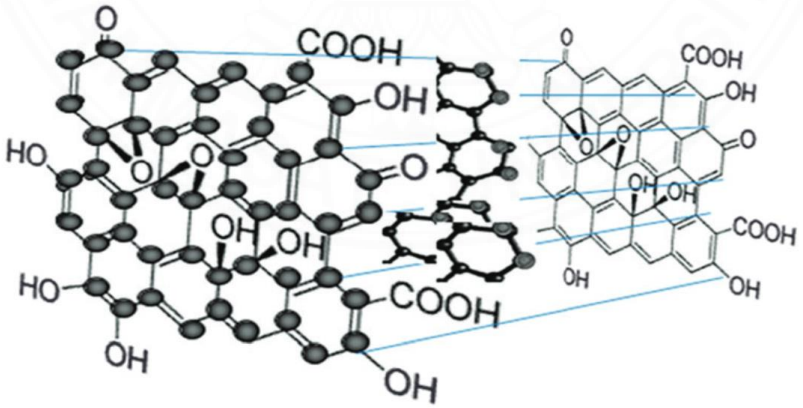

Figure 2.1 Chemical structure of carbon dots. Adapted from "Novel Fluorescent Carbonic Nanomaterials for Sensing and Imaging," by A. P. Demchenko, and M.O. Dekaliuk, 2013, *Methods and Applications in Fluorescence, 1*(4). Copyright 2013 by IOP Publishing.

Comparing with other fluorescent probes, such as organic dyes, quantum dots, and metal nanoclusters, carbon dots possess excellent properties including low cost, simple synthesis, facile functionalization, good biocompatibility, great water solubility, and low toxicity [39, 40]. They have been widely used in many applications such as biological imaging, sensing, drug delivery, photocatalytic [41]. Additionally, they have been used for effective metal ion sensors and energy storage devices because of their selective binding ability with metal ions and they can act as pseudo-capacitive materials, respectively.

Normally, the optical absorption peak of carbon dots occurs in the ultraviolet (UV) region with a tail extending to the visible range. In addition, fluorescence peak of carbon dots is commonly observed. For example, nitrogen-doped carbon dots (NCDs) obtained from using citric acid, ethylenediamine, and fluorescein as the precursors via hydrothermal method exhibited UV–visible absorption peak and strong blue fluorescence with a high fluorescence quantum yield (Figure 2b) [42].

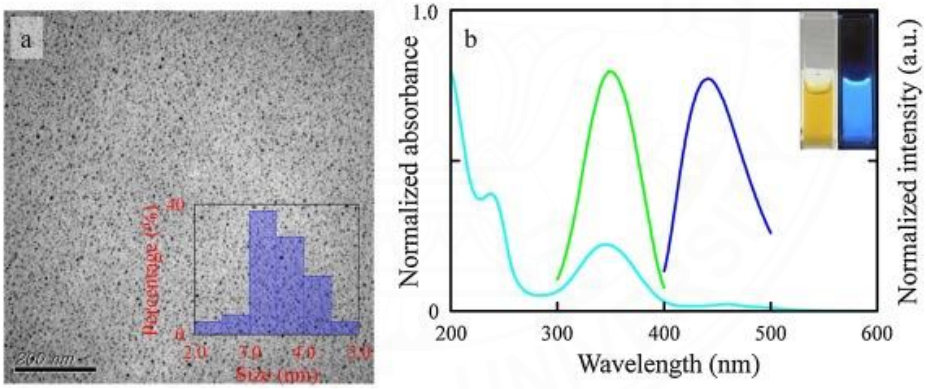

Figure 2.2 (a) TEM images, inset: size distributions of the nitrogen-doped carbon dots (NCDs) and (b) UV–visible absorption, fluorescence excitation (green), and emission (blue) spectra of the NCDs, inset: optical images under daylight (left) and a UV lamp (right). Adapted from "Highly fluorescent nitrogen-doped carbon dots for selective and sensitive detection of Hg^{2+} and ClO^- ions and fluorescent ink," by Y.-X. Li, J.-Y. Lee, H. Lee, C.-C. Hu, T.-C. Chiu, 2020, *Journal of Photochemistry and Photobiology A: Chemistry, 405*. Copyright 2020 by Elsevier.

Recently, their phosphorescence properties and chemiluminescence properties were also discovered. For example, Yehao Deng and co-workers reported that carbon dots dispersed in the polyvinyl alcohol (PVA) matrix showed clear phosphorescence under UV light (Figure 2.3) [43]. From these properties, carbon dots were used in various applications such as catalysts, sensors, information encryption, photodynamic therapy, and in-vitro and in-vivo bioimaging/biosensor. The optical absorption and photoluminescence properties of carbon dots were controlled by the surface functional groups, morphology, size, and crystalline nature of carbon dots.

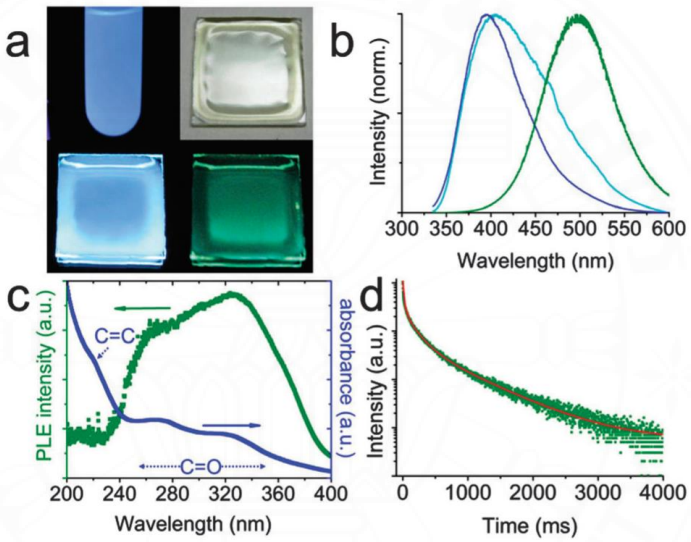

Figure 2.3 (a and b) Digital photographs and the corresponding spectra of carbon dots: dispersed in water under UV light (a: upper left; b: blue line); dispersed in the PVA matrix under daylight (upper right), UV light (a: lower left; b: cyan line) and right after UV light has been turned off (a: lower right; b: olive line). The UV excitation for the photographs is 365 nm while for the spectra it is 325 nm. (c) Phosphorescence excitation spectrum (olive dots) and absorption spectrum of carbon dots dispersed in water (blue dots). (d) Time-resolved phosphorescence spectrum. Adapted from "Long lifetime pure organic phosphorescence based on water soluble carbon dots," by Y. Deng, D. Zhao, X. Chen, F. Wang, H. Song, D. Shen, 2013, *Chemical Communications, 49*(51). Copyright 2013 by RSC Publishing.

2.2 Synthesis of carbon dots

One of the attractive aspects of carbon dots is that they can be synthesized from a number of precursors. Carbon dots were synthesized from glucose [44], sugarcane bagasse [45], banana peel waste [46], cabbage [47], red lentils [48], vitamin B1 [49], pure-solvent tetrahydrofuran [50], and citric acid [51]. The two main approaches for the synthesis of carbon dots are top-down and bottom-up as shown in Figure 2.4

.

Figure 2.4 The synthesis of carbon dots via top-down and bottom-up approaches. Adapted from "Carbon Nanodots: A Review—From the Current Understanding of the Fundamental Photophysics to the Full Control of the Optical Response," by A. Sciortino, A. Cannizzo, F. Messina, 2018, *C*, *4*(4). Copyright 2018 by MDPI.

2.2.1 Top-down approach

In top-down approach, the carbon dots can be synthesized by breaking down larger precursors such as carbon black [52] or graphene oxide [33] into carbon dots via various methods such as arc discharge[19], chemical ablation, laser ablation [32], microwave irradiation [53], and electrochemical carbonization [54].

2.2.2 Bottom-up approach

In bottom-up approach involves reassembling small molecules of carbon-based materials such as orange juice [55], chicken egg [56], citric acid [57], and glucose [30] as precursors to form larger carbon dots by applying external energy including ultrasonication [58], pyrolysis, and hydrothermal.

In comparison between two different methods, the bottom-up method is simpler, lower cost, milder condition, higher product yield, and easier to introduce heteroatoms from the precursor into carbon dots than top-down method.

2.3 Pyrolysis method

Pyrolysis is a thermal decomposition of the organic or carbon-based raw materials and conversion into carbon dots by using high temperature. At the first stage of the reaction, the temperature was over the melting point of precursors, and then these raw materials molecules underwent dehydration, condensation, carbonization, and passivation to the formation of carbon dots [59, 60]. The properties, size distribution, composition, and morphology of obtained carbon dots via pyrolysis method are dictated by material composition, temperature, heating time, and reaction time [57].

The pyrolysis method is commonly used for the preparation of carbon dots. For example, carbon dots were synthesized from fennel seeds as raw materials via pyrolysis method (Figure 2.5). Fennel seeds were crushed, transferred to the crucible cup, and heated using a heat plate at 500 °C for 3 hours. After the reaction time was completed, the crucible was allowed to cool down to room temperature and a dark-gray product was obtained. The obtained product was dissolved in deionized water followed by the sonication for 5 minutes. The black color suspension was centrifuged at 15000 rpm for 10 minutes to remove the large particles. The supernatant was filtered using 100 nm pore size filter and dialysis for further purification. The purified carbon dots was stored for further characterization [61].

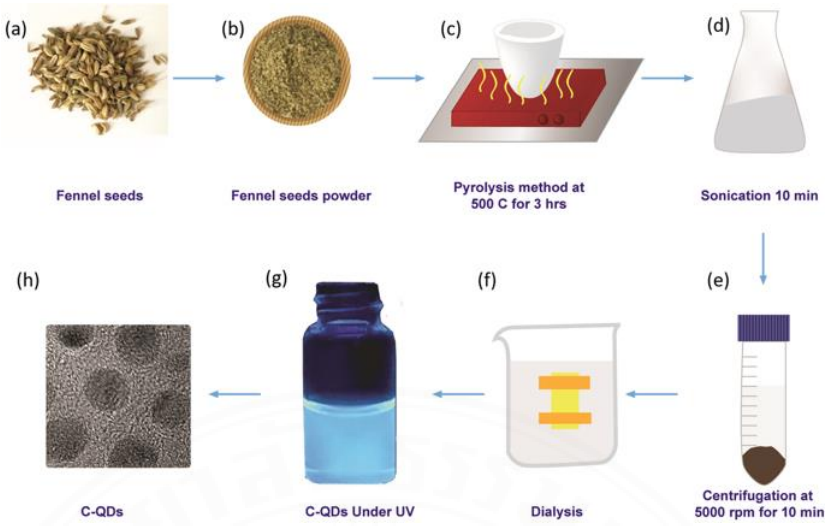

Figure 2.5 The schematic illustration shows the synthesis of carbon dots from fennel seed via pyrolysis method. (a) Fennel seeds. (b) Ground fennel powder. (c) Pyrolysis of fennel powder. (d) Sonication of carbon dots. (e) Centrifugation of carbon dots. (f) Dialysis of carbon dots. (g) Carbon dots under UV. (h) TEM image of carbon dots. Adapted from "Synthesis and characterization of Mono-disperse Carbon Quantum Dots from Fennel Seeds: Photoluminescence analysis using Machine Learning," by A. Dager, T. Uchida, T. Maekawa, M. Tachibana, 2019, *Scientific Reports, 9*(1). Copyright 2019 by Natureresearch.

2.4 Hydrothermal method

Hydrothermal method is a cheap, environmentally friendly, and non-toxic technique to synthesize novel carbon-based materials from various raw materials. This method was classified into two types which are high and low temperatures. The high-temperature hydrothermal treatment proceeds in a range of 300 to 800°C generally for organic compounds while the low-temperature hydrothermal treatment performs at below 300°C for carbon-based materials. The reaction occurs in an apparatus consisting of a steel pressure vessel, called a Teflon-lined autoclave and heating with high-pressure steam inside the reactor to generate the reaction.

Hydrothermal method is widely used for the synthesis of carbon dots. For example, carbon dots can be prepared via a one-pot hydrothermal method using cellulose fibers as a carbon-based precursor and sulfuric acid as a carbonization agent (Figure 2.6). Then, the mixture was transferred to Teflon-lined autoclave and then heated at 200^{o}C for 4 h in an oven. After cooling to room temperature, dilution, and filtration with a 0.22-μM filter membrane, the carbon dot solution was obtained. Furthermore, the prepared carbon dots are successfully applied in chemical detection with excellent selectivity and sensitivity [62].

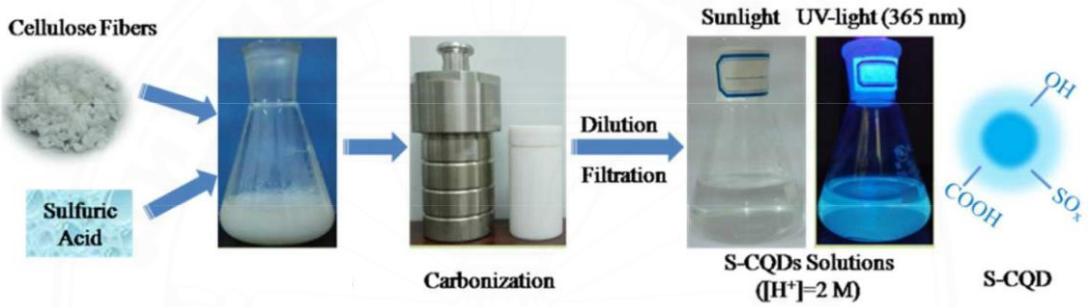

Figure 2.6 The synthesis procedure of S-doped carbon quantum dots (S-CQDs). Adapted from "Acidophilic S-doped carbon quantum dots derived from cellulose fibers and their fluorescence sensing performance for metal ions in an extremely strong acid environment," by G. Yang, X. Wan, Y. Su, X. Zeng, J. Tang, 2016, *Journal of Materials Chemistry A*. Copyright 2016 by Royal society of chemistry.

2.5 Applications of carbon dots

Because of the interesting properties of carbon dots discussed above, carbon dots have been used in several fields as follows.

2.5.1 Metal ion sensing

Carbon dots were used in many potential applications in metal ion sensing because their hydrophilic functional groups on the surface of carbon dots such as hydroxyl, carboxyl, and carbonyl groups are strong binding or chelating sites for

metal ions [63]. As a consequence, the photophysical properties of carbon dots are altered upon binding to the metal ions and can be therefore exploited as a sensing platform for the detection of metal ions in many real environment and biological samples. The examples were shown in Table 2.1.

Table 2.1

List of carbon dots as metal ions sensor

Carbon dots precursors	Metal ions sensing	References
Nanofibrillated cellulose	Cr^{3+}	[64]
Coconut coir	Cu^{2+}, Cd^{2+}	[65]
Mango	Fe^{2+}	[66]
Corncob residues	Fe^{3+}	[67]
Orange peels	Pb^{2+}, Hg^{2+}, Cu^{2+}, Ni^{2+}, Ag^{2+}, Sn^{2+}	[68]
Pineapple	Fe^{3+}	[69]
Murraya koenigii leaves	Cd^{2+}	[70]
Tomato	Fe^{3+}	[71]
Broccoli	Ag^{+}	[72]
Scallion	Cd^{2+}	[73]
Kelp	Co^{2+}	[74]
Spider silk	Hg^{2+}	[75]
Purple perilla leaves	Ag^{+}	[76]

Interestingly, in some cases of application of carbon dots as metal ion sensing, the carbon dots exhibited low selectivity and sensitivity (Figure 2.7) [68]. The orange peels-derived carbon dot as metals sensor can detect various ions including Pb^{2+}, Hg^{2+}, Cu^{2+}, Ni^{2+}, Ag^{2+}, and Sn^{2+}. Therefore, the development of alternative charming candidates with excellent sensitivity, selectivity, and ease of use is highly required.

(a)

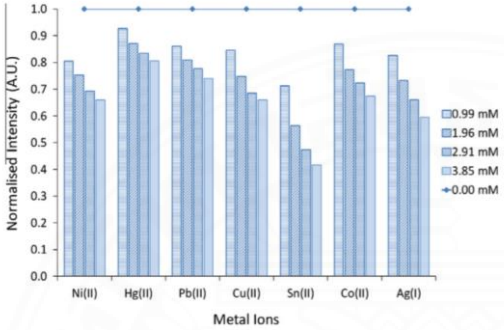

(b)

Metal ions	K_{sv} (M^{-1})	LOD (mM)
Sn(II)	365.29	0.21
Ag(I)	173.33	0.44
Cu(II)	136.43	0.56
Ni(II)	128.71	0.59
Co(II)	124.65	0.61
Pb(II)	86.08	0.89
Hg(II)	62.82	1.21

Figure 2.7 (a) The quenching effect on the carbon nanoparticles in the presence of different metal ions at various concentrations. (b) Summary of the analytical characteristics of the carbon nanoparticles with various metal ions tested in this study. Adapted from "A sustainable alternative to synthesis optical sensing receptor for the detection of metal ions," by A.N.L. Tiong, N.K.H. Wong, J.F.Y. Fong, X.W. Tan, S.M. Ng, 2015, *Optical Materials*, *40*. Copyright 2015 by Elsevier.

2.5.2 Supercapacitors

Supercapacitors, also known as electrochemical capacitors (ECs) or ultracapacitors (UC), are new types of energy storage devices. They consist of electrodes, electrolyte, and separator. Electrolytes are aqueous and non-aqueous solutions of different types of acids, bases, or salts such as sulfuric acid, potassium hydroxide, and sodium sulfate. Supercapacitors can store energy at high rates, resulting in higher power densities compared with batteries [81]. Besides, they provide fast charge-discharge times and lifetimes of a million cycles as shown in Figure 2.8 [82].

However, they have lower energy density compared with battery and their applications are limited by the lack of appropriate electrodes with excellent electrochemical performance [83, 84]. The electrode materials of supercapacitors are divided into two types. The first type is carbon materials with a high surface area, such as activated carbon [85], reduced graphene oxide [86], and carbon aerogel [87]. The second type is metal oxides and conducting polymers which are pseudocapacitive materials as they can improve the electrochemical capacity of electrodes via redox reactions or Faradaic processes [88]. Moreover, a hybrid between carbon-based materials and metal oxides has been receiving attention for supercapacitors, which are expected to generate faradic capacitance and other effects to upgrade the performances [89].

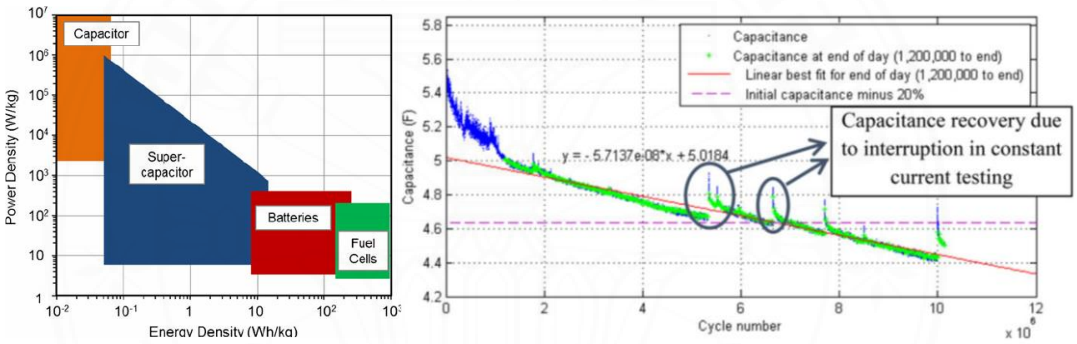

Figure 2.8 (a) Power density against energy density, also called a Ragone plot, for various energy storage and conversion devices. (b) Capacitance versus cycle number during cycle lifetime testing at 25°C. Adapted from "A flexible super-capacitive solid-state power supply for miniature implantable medical devices," by C. Meng, O.Z. Gall, P.P. Irazoqui, 2013, *Biomedical microdevices*, *15*(6). Copyright 2013 by Springer.

2.6 Enhanced the electrochemical performance of energy storage applications

2.6.1 Carbon dots

In recent years, many studies applied carbon dots in supercapacitors applications. Haipeng Lv and co-workers synthesized carbon dot-induced MnO_2 nanowire and utilized as a supercapacitor electrode materials to enhance supercapacitor

performance [90]. The MnO_2 membrane is a hydrophilic character, resulting in the sufficient and abundant contact probability between electrode and electrolyte. In the same way, carbon dots can improve the wettability between this interface region. Therefore, the charge-transfer and ion migration kinetics were improved, facilitating electrolyte ion transport and storage in the porous electrode (Figure 2.9a). Xiang Zhang and co-workers synthesized graphene oxide/carbon dots/polypyrrole composite, exhibiting a high specific capacitance of 576 F g^{-1} at 0.5 A g^{-1} [91]. Also, Tingkai Zhao and co-workers reported that carbon dots can act as pseudo-capacitive materials. They promoted the redox reaction (Figure 2.9b), resulting in enhancing the electrochemical performance of the electrode [92].

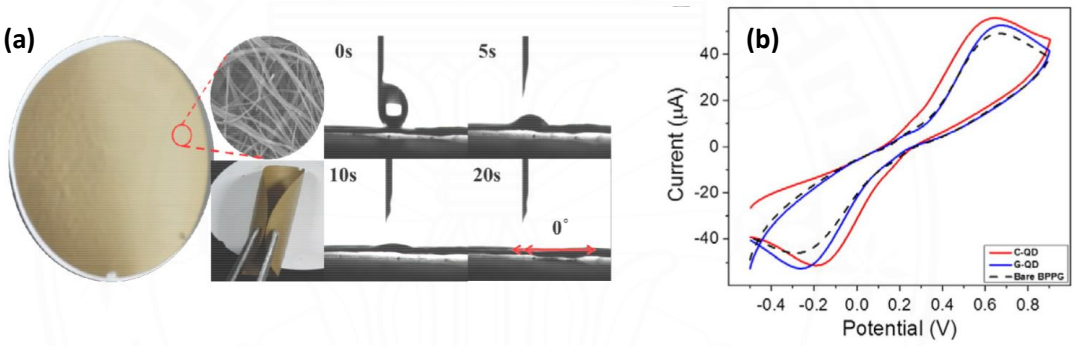

Figure 2.9 (a) Photographs of the composite membrane and the water droplet shape on the membrane at 0, 5, 10 and 20 s. (b) Cyclic voltammograms of graphene quantum dots and carbon quantum dots compared against bare basal-plane pyrolytic graphite (BPPG) in 10 mM potassium ferro/ferricyanide. Adapted from "Carbon Quantum Dot-Induced MnO_2 Nanowire Formation and Construction of a Binder-Free Flexible Membrane with Excellent Superhydrophilicity and Enhanced Supercapacitor Performance," by H. Lv, X. Gao, Q. Xu, H. Liu, Y.-G. Wang, Y. Xia, 2017, *ACS Applied Materials & Interfaces*. Copyright 2017 by ACS publications.

2.6.2 Zinc oxide nanoparticles

Various metal oxides, such as ruthenium oxide (RuO_2), nickel oxide (NiO_2), and manganese oxide (MnO_2), have been widely used as composite electrode materials for supercapacitors. For example, M. Ramani and co-workers fabricated the

RuO_2-carbon composite electrode showing a maximum capacitance of 260 F g^{-1} [93]. Even though these metal oxide-based electrodes provide high specific capacitance and good electrochemical properties, their cost and toxicity are too high when compared to other inexpensive and less toxic metal oxides; thus, limiting their commercial applications. On the other hand, a low-cost, environmental-friendly zinc oxide (ZnO) is widely utilized as catalyst [94], UV absorber [95], in solar cells [96] and batteries [97], etc. This is due to its excellent properties such as wide bandgap, high stability, good electrical properties, and ease of synthesis of ZnO [98]. Moreover, ZnO could be a promising candidate for supercapacitors due to its large surface area and pseudo-capacitance via Faradaic redox reaction for charge/discharge process. For example, Faheem Ahmed and co-workers fabricated ZnO nanorods directly grown on aluminum substrate for high performance supercapacitors [99]. It was fabricated via two steps. First, a seed layer was deposited on aluminium substrate with spin coating technique using ZnO solution. Then, ZnO nanorods grew on the substrate via wet chemical method in the next step (Figure 2.10a). The fabricated electrode provided a high specific capacitance of 394 F g^{-1} measured with scan rate of 20 mV s^{-1} (Figure 2.10b) and showed excellent stability more than 98% capacitance retention for 1000 cycles. In addition, there are many techniques, such as sol-gel method [100], hydrothermal treatment [101], and microwave-assisted synthesis [102], can be used to prepare ZnO in various morphologies, such as nanorods [103], nanocones [104], nanowires [104], and nanoparticles [103]. Among these techniques, the sol-gel method is interesting because it is inexpensive and easy to control the formation of ZnO nanoparticles [105]. However, ZnO-based supercapacitors remain limited by their low rate capacitance because of a slow faradic reaction and low electron transportability at high current [106, 107].

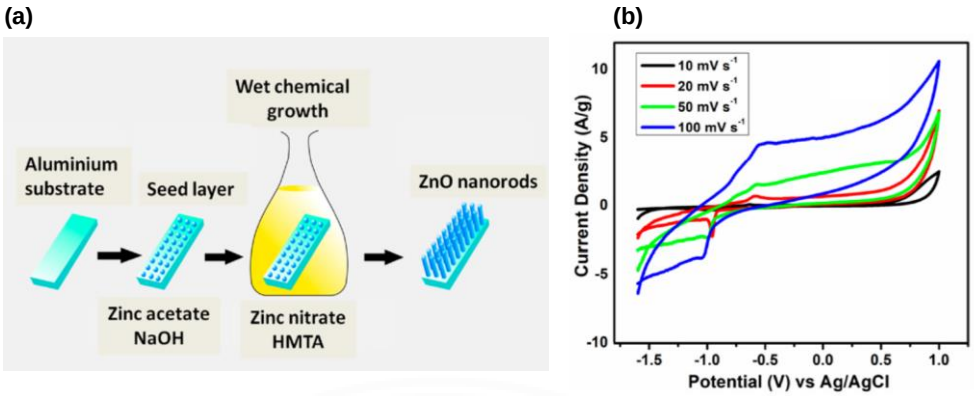

Figure 2.10 (a) A schematic diagram for the growth of ZnO nanorods on Al substrate. (b) CV of ZnO nanorods electrode at various scan rates with 2M KOH electrolyte. Adapted from "Significant increase in current density of inverted polymer solar cells by induced-crystallization of sol-gel ZnO embedded with ZnO-NP," by Jen-Hao Tsai, Ming-Chia Tsai, Cheng-Ying Sung, Ping-Tsung, 2020, *Organic Electronics*, *86*. Copyright 2020 by Elsevier.

To improve the electrochemical performance, the fabrication of composite electrodes between ZnO nanoparticles and other materials can synergistically offer positive results to supercapacitors.

2.7 Gamma irradiation

Gamma irradiation is a form of electromagnetic radiation which emits photons from excited nuclei. The emitted photons provide high energy and short wavelength in the electromagnetic radiation spectrum. Due to its high energy, gamma irradiation has been used in a variety of applications, such as radiotherapy, sterilization, microbial decontamination, and material modification[108]. Many phenomena, including structural modifications, bond breaking, free radical formation, cross-linking, and chain scission, occur when gamma rays interact with the materials [109]. S. Jovanovic and co-workers reported that the irradiation dose of gamma rays affected the structure of graphene quantum dots and one of the interesting results was an improved

singlet oxygen generation and photostability [110]. Ludovic F. Dumée and co-workers converted graphene oxide to reduced-graphene oxide by gamma-ray irradiation, they proposed that electrons from ionization can excited or ionized other atoms and oxygen functionalities were removed from the surface of graphene oxide upon exposure to gamma-ray irradiation [111]. In another study, gamma irradiation in the presence of isopropyl alcohol and EDA was employed for the preparation of nitrogen-doped graphene quantum dots (Figure 2.11) [112]. It was observed that the percentage of carbon atoms increased from 63% to more than 79%. Additionally, the zeta potential of the obtained graphene quantum dots changed from -34.6 to +9.1 mV, owing to the modification of functional groups localized on the surface, resulting in increased photoluminescence intensity. Moreover, it was also revealed that the gamma-irradiated graphene quantum dots emitted mostly blue light, compared to graphene quantum dots without gamma irradiation which emitted violet to blue and evergreen light. Blue photoluminescence of gamma-irradiated graphene quantum dots resulted from sp^2 core, while green photoluminescence originated from the functional groups [113, 114]. Based on these previous studies, the gamma irradiation can effectively modify the carbon-based materials that can potentially benefit the supercapacitor performance and thus needs further investigation.

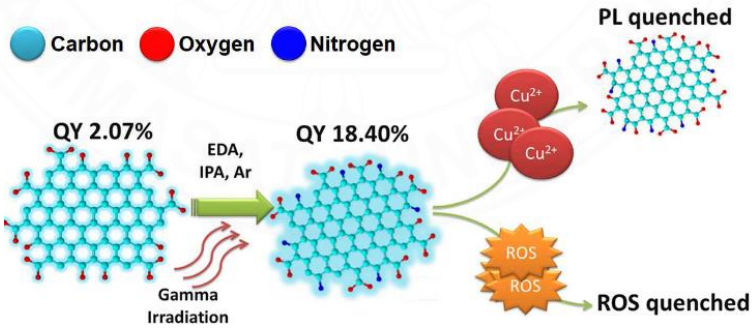

Figure 2.11 A schematic diagram for gamma irradiation of graphene quantum dots with ethylenediamine to enhance their quantum yield. Adapted from "Gamma irradiation of graphene quantum dots with ethylenediamine: Antioxidant for ion sensing," by S. Jovanović, S. Dorontić, D. Jovanović, G. Ciasca, M. Budimir, A. Bonasera, M. Scopelliti, O. Marković, B. Todorović Marković, 2020, *Ceramics International*. Copyright 2020 by Elsevier.

Gamma-irradiated CDs have been applied in various applications, such as photocatalysts [108], sensors [112], medical treatment [115], and biological imaging [116]. However, they have never been employed for supercapacitors. Therefore, the goal of this research is to fabricate novel composite electrodes that consist of gamma-irradiated CDs and ZnO nanoparticles for supercapacitors and to investigate and improve their supercapacitive properties.

2.8 The raw materials used in thesis research

2.8.1 Polyurethane

Polyurethane is a thermoset polymer composed of urethane links in their repeat unit (Figure 2.12). It was first synthesized in 1937 by Otto Bayer in Germany [117]. Because of its availability, excellent mechanical properties, ability to make foam and eco-friendly nature [118], it is widely used in a range of consumer products from apparels to furniture, textiles, automotive, and biomedical applications [119, 120]. Polyurethane is one of the most versatile polymer materials being a part of daily life, and therefore tons of polyurethane become wastes [121]. Therefore, converting polyurethane into scientifically useful carbon dots provides interesting recycling incentives. Since polyurethane is a carbon-based material, it can act as the precursor for the preparation of activated carbon and carbon dots. Furthermore, polyurethane consists of nitrogen, the resulting carbon dots will be highly doped with nitrogen. Nitrogen doping is well known to enhance their quantum efficiency, metal ion chelating ability, and electronic properties [122]. The resulting activated carbon and carbon dots will be used in metal ion sensing and energy storage applications.

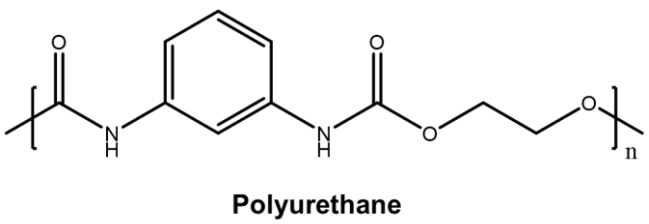

Polyurethane

Figure 2.12 Chemical structure of polyurethane.

2.8.2 Natural rubber

Natural biopolymers (Figure 2.13), such as polysaccharides, proteins, and nucleic acids, are beneficial for multifaceted applications because they are renewable, low cost, non-toxic, and highly biodegradable [123]. Natural rubber is one of natural biopolymer obtained from the *H. Brasiliensis* tree [124]. It consists of water (50-70% w/w), cis-1,4-polyisoprene (25-35% w/w), protein (1-1.8% w/w), carbohydrates (1-2% w/w), etc.[125, 126] Thus, it is a carbon-rich material which is a suitable precursor for the preparation of carbon dots. Natural rubber is used more than 90% in the rubber industry (tires, belts, joints, etc.) [124]. Thailand is the world's largest producer and exporter of natural rubber due to its origination in Thailand during the early 1900s. In recent years, the price of natural rubber has fallen since the rubber industry has been shifting toward using synthetic rubber instead. Thus, the demand for natural rubber was decreased. The transformation of natural rubber to useful carbon dots is one way to increase the value of this resource. The carbon dots prepared from natural rubber will be used in metal ions sensing.

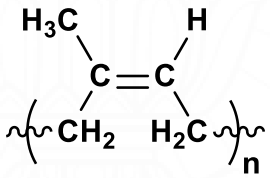

***cis*-1,4-polyisoprene**

Figure 2.13 Chemical structure of natural rubber.

CHAPTER 3
RESEARCH METHODOLOGY

3.1 Materials and chemicals

Polyurethane foam was purchased from Uratex, Philippines and natural rubber was obtained from the Thai local market. All chemicals were purchased from Sigma-Aldrich unless otherwise noted. Sulfuric acid (96 wt%) and nitric acid (65%) were obtained from CARLO ERBA Reagents. All reagents were used without further purification. A high-grade regenerated cellulose dialysis membrane (1,000 MWCO) was brought from Membrane Filtration Product, Inc. Deionized (DI) water (15 MΩ) was used to prepare solutions in all experiments .

3.2 Methods and preparation

This thesis is divided into three parts based on two different raw materials and two applications (Figure 3.1). The methods and preparation steps of each part are shown as follows.

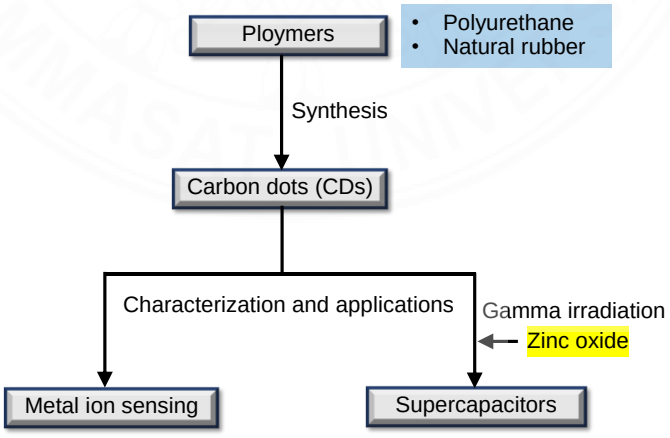

Figure 3.1 Schematic representation of three parts in this thesis research.

3.2.1 Synthesis and applications

3.2.1.1 Polyurethane

(1) Preparation of carbon dots for metal ion sensing

Small pieces of polyurethane (5.00 g) were mixed with 2.5 M sulfuric acid solution (50 mL) in a porcelain crucible and pyrolyzed at 250 °C for 4 h. After the reaction, a black solid was cooled to room temperature to which DI water (50 mL) was added. The resulting mixture was placed in an ultrasonic bath for 30 min to ensure the transfer of carbon dots from the surface of the carbonized polyurethane to the DI water. The mixture was filtered to obtain carbon dots in the resulting solution. Carbon dots solution was then neutralized with sodium hydroxide and dialysis for 4 days. Finally, it was freeze-dried for 24 h to obtain the carbon dots powder for further use. The preparation step is shown as follows (Figure 3.2).

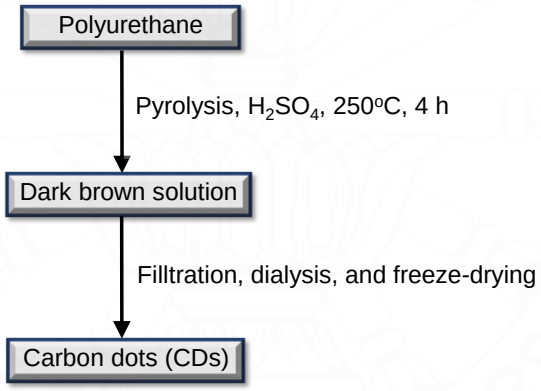

Figure 3.2 The preparation step of carbon dots from polyurethane for metal ion sensing.

(2) Preparation of the gamma-irradiated, amine-passivated carbon dots and zinc oxide (ZnO) nanoparticles for supercapacitor application

To prepare the gamma-irradiated, amine-passivated carbon dots in this application, the obtained carbon dots (0.1 g) were mixed with 4 mL EDA, 3 mL isopropyl alcohol, and 93 mL DI water. Before irradiation, the prepared solution was ultrasonicated while bubbling with N_2 gas to remove oxygen molecules from the dispersion. The prepared solution was irradiated using an irradiation unit with Co-60 as

an irradiation source with a dosage of 50 and 200 kGy. After irradiation, the obtained solution was then added with sodium hydroxide, dialyzed, and freeze-dried for 24 h to obtain the gamma-irradiated, amine-passivated carbon dots powder. The obtained powders irradiated with a dose of 50 and 200 kGy in the presence of EDA were labeled CDs-EDA-50 and CDs-EDA-200, respectively. In case of no EDA adding, carbon dots (0.1 g) were mixed with 3 mL isopropyl alcohol and 97 mL deionized water. The remaining experimental procedure was the same as previously mentioned. The gamma-irradiated powders with a dose of 50 and 200 kGy were denoted as CDs-50 and CDs-200, respectively.

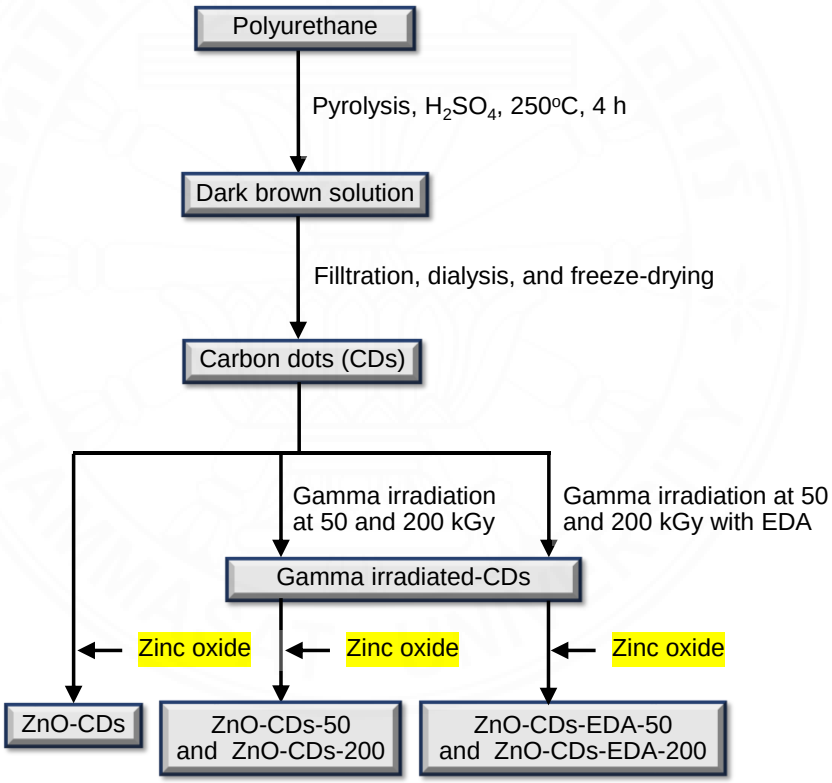

Figure 3.3 The preparation of the electrode for supercapacitor application.

Zinc oxide (ZnO) nanoparticles for supercapacitor application were synthesized using sol-gel method. Zinc acetate dihydrate ($Zn(CH_3COO)_2 \cdot 2H_2O$) (20 g) was dissolved in 150 mL DI water and stirred for 20 min at room temperature to

form a homogeneous zinc acetate solution. Sodium hydroxide (80 g) was dissolved in 80 mL DI water and stirred for 20 min at room temperature. The prepared zinc acetate and sodium hydroxide solutions were then mixed. After mixing, 100 mL ethanol was added dropwise into the mixture with vigorous stirring for 90 min to obtain a gel-like product. After stirring was stopped, a white precipitate formed. The precipitate was filtered and washed with deionized water and absolute ethanol several times and then dried at 80°C for 4 h. The obtained powder was calcined at 400 °C for 2 h in a furnace. Finally, ZnO nanoparticles were obtained. The chemical reactions for the formation of ZnO nanoparticles are shown in Equation 1 and 2.

$$Zn(CH_3COO)_2 + 2NaOH \xrightarrow{\Delta} Zn(OH)_2 + 2NaCH_3COO \quad (1)$$

$$Zn(OH)_2 \longrightarrow ZnO + H_2O \quad (2)$$

(2) Selectivity and interference tests for metal ion sensing

Metal ion solutions (100 μM), including K^+ (KNO_3), Mg^{2+} ($MgCl_2$), Sn^{2+} ($SnCl_2$), Zn^{2+} ($ZnCl_2$), Ag^+ ($AgNO_3$), Ca^{2+} ($Ca(NO_3)_2$), Co^{2+} ($CoCl_2$), Cd^{2+} ($Cd(NO_3)_2$), Cu^{2+} ($Cu(NO_3)_2$), Ni^{2+} ($Ni(NO_3)_2$), Fe^{3+} ($FeCl_3$), and Cr^{6+} ($K_2Cr_2O_7$) were prepared for selectivity testing. Each of metal ion solution (2 mL) and carbon dot solution (2 mL, 0.05 $g{\cdot}L^{-1}$) were mixed and transferred to a quartz cuvette. The fluorescence emission spectra of these mixtures were recorded and the most strongly quenched of metal ion was further examined to determine limit of detection (LOD).

To further confirm the Ni^{2+} selectivity of the carbon dots in the presence of other metal ions as interferences, the carbon dot solution (2 ml, 0.05 gL^{-1}) was mixed with Ni^{2+} solution (1 ml, 100 μM) and interference solution (1 ml, 100 μM). The fluorescence emission spectra of all samples and carbon dots solution without adding the interferences were then recorded.

(3) Sensitivity test for metal ion sensing

The sensitivity of the carbon dots was tested using Ni^{2+} solution mixed with the carbon dot solution in different volume ratios to prepare mixtures with various concentrations ranging between 0 to 250 μM of Ni^{2+}. The fluorescence emission intensities of all samples were then recorded. The LOD was calculated using Equation 3:

$$LOD = \frac{3 \times standard\ deviation}{slope} \quad (3)$$

(4) Spiking experiment in DI water and drinking water

Three types of drinking water were obtained to determine the accuracy of carbon dots for Ni^{2+} analysis using fluorescence spectroscopy and the inductively coupled plasma-optical emission spectrometry (ICP-OES) as a reference method. The carbon dot solutions (4 mL, 0.05 $g \cdot L^{-1}$) were prepared using the drinking water samples and spiked with Ni^{2+} (5 µM). The fluorescence emission intensities of prepared samples were recorded and compared with the results from the ICP-OES method. The recovery and relative standard deviation (RSD) as a percentage were calculated by Equation 4 and 5:

$$\%\text{Recovery} = \frac{\text{Concentration of } Ni^{2+} \text{found (florescence spectroscopy)}}{\text{Concentration of } Mg^{2+} \text{found (ICP-OES)}} \times 100 \quad (4)$$

$$\%\text{RSD} = \frac{\text{SD}}{\bar{X}} \times 100 \quad (5)$$

(5) Paper-based sensor

Whatman No.1 filter papers were cut into 2×2 cm^2 as solid-state fluorescent sensors. The small papers were immersed in the carbon dot solution (0.05 $g \cdot L^{-1}$) and dried at 60 °C for 1 h to obtain the paper-based sensors. The solutions of metal ion (20 µL), $K^+(KNO_3)$, $Mg^{2+}(MgCl_2)$, $Sn^{2+}(SnCl_2)$, $Zn^{2+}(ZnCl_2)$, Ag^+ ($AgNO_3$), $Ca^{2+}(Ca(NO_3)_2)$, Co^{2+} ($CoCl_2$), $Cd^{2+}(Cd(NO_3)_2)$, $Cu^{2+}(Cu(NO_3)_2)$, $Ni^{2+}(Ni(NO_3)_2)$, $Fe^{3+}(FeCl_3)$, and Cr^{6+} ($K_2Cr_2O_7$) ions, were dropped onto the obtained paper-based sensors and dried at 60 °C for 1 h. After drying, they were illuminated under a UV light and were taken for pictures using an iPhone camera.

To study the sensitivity of the obtained paper-based sensors, they were dropped with various concentrations of Ni^{2+} ranging from 0 to 250 µM and were taken for pictures to extract red-green-blue (RGB) values. The sum of RGB values was calculated using Equation 6:

$$\text{Sum RGB values} = \text{Red} + \text{Green} + \text{Blue} \quad (6)$$

(6) Supercapacitor preparation

To fabricate the composite electrode, the obtained ZnO nanoparticles were mixed with carbon black and poly(vinylidene fluoride) as a binder in a ratio of 80:15:5% w/w in *N*-methyl-2-pyrrolidone as a solvent to form a slurry solution. The slurry solution was coated on carbon paper as a current corrector and then dried at 80^{o} C in the oven for 2 h to obtain the electrode. To investigate the effects of gamma-irradiated CDs on the electrochemical performance, CDs-50, CDs-200, CDs-EDA-50, and CDs-EDA-200 (5% w/w each) were added, which were denoted as ZnO-CDs-50, ZnO-CDs-200, ZnO-CDs-EDA-50, and ZnO-CDs-EDA-200, respectively. The addition of unmodified CDs (5% w/w) in the electrode was used as a control sample, which was denoted as ZnO-CDs.

3.2.1.2 Natural rubber

(1) Preparation of carbon dots for metal ion sensing

High-ammonia natural rubber latex (60% DRC, 15 mL) was mixed with DI water (15 mL) in a porcelain crucible. Then, the mixture was placed into a furnace and pyrolyzed at 350°C for 6 h. After pyrolysis, the resulting black solid was allowed to cool to room temperature, mixed with 0.5 M nitric acid, transferred to Teflon lined autoclave, and kept in the furnace at 200°C for 6 h. After the termination of the reaction time, the resulting dark brown solution was cooled to room temperature, mixed with deionized water (50 mL), and then placed in an ultrasonic bath for 30 min to ensure the transfer of carbon dots from the surface of the carbonized natural rubber to the deionized water. The solution was filtered, neutralized, and purified using a dialysis membrane (1000 Da MWCO) for 4 days. Then, the resulting solution was stored and freeze-dried for 24 h to obtain carbon dots powder for further use.

(2) Selectivity and interference tests for metal ion sensing

Metal ion solutions (100 μM), including K^{+} (KNO_3), Mg^{2+} ($MgCl_2$), Sn^{2+} ($SnCl_2$), Zn^{2+} ($ZnCl_2$), Ag^{+} ($AgNO_3$), Ca^{2+} ($Ca(NO_3)_2$), Cd^{2+} ($Cd(NO_3)_2$), Cu^{2+} ($Cu(NO_3)_2$), Ni^{2+} ($Ni(NO_3)_2$), Fe^{3+}($FeCl_3$) and Cr^{6+} ($K_2Cr_2O_7$) were prepared for selectivity testing. Each of metal ion solution (2 mL) and carbon dot solution (2 mL, 0.05 $g{\cdot}L^{-1}$) were mixed and transferred to a quartz cuvette. The fluorescence emission spectra of these mixtures were recorded and the most strongly quenched of metal ion was further examined to determine limit of detection (LOD).

To further confirm the Mg^{2+} selectivity of the carbon dots in the presence of other metal ions as interferences, the carbon dot solution (3 ml, 0.05 gL^{-1}) was mixed with Mg^{2+} solution (1 ml, 100 µM) and interference solution (1 ml, 100 µM). The fluorescence emission spectra of all samples and carbon dots solution without adding the interferences were then recorded as above.

(3) Sensitivity test for metal ion sensing

The sensitivity of the carbon dots was tested using Mg^{2+} solution mixed with the carbon dot solution in different volume ratios to prepare mixtures with various concentrations ranging between 0 to 250 µM of Mg^{2+}. The fluorescence emission intensities of all samples were then recorded. The LOD was calculated using Equation 3.

(4) Spiking experiment in DI water and drinking water

Three types of drinking water were obtained to determine the accuracy of carbon dots for Mg^{2+} analysis using fluorescence spectroscopy and the inductively coupled plasma-optical emission spectrometry (ICP-OES) as a reference method. The carbon dot solutions (2 mL, 0.05 $g{\cdot}L^{-1}$) were prepared using the drinking water samples and spiked with Mg^{2+} (5 µM). The fluorescence emission intensities of prepared samples were recorded and compared with the results from the ICP-OES method. The recovery and relative standard deviation (RSD) as a percentage were calculated by Equations 4 and 5.

(5) Paper-based sensor

Whatman No.1 filter papers were cut into 2×2 cm^2 as solid-state fluorescent sensors. The small papers were immersed in the carbon dot solution (0.05 $g{\cdot}L^{-1}$) and dried at 80 °C for 1 h to obtain the paper-based sensors. The solutions of metal ion (20 µL), $K^+(KNO_3)$, $Mg^{2+}(MgCl_2)$, $Sn^{2+}(SnCl_2)$, $Zn^{2+}(ZnCl_2)$, Ag^+ ($AgNO_3$), $Ca^{2+}(Ca(NO_3)_2)$, $Cd^{2+}(Cd(NO_3)_2)$, $Cu^{2+}(Cu(NO_3)_2)$, $Ni^{2+}(Ni(NO_3)_2)$, $Fe^{3+}(FeCl_3)$, and Cr^{6+} ($K_2Cr_2O_7$) ions, were dropped onto the obtained paper-based sensors and dried at 80 °C for 1 h. After drying, they were illuminated under a UV light and were taken for pictures using an iPhone camera.

To study the sensitivity of the obtained paper-based sensors, they were dropped with various concentrations of Mg^{2+} ranging from 0 to 200 µM and

were taken for pictures to extract red-green-blue (RGB) values. The sum of RGB values was calculated using Equation 6.

3.3 Characterizations

3.3.1 The functional groups on the surface and elemental components of carbon dots

The functional groups on the surface and elemental components of carbon dots were characterized using a Perkin Elmer FT-IR spectrometer (Spectrum 2000) and KBr pellets and X-ray photoelectron spectrometer (XPS; AXIS ULTRA^{DLD}, Kratosanalytical, Manchester UK.).

3.3.2 The morphology and particle sizes

The morphology and particle sizes were determined using a transmission electron microscope (JEOL JEM-2100) .The accelerating voltage was 200 kV.

3.3.3 The optical properties and quantum yields of carbon dots

The optical properties and quantum yields of carbon dots were measured using a UV–vis spectrophotometer (Shimadzu, UV-1700 PharmaSpec) and fluorescence spectrometer (Jasco, FP-6200).

3.3.4 The morphology and structure of ZnO nanoparticles

The morphology and structure of ZnO nanoparticles were characterized by a scanning electron microscope (JEOL, JEM-2010) and an X-ray diffractometer (XRD; Rigaku, SmartLab).

3.3.5 Quantum yield measurement

The relative quantum yield of carbon dots was measured with quinine sulfate as a reference, using Equation 7:

$$\phi = \phi_R \times \frac{I}{I_R} \times \frac{A_R}{A} \times \frac{n^2}{n_R^2} \quad (7)$$

where ϕ is the quantum yield, I is the integrated emission intensity measured using a fluorescence spectrometer, n is the refractive index, A is the absorbance measured using a UV–vis spectrometer, and the subscript R relates to the reference, which is quinine sulfate in 0.1 M sulfuric acid solution (ϕ_R = 54% at 360 nm).

3.3.6 The geometric information

The geometric information about interatomic distances, coordination numbers of shells surrounding the absorbing atom, and cation site distribution within the spinel structure was studied using extended X-ray absorption fine structure (EXAFS). Moreover, X-ray absorption near edge structure (XANES) allows obtaining information on the oxidation states of the absorbing atoms and on-site symmetry.

3.3.7 Supercapacitor characterization

Electrochemical cells in three- and two-electrode configurations were employed for electrochemical characterization using a potentiostat/galvanostat (μAutolab, PGSTAT204). In the three-electrode system, a Pt counter electrode (CE), an Ag/AgCl reference electrode (RE), and the prepared electrode as a working electrode (WE) were used for the electrochemical response measurement using cyclic voltammetry (CV) at the various scan rates for 3 cycles and electrochemical impedance spectroscopy (EIS) which was conducted in a frequency range between 100 kHz and 100 mHz with an amplitude of 10 mV. The two-electrode configuration containing a pair of symmetric prepared electrodes was used for galvanic charge-discharge (GCD) assay at the various current densities. A Swagelok cell was used to measure the cyclability using carbon paper and Whatman filter paper with a diameter of 1 cm as a current collector and separator, respectively.

The specific capacitance (Cs, F g^{-1}) was derived from the cyclic voltammogram and calculated by applying the following expression (Equation 8):

$$Cs\ (F.g^{-1}) = \frac{I \times t}{V \times m} \quad (8)$$

where I (A) is the current applied to the device, t (s) is the discharge time, V (V) is the window voltage, and m (g) is mass of active materials.

Moreover, contact angle analysis of the obtained electrodes were conducted using a Biolin Scientific contact angle meter and electrolyte droplet (1 μL).

CHAPTER 4
RESULTS AND DISCUSSION

4.1 Highly sensitive Ni^{2+} sensors based on polyurethane-derived, label-free carbon dots with high adsorption capacity

4.1.1 Characterizations

4.1.1.1 Size and morphology characterization

The particle size and morphology of carbon dots were characterized using TEM. As shown in Figures 19a and b, the carbon dots were mostly spherical with an average diameter of approximately 4 nm. The agglomeration was due to the highly hydrophilic nature of carbon dots. The inset in Figure 4.1a shows the layer spacing of a representative carbon dot to be 0.3 nm. The zeta potential of carbon dots was -12.0 mV, which corresponds to the agglomeration of particles of carbon dots, consistent with the TEM result.

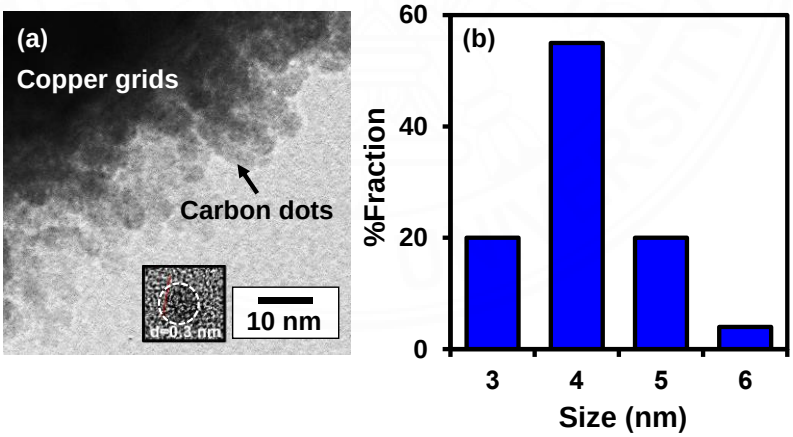

Figure 4.1 (a) TEM images with inset figure showing the layer spacing of a representative carbon dot. (b) Size distribution of carbon dots.

4.1.1.2 Structural characterization

To analyze the structure of the prepared carbon dots, FT-IR spectroscopy was used. The FT-IR spectra of polyurethane and carbon dots were obtained (Figure 4.2a). The polyurethane spectrum showed the presence of O-H/N-H, C-H, C=O, C=C, and C-O stretching vibrations at 3280, 2900, 1720, 1600, and 1120 cm^{-1}, respectively[127, 128]. The carbon dots showed a similar O-H/N-H signal and the appearance of C-S vibration at 619 cm^{-1}, but weaker C-H, C=C, and C=O vibrations and a much stronger C-O vibration. This change suggests that the carbon dots contained the dominant O-H/N-H, C-O, and C-S bonds. The carbon dots were sulfur-doped because of the use of sulfuric acid as a reagent. The presence of these groups suggests the hydrophilicity of carbon dots as the carbon dots were indeed highly soluble in water.

The carbon dots were then characterized using XPS. The survey XPS spectrum showed four relevant signals of O_{1s}, N_{1s}, C_{1s}, and S_{2p} at 532.1, 399.1, 285.1, and 169.1 eV, respectively (Figure 4.2b). The carbon dots were mainly composed of carbon (57.61%), oxygen (32.44%), nitrogen (7.38%), and sulfur (2.57%). The high concentration of nitrogen was as expected because polyurethane consists of two nitrogen atoms per one repeating unit and sulfur came from the use of sulfuric acid. The high-resolution C_{1s} signal can be deconvoluted into four peaks, which correspond to C=C, C-C, C-N, and C-O (Figure 4.2c). The high resolution N_{1s} spectrum showed the presence of graphitic-N, C-N, and N-H (Figure 4.2d) whereas the high resolution O_{1s} spectrum revealed the C=O, O=C-N, C-O-C, and -COOH groups (Figure 4.2e). A combination of FT-IR and XPS results suggests that the carbon dots consisted of carboxyl, amide/amine, hydroxyl, and carbonyl groups and were nitrogen- and sulfur-doped.

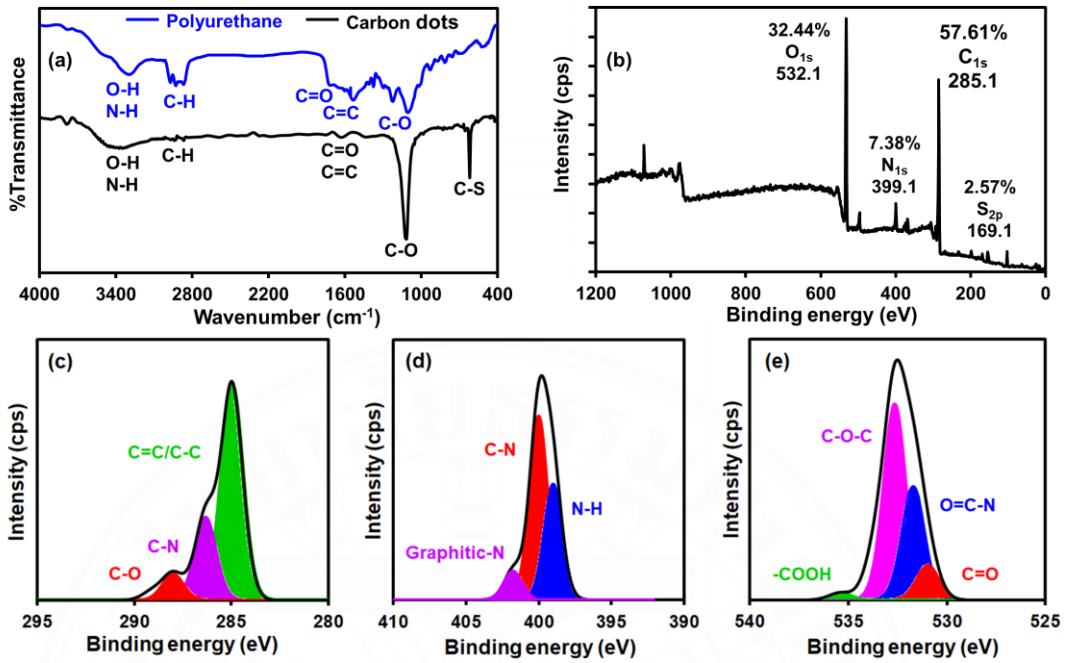

Figure 4.2 (a) FT-IR spectrum of polyurethane and carbon dots. (b) Survey XPS spectrum of carbon dots, (c) C_{1s}, (d) N_{1s}, and (e) O_{1s} spectra of carbon dots.

4.1.1.3 Optical characterization

Optical properties of carbon dots were investigated using UV-vis and fluorescence spectroscopy. From the UV-vis spectrum, the carbon dots exhibited a broad absorption similar to other previously reported carbon dots [129-131] (Figure 4.3a). A peak at around 250 nm was caused by π-π* transition of the aromatic sp^2 carbon in the carbon dots [132]. This peak is attributed to the unsaturated carbon atoms in the carbon dots, similarly identified from the FT-IR and XPS spectra. Another peak at about 300 nm is attributed to n-π* transition. The fluorescence emission of carbon dots was characterized using fluorescence spectroscopy .Maximum fluorescence emission of carbon dots was observed at 492 nm when using an excitation wavelength of 380 nm (Figure 4.3b). The inset in Figure 4.3b shows photographs of the carbon dot solutions under visible light and 365-nm UV light. The carbon dot solution under UV irradiation exhibited the blue color emission. The quantum yield of the carbon dots is 24%, which is relatively high compared to the carbon dots synthesized

from other synthetic polymers (Table 4.1). This is a result of high doping of nitrogen and sulfur atoms of carbon dots [133, 134]. The position of the emission peak remains unchanged when the excitation wavelength was increased from 300-400 nm, demonstrating an excitation-independent emission. This excitation-independent photoluminescence behavior suggests homogenous surface states of carbon dots due to the use of pure polyurethane as a pure precursor [135]. Additionally, the excitation-independent behavior is often observed in highly nitrogen -and sulfur-doped carbon dots and the use of pure chemical precursors [135-137]. This behavior represented well-defined carbon dots, demonstrating control over their structures and properties.

It is well known that the optical properties of carbon dots are governed by the surface states and the environment in which they are in. In this experiment, the fluorescence emission of carbon dots was investigated in solutions with pH values ranging from 1.0 to 13.0. It was found that the fluorescence intensity decreased by about 30-55% in strong acidic and basic conditions in which the acidic conditions caused a slightly larger reduction than the basic conditions (Figure 4.3c). A pH of 9 yielded the highest fluorescence emission. This pH dependence is a result of protonation and deprotonation of the carbon dots, leading to modulation of the emissive sites as also found in carbon dots prepared from, for example, κ-carrageenan and phenyl boronic acid [138], cherry blossom flowers[139], and water hyacinth leaves [140]. The photostability of carbon dots for a period of time was next examined. It was found that the fluorescence emission intensity remained nearly the same for at least 6 weeks (Figure 4.3d). Based on these results, the carbon dots did not photobleach and are therefore the proper fluorophores for applications that require long-term photostability.

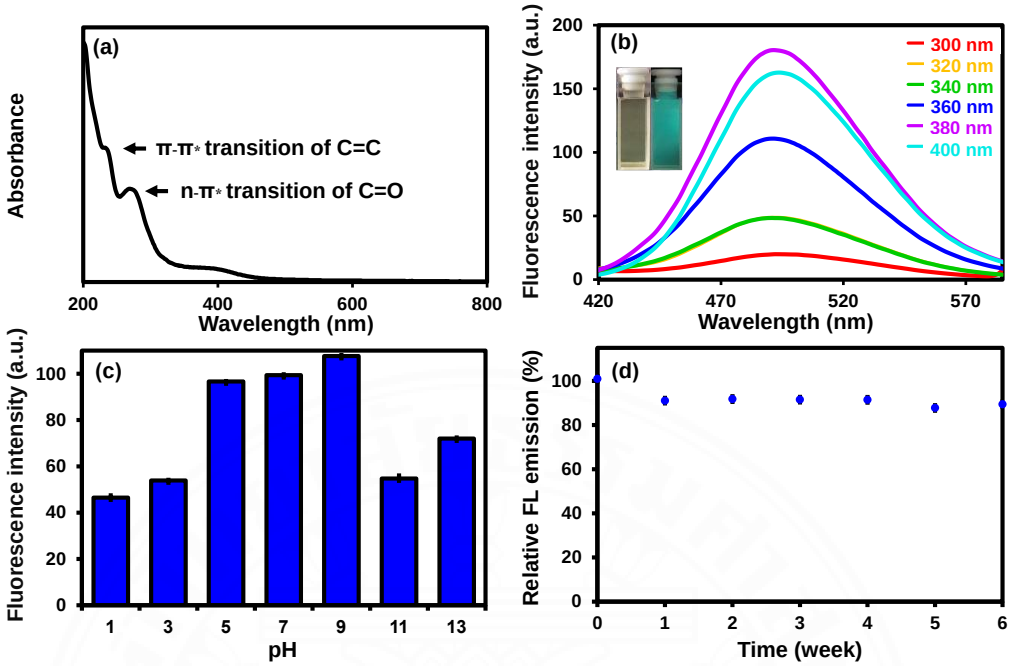

Figure 4.3 (a) UV-vis absorption spectrum, (b) fluorescence emission spectra of carbon dots with inset photographs of carbon dot solutions under visible light (left) and UV light (365 nm) (right). (c) Fluorescence intensities of carbon dots in solutions with different pH, and (d) photostability of carbon dots in aqueous solutions.

Table 4.1

Quantum yields of synthetic polymer-derived carbon dots

Precursor	Quantum yield (%)	Reference
Polyethyleneimine	0.7	[141]
Polyethylene glycol	7.8	[142]
Polystyrene	13.0	[143]
Polyvinylpyrrolidone	23.6	[144]
Crosslinking polyacrylic acid and ethylenediamine	44.2	[145]
Polyurethane	24.0	This work

4.1.2 Ni^{2+} ion sensing

4.1.2.1 Selectivity and interference tests for Ni^{2+} ion sensing

Carbon dots are known as excellent chelating ligands for complexation with metal ions, making them appropriate for use as metal ion sensors. Firstly, we characterized the selectivity of the carbon dots by measuring their fluorescence intensity in the presence of K^{+}, Mg^{2+}, Sn^{2+}, Zn^{2+}, Ag^{+}, Ca^{2+}, Co^{2+}, Cd^{2+}, Cu^{2+}, Ni^{2+}, Fe^{3+}, and Cr^{6+}. These metal ions were chosen because they are abundant and ubiquitous. Figure 4.4a and b demonstrate that the fluorescence intensities were not significantly altered by any metal ions except Ni^{2+}. Ni^{2+} could quench the fluorescence intensity of carbon dots by almost 70% compared to other tested metal ions. This indicates that the carbon dots were selective to Ni^{2+}.

The selectivity of carbon dots towards Ni^{2+} was further investigated via interference experiment. This experiment was carried out by measuring the fluorescence emission of the carbon dots in the presence of Ni^{2+} and other metal interferences, including Ag^{+}, Ca^{2+}, Cd^{2+}, Cu^{2+}, Mg^{2+}, Sn^{2+}, Zn^{2+}, Co^{2+}, Cr^{6+}, Fe^{3+}, and K^{+}. As shown in Figure 4.4c, it was found that the fluorescence emission of carbon dots in the presence of Ni^{2+} was nearly unchanged even in the presence of the interferences. This confirmed that carbon dots remained selective towards Ni^{2+}, even when interferences were present.

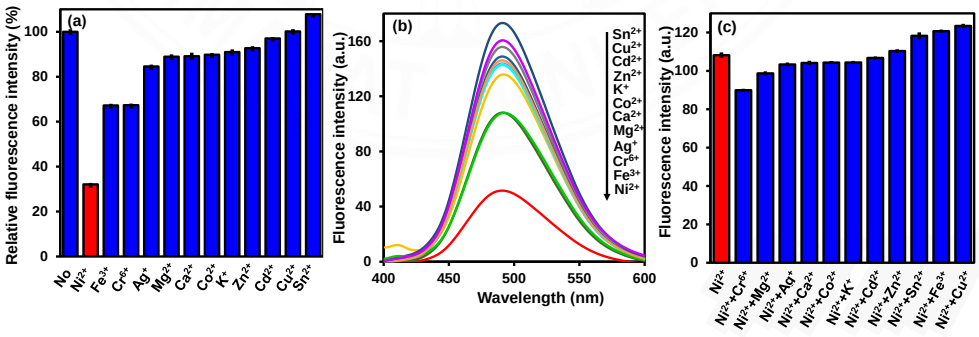

Figure 4.4 (a) Relative fluorescence emission intensities and (b) fluorescence spectra of carbon dots upon the addition of metal ions. (c) Fluorescence emission intensities of carbon dots after the addition of Ni^{2+} and other metals as interferences.

4.1.2.2 Sensitivity test for Ni^{2+} ion sensing

The fluorescence quenching dependence on Ni^{2+} concentration was further investigated using eight concentrations ranging from 0 to 250 µM. We found that the fluorescence intensity of carbon dots decreased with increasing Ni^{2+} concentration. The limit of detection (LOD) calculated using 3σ/slope method was 3.14 µM, which was calculated using the standard deviation of 10 measurements (Figure 4.5). This is about 300 times better than the LOD of the carbon dots reported by Y. Gong *et al.*[146] (Table 4.2). Although some other sensors produced better LODs and/or linear ranges. Our carbon dots are much simpler to prepare via a one-step pyrolysis than the previously reported materials, e.g. hydrazone derivative [147], pyrimidine ligand[148], imprinted polymers [149], and functionalized silver nanoparticles [150-152]. It is noteworthy to point out that in our previous work the carbon dots were prepared from polyurethane, which were found to be selective to Ag^{+} [132]. The differences between our previous work and this present work are in the amount of polyurethane and reaction conditions used in the synthesis. The amount of polyurethane per acid volume and temperature were higher, but the H_2SO_4 concentration was lower in this work as compared to the previous study. Indeed, the carbon dots in this work contained higher nitrogen and less sulfur contents than the carbon dots in the previous study as consistent with the less polyurethane amount, H_2SO_4 concentration, and temperature. Despite the same precursor, this indicates that the properties and compositions of carbon dots are highly controlled by synthesis conditions, which in turn governs the selectivity of carbon dots towards metal ions.

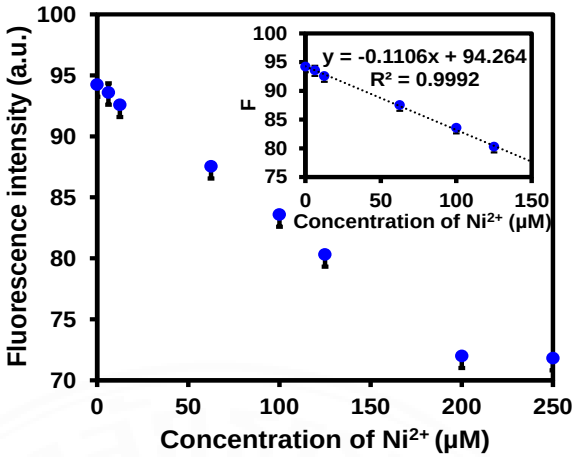

Figure 4.5 Plot of fluorescence emission intensities with inset figure showing a plot between fluorescence emission intensities and Ni^{2+} concentrations in the linear range.

Table 4.2

Summary of Ni^{2+} sensors

Materials	Linear range (μM)	LOD (μM)	Ref
Hydrazone derivative immobilized on the triacetyl cellulose membrane	5×10^{-4} – 20.4	1×10^{-4}	[153]
Pyrimidine ligand-coated graphite electrode	0.02-100,000	8×10^{-3}	[154]
Ni^{2+} ion-imprinted polymer	10-100,000	5	[156]
Glutathione-stabilized silver nanoparticles	1-100	75	[157]
Citrate-stabilized silver nanoparticles	700-1,600	750	[158]
Imidazole-functionalized carbon dots	6,000-100,000	930	[159]
Carbon dots from polyurethane	0-150	3.14	This work

4.1.2.3 The response time for Ni^{2+} ion sensing

To evaluate the response time of the carbon dots, the fluorescence emission intensity of carbon dots with metal ions was measured as a function of time. The measurement was recorded every 50 seconds, the minimum time required for each spectrum scan. Again, only Ni^{2+} caused the fluorescence quenching immediately after the first measurement. The fluorescence intensity showed no decrease after 50 seconds for all other metal ions (Figure 4.6a). More importantly, the fluorescence intensity of carbon dots in the presence of Ni^{2+} remained constant, indicating the fluorescence quenching was complete within 50 seconds. This experiment thus confirmed rapid and selective detection of Ni^{2+} by the carbon dots. The fluorescence emission intensities of the carbon dots with five concentrations of Ni^{2+} ranging from 100 to 500 µM were further investigated. Similarly, all five concentrations of Ni^{2+} could quench the fluorescence emission intensities of carbon dots within 50 seconds before levelling (Figure 4.6b). This indicates a rapid detection of Ni^{2+} by carbon dots that can be obtained within 50 seconds or faster if a faster spectrometer is used.

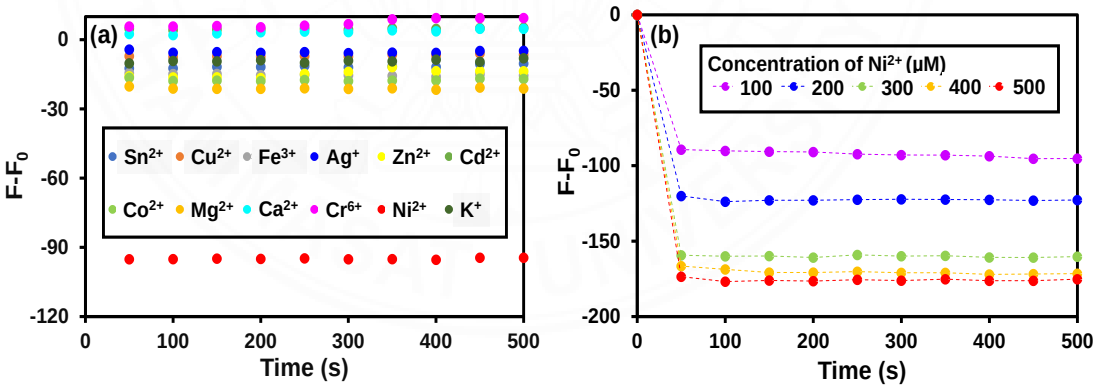

Figure 4.6 (a) Time profiles of fluorescence emission of the carbon dots in the presence of metal ions. (b) Time profiles of fluorescence emission of the carbon dots with different concentrations of Ni^{2+}.

4.1.2.4 The quenching mechanism

To further determine the quenching mechanism, the UV-vis absorbance of Ni^{2+} solution and Ni^{2+}/carbon dot solution were measured at 380 nm. The linear relationship was obtained for both solutions, following the Beer-Lambert law (Figure 4.7a). However, the slope of Ni^{2+}-carbon dot solution, equivalent to an absorption coefficient, differed from that of Ni^{2+} solution, indicating that the formation of static complexes between Ni^{2+} and carbon dots took place [160]. The formation of static complexes also indicates Ni^{2+} was adsorbed on the surface of the carbon dots. The adsorbent properties of the carbon dots can be then further investigated. The fluorescence emission of carbon dots was decreased with increasing the concentration of Ni^{2+} and remained constant when the concentration exceeded 200 µM (Figure 4.5). This result indicated that the saturation of fluorescence quenching of carbon dots by Ni^{2+} was at 200 µM. We used this saturation concentration to calculate the maximum adsorption capacity of the carbon dots. The diameter of the carbon dots was approximately 4 nm, the Ni^{2+} surface coverage of carbon dots was calculated to be 3.63 ions/nm^2 (calculation in appendix A) [161], meaning that one carbon dot can adsorb and accommodate upto 182 Ni^{2+} ions, equivalent to 234.8 $mg \cdot g^{-1}$, which is the highest to date (Table 4.3). The high adsorption capacity is due to their small size, large surface area, and ability to strongly bind Ni^{2+} through hydrophilic functional groups and heteroatoms.

To further examine the fluorescence quenching mechanism, the UV-vis absorption of Ni^{2+} and fluorescence emission of the carbon dots were investigated. It was found that the UV-vis absorption spectrum of Ni^{2+} slightly overlapped with the fluorescence emission spectrum of carbon dots (pink area) (Figure 4.7b). Furthermore, the fluorescence excitation spectrum of the carbon dots largely overlapped with the UV-vis absorption spectrum of Ni^{2+} (green area), which confirms that the sensing mechanism proceeded via inner filter effect. The UV-vis absorption of other metal ions did not overlap with the fluorescence emission of the carbon dots (Figure A1). This suggests that the inner filter effect also contributed to the fluorescence quenching of carbon dots by Ni^{2+}. It can be briefly concluded that the synergetic effects of non-fluorescence complex formation and inner filter effect contributed to the selective and sensitive quenching of the carbon dots towards Ni^{2+}. To further investigate

the inner filter effect, the optical band gaps (E_g) of carbon dots and Ni^{2+} were estimated from Tauc plot (Figure 4.7c and d) [162]. The Tauc plot showed that the optical band gaps of carbon dots and Ni^{2+} are 5.3 and 3.8 eV, respectively, which are close the literature values [163, 164]. The larger optical band gap of carbon dots confirmed that the emission energy after energy absorption was sufficient to be absorbed by Ni^{2+} (Figure 4.7e), which is in consistency with the overlapped carbon dot emission and Ni^{2+} absorption in Figure 4.7b. Moreover, we believed that the functional groups of carbon dots, such as carbonyl, hydroxyl, and carboxylate groups, induced Ni^{2+} via electrostatic attraction leading to effective inner filter effect.

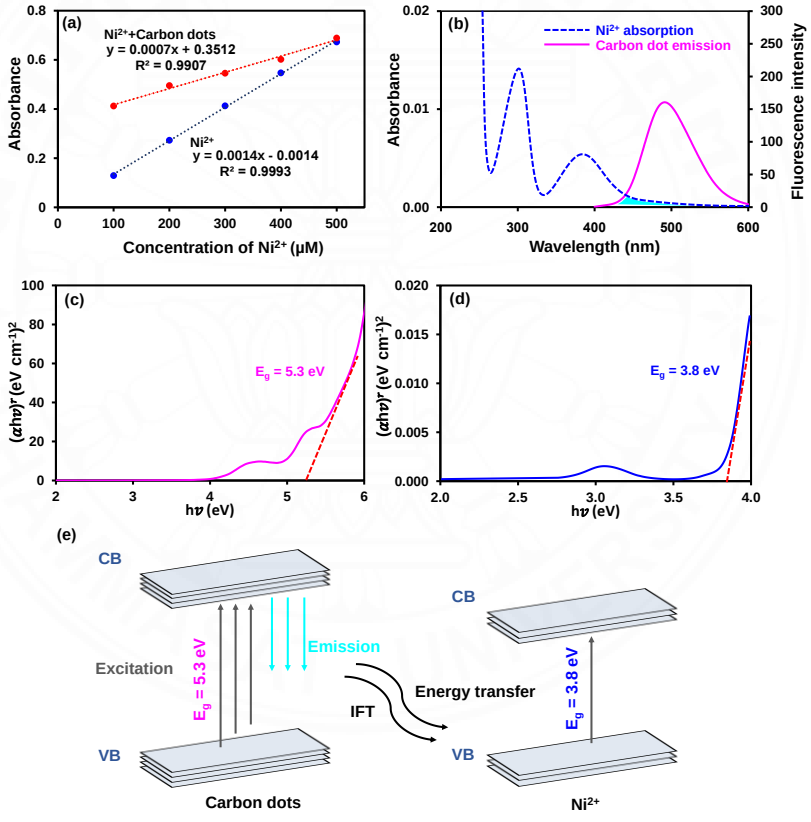

Figure 4.7 (a) UV-vis absorption spectra of Ni^{2+} and Ni^{2+}-carbon dot solutions at 380 nm. (b) UV-vis absorption of Ni^{2+} solution, fluorescence emission spectrum of carbon dots excited at 380 nm, and fluorescence excitation spectrum of carbon dots at 492 nm emission. Tauc plots of (c) carbon dots and (d) Ni^{2+}. (e) Scheme of energy level diagram describing energy transfer processes and inner filter effect (IFE) between carbon dots and Ni^{2+}.

Table 4.3

Adsorption capacities of different adsorbents for Ni^{2+} ions

Adsorbent	Adsorption capacity ($mg \cdot g^{-1}$)	Ref.
Palm shell activated carbon	0.130	[165]
Brewed tea waste	1.163	[166]
Activated carbon prepared from Lapsi seed stone	69.49	[167]
Lignocellulose/montmorillonite nanocomposite	94.86	[168]
Chitosan	159.058	[169]
Carbon dots	234.8	This work

To manifest the interaction between Ni^{2+} and the carbon dots, XAS was used to examine the local electronic structure of Ni^{2+}. In particular, the XANES spectrum can provide the valency information of the absorbing atom[170, 171]. In order to analyze the edge region, a background was carefully subtracted from the raw data, followed by a normalization of the spectra. The resulting spectra are shown in Figure 4.8. Comparing these two spectra immediately reveals the same fine structure, indicating that the local structure of Ni^{2+} was not noticeably changed. However, the edge energy (E_0) of Ni^{2+} solution with carbon dots is 8346.2 eV while that of $Ni(NO_3)_2$ is 8347.5 eV. A decrease in E_0 upon the addition of carbon dots indicates the charge transfer to Ni^{2+}. This indicates that the carbon dots caused a change in electron density and electronic environment of Ni^{2+}. Such changes justified their interaction that led them to a close proximity and enhance the inner filter effect, and consequently the fluorescence quenching of the carbon dots.

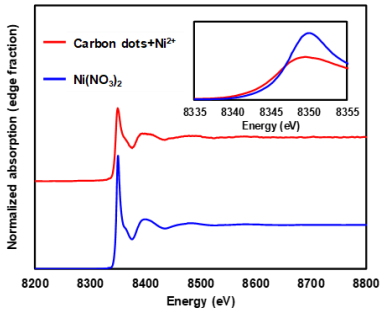

Figure 4.8 Ni *K*-edge XANES spectra of $Ni(NO_3)_2$ and carbon dots/Ni^{2+}. The inset show a magnification at the near edge region of the spectra.

4.1.2.5 Analysis of Ni^{2+} in real water samples

The Ni^{2+} sensing of carbon dots in water samples was further examined and compared with the ICP-OES method. The Ni^{2+} solution (5 µM) was spiked in the three types of bottled drinking water samples. The recovery was calculated and found in a range of 95.64 to 99.22%, which is within the acceptable range (95-105%) (Table 4.4) [172]. The relative standard deviation values ranging from 0.06 to 0.46% were regarded as excellent because they are less than 2%. [172] These results indicate that the obtained carbon dots have a high efficiency for accurate Ni^{2+} detection in real samples.

Table 4.4

Percentage recovery of spiked Ni^{2+} ions using carbon dots in water samples

Sample	Added (µM)	Found (µM)[a]	Found (µM)[b]	Recovery (%)	RSD (%)
DI water	5	5.00±0.24	5.04±0.16	99.21	0.09
Drinking water 1	5	4.78±0.35	4.99±0.23	95.79	0.06
Drinking water 2	5	4.83±0.41	5.05±0.29	95.64	0.20
Drinking water 3	5	5.09±0.19	5.13±0.14	99.22	0.46

[a] from carbon dots/fluorescence spectroscopy. [b] from ICP.

4.1.2.6 Paper-based sensor

A paper-based sensor was fabricated as an easy-to-use and portable test equipment convenient for on-site testing. The carbon dots were coated on the filter papers and various types of metal ion solutions were dropped onto the carbon dot-loaded papers as solid-state sensors. The images show that the paper-based sensor with Ni^{2+} exhibited the darkest blue color whereas other metal ions gave lighter blue color (Figure 4.9a). This suggests that the fluorescence of the paper-based sensor was significantly quenched by Ni^{2+}, consistent with the above results. To investigate the sensitivity of the paper-based sensor, various Ni^{2+} concentrations ranging from 0 to 250 µM were dropped onto the prepared paper-based sensor and the images were then taken under UV lamp for red-green-blue (RGB) value extraction (Figure 4.9b). It was found that the sum of RGB values decreased with increasing Ni^{2+} concentrations. The limit of detection was 43.3 µM, obtained from the RGB curve in the linear range (Figure 4.9c).

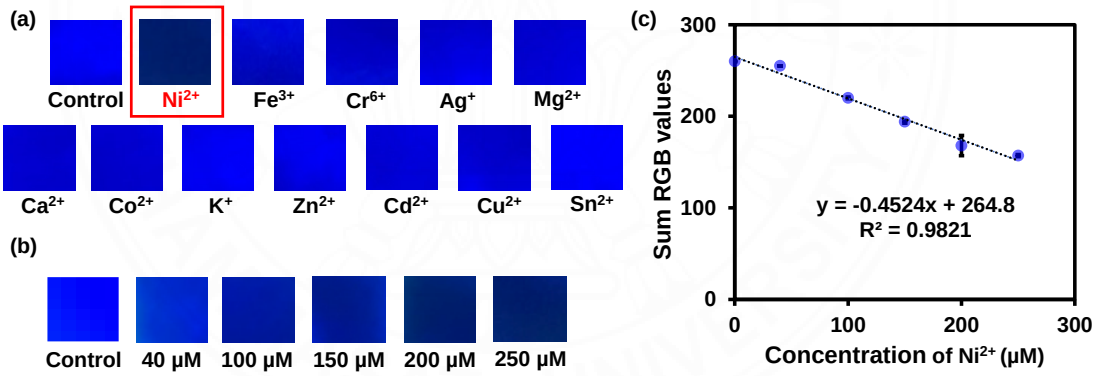

Figure 4.9 Images of paper-based sensor with (a) various metal ion solutions and (b) various concentrations of Ni^{2+}, and (c) plot of sum of RGB values and concentration of Ni^{2+}.

4.2 High-performance Mg^{2+} sensors based on natural rubber-derived, label-free carbon dots

4.2.1 Characterizations

4.2.1.1 Size and morphology characterization

The morphology and the particle size of the carbon dots were characterized by transmission electron microscopy (TEM). The spherical shapes of the carbon dots were well dispersed with diameters in the range from 1 to 4 nm and an average size of 2.4 nm and a lattice spacing of 0.3 nm (Figure 4.10a and b).

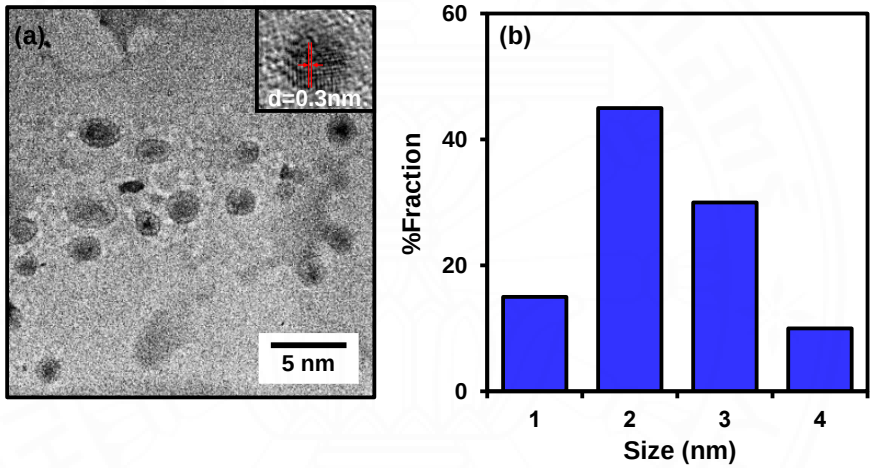

Figure 4.10 (a) TEM image and (b) size distribution of carbon dots.

4.2.1.2 Structural characterization

Chemical functionalities of the prepared carbon dots were first identified via FT-IR spectroscopy and compared with those of natural rubber (Figure 4.11a). The FT-IR spectrum of natural rubber showed the signature signals of C-H stretching, C=C stretching, CH_2 bending, CH_3 bending, =CH out-of-plane bending at 2851-2960, 1631, 1446, 1375, and 830 cm^{-1}, respectively. Other signals, O-H, C=O, O-P-O, and C-O at 3367, 1775, 1240, and 1055 cm^{-1}, belong to other components in natural rubber, such as moisture, proteins, phospholipids, etc [173-176]. The signals of the prepared carbon dots located at 2969, 1587, and 1365 cm^{-1} refer to C-H stretching,

C=C stretching, and C-H bending, respectively. These signals demonstrated sp^3 and sp^2 hybridization carbon in the structure. The signal at 3390, 1100 cm^{-1}, and a shoulder peak at 1730 cm^{-1} are assigned to O-H, C-O, and C=O stretching. Compared to the natural rubber, the FT-IR signals of the carbon dots are much broader and several signals of natural rubber disappeared, indicated the successful transformation of natural rubber to carbon dots. The presence of the O-H and C=O stretching vibrations indicates that the carbon dots consisted of oxygen-containing functional groups, making them water soluble.

The elemental composition of carbon dots was next characterized via X-ray photoelectron spectroscopy (XPS). The survey XPS spectrum showed two relevant signals at 532.1 and 285 eV of O_{1s} and C_{1s} at atomic concentrations of 70.87% and 29.13%, respectively, (Figure 4.11b). Therefore, the carbon dots were solely composed of carbon and oxygen. The high-resolution C_{1s} spectrum was divided into four peaks, which refer to the signals of O-C=O, C=O, C-O, and C-C at 289.1, 288.1, 286.5, and 285 eV, respectively (Figure 4.11c). The high-resolution O_{1s} spectrum exhibited the signals of O-C=O, C-O-C, C-O-H, and C=O at 535.1, 533.7, 532.7, and 531.7 eV, respectively (Figure 4.11d). Peaks at 103.1 and 154.1 eV belonged to Si_{2p} and Si_{2s} due to the use of Si substrate for the XPS sample preparation. Both FT-IR and XPS results are in a good agreement that the carbon dots are dominated by carbon and oxygen and consisted of O-H and C=O groups. These polar functional groups were believed to form during the hydrothermal step and via the use of nitric acid, which can hydrolyze the carbon core [177].

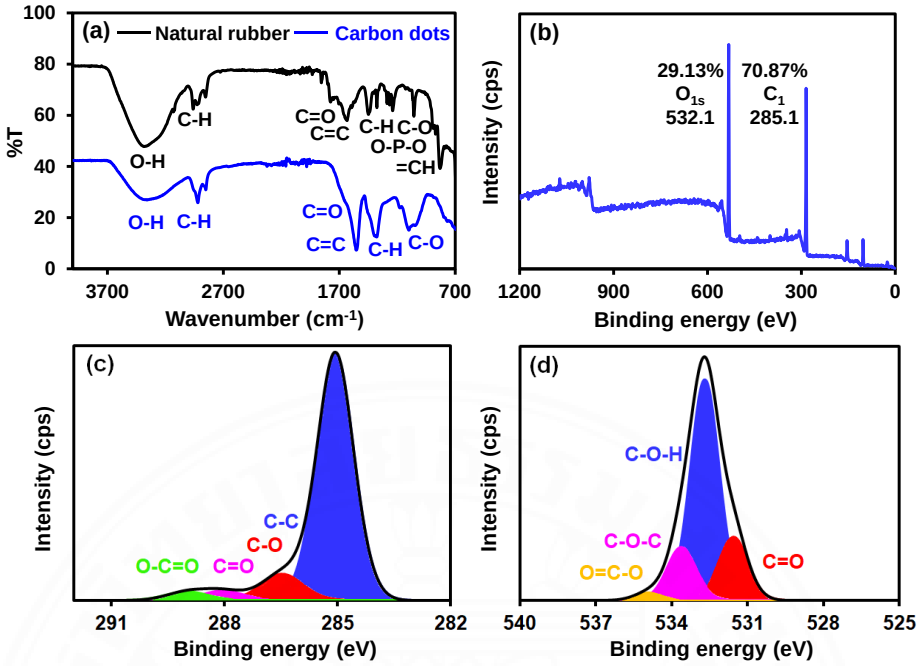

Figure 4.11 (a) FT-IR spectra of natural rubber and carbon dots. (b) Survey XPS spectrum of carbon dots. (c) High resolution of C_{1s} peaks and (d) high resolution of O_{1s} peaks of carbon dots.

4.2.1.3 Optical characterization

Optical properties including absorption and fluorescence emission of carbon dots were characterized using UV-vis and fluorescence spectroscopy. According to the UV-vis spectrum of the obtained carbon dots, it showed a strong optical absorption peak in the UV region while the tail expanded in the visible zone up to 400 nm. The absorption peak was observed at around 240 nm due to the π-π* transition of C=C conjugate hybridization in their structure. Another peak located at about 280 nm refers to the n-π* transition of C=O units (Figure 4.12a). In addition, the fluorescence spectrum of the carbon dots exhibited the maximum emission peak at 414 nm for the excitation at 340 nm with a broad range between 320-600 nm. The emission spectrum gives an evidence that the carbon dots dominantly emitted blue light (the inset in Figure 4.12b). The position of the emission peak shifted when the excitation wavelength was changed to longer wavelengths, demonstrating an excitation-dependent emission (Figure 4.12b). This behavior results from different emissive sites

on the surface of carbon dots. Because carbon dots are sensitive to pH variations in solutions as reported in previous reports [178-180], the pH-dependent fluorescence emission of carbon dots was studied (Figure 4.12c). The result showed that a pH of 11 yielded the highest fluorescence emission intensity while the fluorescence emission intensity significantly decreased in strong acid and basic conditions. To investigate the stability of the carbon dots for practical applications, the carbon dot solution was stored under ambient conditions for 6 weeks and the emission intensity of this solution was recorded every week. The result showed that the emission intensity did not significantly change for 6 weeks (Figure 4.12d). This suggested that the obtained carbon dots are suitable fluorophores for applications that require long-term photostability because they did not photobleach for at least 6 weeks.

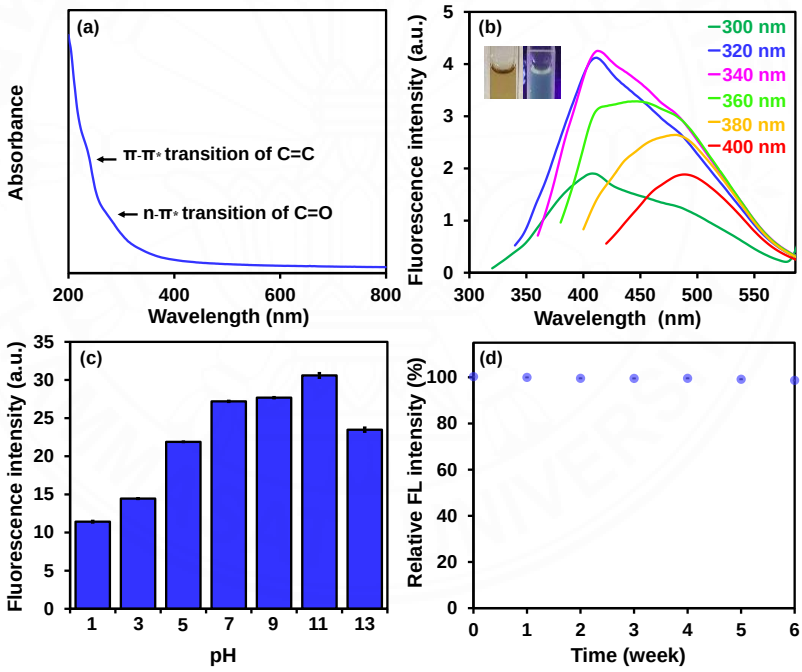

Figure 4.12 (a) UV-vis absorption spectrum of carbon dots. (b) Fluorescence emission spectra of carbon dots at various wavelengths of excitation with inset figures of carbon dot solutions under visible light (left) and UV light (right). (c) Fluorescence emission intensities of carbon dots with various pH. (d) Photostability of carbon dots in solutions.

4.2.2 Mg^{2+} ion sensing

4.2.2.1 Selectivity and interference tests for Mg^{2+} ion sensing

Due to the unique properties of carbon dots, especially their selective interaction with metal ions, they can be used as metal ion sensors. To study the potential of the carbon dots as sensors, various metal ions, including K^{+}, Mg^{2+}, Sn^{2+}, Zn^{2+}, Ag^{+}, Ca^{2+}, Cd^{2+}, Cu^{2+}, Ni^{2+}, Fe^{3+}, and Cr^{6+}, were chosen to examine the selectivity of carbon dots. The result showed that only Mg^{2+} could significantly quench the fluorescence intensity of carbon dots by more than 80% compared to other tested metal ions, indicating that carbon dots were highly selective to Mg^{2+} (Figure 4.13a).

To confirm the selectivity of carbon dots, interference experiment was then studied by measuring the fluorescence emission intensity of the carbon dots in the presence of Mg^{2+} and coexisting metal ions, including Fe^{3+}, Cr^{6+}, Ca^{2+}, Ni^{2+}, Cu^{2+}, Sn^{2+}, Zn^{2+}, Ag^{+}, K^{+}, and Cd^{2+}, as interferences. The result showed that the fluorescence emission intensity of carbon dots still selective to Mg^{2+} even in the presence of the metal interferences (Figure 4.13b and c). This demonstrated high anti-interference of carbon dots to other metal ions and confirmed the effective sensing potential of carbon dots.

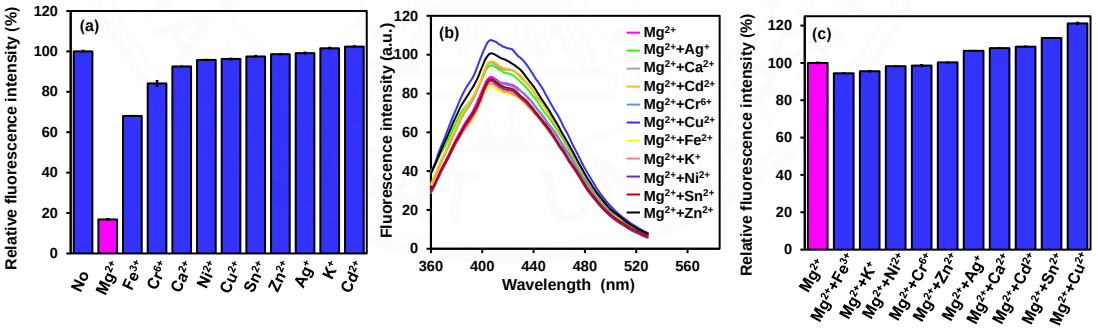

Figure 4.13 (a) Relative fluorescence emission intensities of carbon dots with the addition of various metal ions. (b) Fluorescence emission spectra of carbon dots mixed with Mg^{2+} and interferences. (c) Fluorescence emission intensities.

4.2.2.2 Sensitivity test for Mg^{2+} ion sensing

Their sensitivity was further studied with various concentrations of Mg^{2+} solution ranging from 0 to 250 µM. The result demonstrated that the fluorescence intensity of carbon dots decreased with increasing concentration of Mg^{2+}. The quenching rate of carbon dots had a good linear relationship to the concentration of Mg^{2+} ($R^2 = 0.9908$) with a limit of detection (LOD) of 4.3 µM (Figure 4.14). The selectivity of the carbon dots towards Mg^{2+} is believed to arise from ion-dipole interactions between Mg^{2+} and surface functional groups. Phenolic and oxygen of the carbonyl groups were reported to interact strongly to Mg^{2+} [181]. This is possible because our carbon dots contained aromatic units and carbonyl groups as proved by the FT-IR, XPS, and UV-vis results. Furthermore, Mg^{2+} has a suitable size that possibly fits the cavity between functional groups in carbon dots as the size-controlled ion detection of the carbon dots has been observed in previous studies [182, 183].

The linear range and LOD of various Mg^{2+} ion sensors are summarized in Table 4.5. Our LOD is better than those from carbon paste electrode [184] and ion-channel mimetic sensors [185]. Although the LODs from tryptophan functionalized gold nanoparticles [186] and PVC membrane trapped chlorophyll[187] are better than ours, our carbon dots were much cheaper and simpler to prepare and required less fabrication steps. A report by Sadhanala *et al.* is the first to describe the Mg^{2+} sensor using carbon dots with a detection limit of 39 µM [188]. Although our work is the second on using the carbon dots, our carbon dots are much greener because theirs were prepared from more toxic and more expensive naphthalene-1-boronic acid and catechol. Furthermore, our LOD is almost ten-fold better than their LOD. Interestingly, we also fabricated the paper-based sensors as discussed later to demonstrate the practicality.

Table 4.5

Summary of Mg^{2+} ion sensors

Materials	Linear range (μM)	LOD (μM)	Ref.
Carbon paste electrode	1×10^{-3}-10,000	5×10^{-4}	[184]
Tryptophan functionalized gold nanoparticles	0.1-0.45	0.2	[189]
PVC membrane trapped chlorophyll	10-100,000	3.2	[187]
Ion-channel mimetic sensors	100-100,000	50.12	[185]
Boron-doped carbon dots	0-300	39	[190]
Natural rubber-derived carbon dots	0-40	4.3	This work

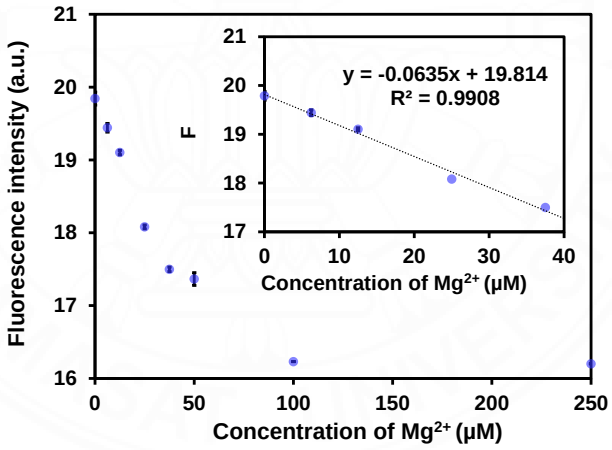

Figure 4.14 Fluorescence emission intensities with inset figure showing fluorescence intensities at various Mg^{2+} concentrations in the linear range.

4.2.2.3 The response time for Mg^{2+} ion sensing

The time response of the carbon dots for Mg^{2+} detection with various metal ions was studied. Their fluorescence emission intensities were recorded every 50 seconds, a minimum time of each spectrum scan. The result shows that only

the fluorescence intensity of carbon dots in the presence of Mg^{2+} was immediately decreased at the first scan and remained constant, showing the high response for Mg^{2+} detection (Figure 4.15a). This suggests that the obtained carbon dots showed the fast and selective detection of Mg^{2+}. Furthermore, the fluorescence emission intensities of the carbon dots with various Mg^{2+} concentrations ranging from 100 to 500 µM were recorded at the same rate. As shown in Figure 4.15b, all concentrations of Mg^{2+} could quench the fluorescence intensities of carbon dots within 50 seconds as we have described earlier. These results confirmed a high response of the carbon dots for the detection of Mg^{2+} within 50 seconds.

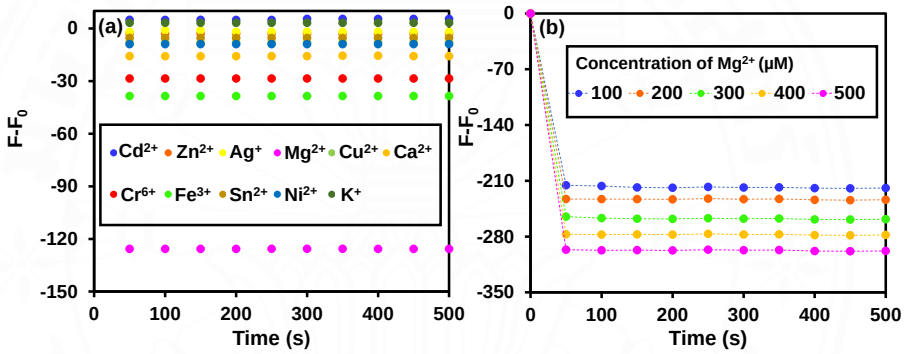

Figure 4.15 (a) Time profiles of fluorescence emission of the carbon dots in the presence of tested metal ions. (b) Time profiles of fluorescence emission of the carbon dots with different concentrations of Mg^{2+}.

4.2.2.4 The quenching mechanism

To determine the fluorescence quenching phenomena of carbon dots by Mg^{2+}, the quenching mechanism was further studied. Mg^{2+} with and without carbon dot solutions were recorded at 280 nm using UV-vis spectrophotometry and exhibited the linear relationship, following the Beer-Lambert law (Figure 4.16a and b). The slopes of both solutions, equivalent to an absorption coefficient, are similar, indicating no formation of the complex between Mg^{2+} and carbon dots took place [160].

This suggests a dynamic interaction instead of a static complex formation between the carbon dots and Mg^{2+}.

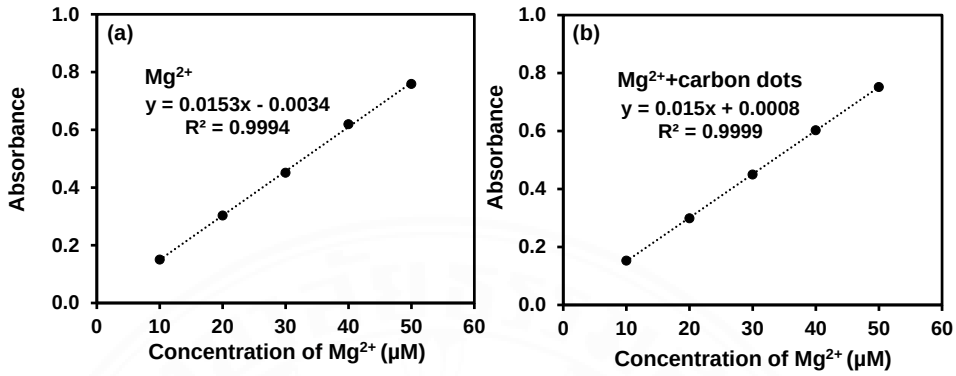

Figure 4.16 UV-vis absorption spectra of (a) Mg^{2+} and (b) Mg^{2+}-carbon dot solutions at 280 nm.

XANES was next used for the investigation on the interaction between carbon dots and Mg^{2+} (Figure 4.17). The absorption edge energy (E_0) of Mg^{2+}/carbon dots was measured and compared with those of $MgCl_2$ and $MgCO_3$ as the standard samples. It was found that the E_0 of Mg^{2+}/carbon dots (1310.3 eV) is different from that of $MgCl_2$ (1308.7 eV), indicating the difference in electron density and electronic environment of Mg^{2+} ions in the presence of carbon dots. Since the Mg^{2+}/carbon dot mixture was purified by dialysis, there were virtually no free Mg^{2+} ions in the solution. This confirms that the Mg^{2+} ions in the carbon dot solution interacted with the carbon dots, leading to a change in E_0 value with respect to that of $MgCl_2$. Furthermore, the E_0 of Mg^{2+}/carbon dots is close to that of $MgCO_3$ (1310.3 eV), suggesting the Mg^{2+} ions in the presence of carbon dots might be in the oxygen-rich environment. This finding agrees well with the FT-IR and XPS results that the carbon dots were oxygen-rich and their oxygen-rich groups might be in a close proximity to Mg^{2+} ions and caused a change of electronic environment around Mg^{2+} ions. In addition, the absorption features of Mg^{2+}/carbon dots around 1306 to 1354 eV is different from those of $MgCl_2$, implying different local environment around Mg^{2+} ions in the presence of carbon dots, as compared to $MgCl_2$. These results, which also agree with the above

UV-vis results, suggest that the carbon dots and Mg^{2+} ions interacted dynamically and had sufficient interactions possibly through ion-induced dipole interactions, causing a change of emissive states and leading to the fluorescence quenching. Although there is no enough information at this stage to specifically determine the type of interactions between carbon dots and Mg^{2+} ions, we can conclude that the carbon dots and Mg^{2+} ions possess unique interactions that can be utilized for sensing applications. Further studies must be carried out requiring other specialized techniques, such as extended X-ray absorption fine structure, which can give us the detailed information of the local environment of Mg^{2+} ions.

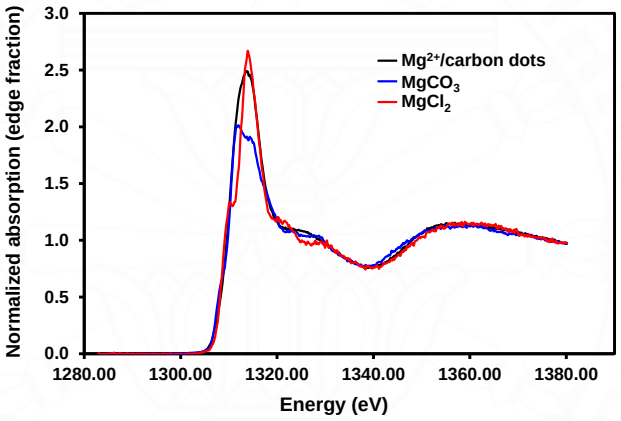

Figure 4.17 Mg *K*-edge XANES spectra of Mg^{2+}/carbon dots, $MgCO_3$, and $MgCl_2$.

4.2.2.5 Analysis of Mg^{2+} in real water samples

The practical use of carbon dots in real water samples was next evaluated using three types of bottled drinking water. Three types of drinking water were used to prepare the carbon dot solution. The Mg^{2+} solution (5 µM) was then spiked in all samples because there was only a trace amount of Mg^{2+} in the drinking water samples, which is below the detection limit, and their fluorescence intensities were recorded using fluorescence spectroscopy. The result from this method was compared with the ICP-OES method as a reference method to calculate the percentage recovery and the relative standard deviation values. As shown in Table 4.6, we found that the percentage recovery was in the range of 97.21 to 99.21%, which is within the acceptable

range (95-105%) [172]. The relative standard deviation values were excellently found in a range between 0.26 to 0.61, which are less than 2% [172]. These results indicated that the prepared carbon dots have high efficiency for Mg^{2+} detection in drinking water samples with a high accuracy.

Table 4.6

Percentage recovery and the relative standard deviation values of spiked Mg^{2+} solution using carbon dots in drinking water samples

Sample	Added (μM)	Found (μM)[a]	Found (μM)[b]	Recovery (%)	RSD (%)
DI water	5	5.00±0.37	5.04±0.21	99.21	0.61
Drinking water 1	5	4.89±0.16	4.98±0.16	98.19	0.26
Drinking water 2	5	4.90±0.49	4.99±0.28	98.19	0.83
Drinking water 3	5	4.87±0.35	5.01±0.21	97.21	0.61

[a] from fluorescence spectroscopy. [b] from ICP.

4.2.2.6 Paper-based sensor

Because filter paper is cheap and easy for reagent immobilization and on-site testing, it has been attracting attention for use as a substrate for fluorescence-based sensing. Thus, we fabricated paper-based metal ion sensors from the carbon dot-loaded filter papers by dropping carbon dot solution on the papers. Metal ion solutions, including Ag^{+}, Ca^{2+}, Cd^{2+}, Cu^{2+}, Mg^{2+}, Sn^{2+}, Zn^{2+}, Ni^{2+}, Cr^{6+}, Fe^{3+}, and K^{+}, were dropped on the fabricated papers and they were taken under UV light using an iPhone camera. The results show that the paper-based sensors produced light blue images except Mg^{2+}, showing the darkest blue (Figure 4.18a). This indicates that paper-based sensors were significantly quenched by Mg^{2+} which is consistent with the above results. Moreover, the sensitivity of the paper-based sensor was also investigated by dropping various Mg^{2+} concentrations ranging from 0 to 200 μM and the images were next taken under UV light for red-green-blue (RGB) extraction (Figure 4.18b). The result shows that the sum RGB values decreased with increasing the concentration of

Mg^{2+} and the detection limit of Mg^{2+} was calculated as 8.01 µM from the sum RGB curve in the linear range (Figure 4.18c).

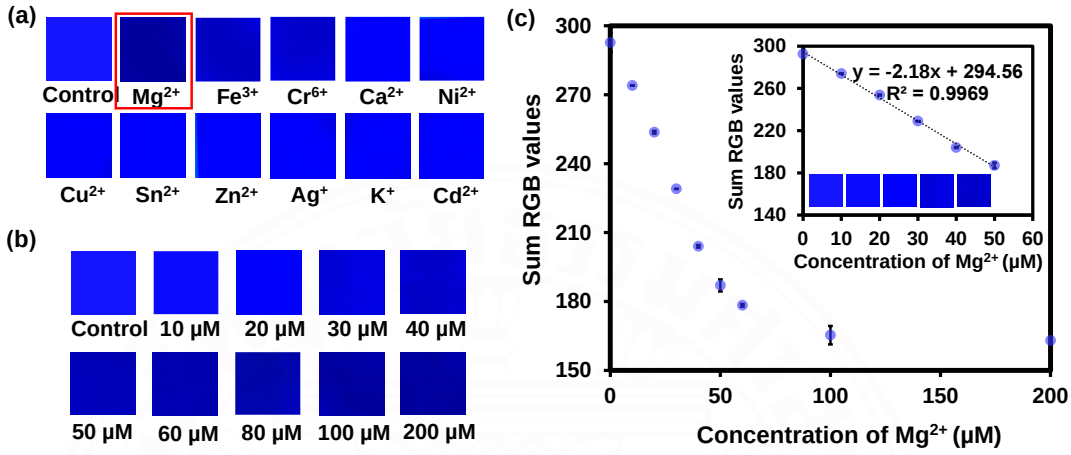

Figure 4.18 Images of paper-based sensor with (a) various metal ions and (b) various Mg^{2+} concentrations. (c) Plots of RGB values extracted from paper-based sensor. Inset shows RGB values with various Mg^{2+} concentrations ranging between 0 and 50 µM as a linear plot.

4.3 Enhancing the specific capacitance and cycling stability of zinc oxide-based supercapacitors using gamma irradiated, amine-passivated carbon dots

4.3.1 Characterizations

4.3.1.1 Size and morphology characterization

(1) Carbon dots

The morphology and particle size of all CDs were characterized by TEM (Figure 4.19a-e). The images showed that all CDs were mostly spherical with an average diameter of approximately 4, 4, 3.6, 24.8, and 29.8 nm, respectively (Figure 4.19f-j). The surface passivation of EDA led to larger nanoparticle size. Obviously, the nanoparticles in CDs-EDA-50 and CDs-EDA-200 showed darker carbon core and lighter outer layer, which is the EDA passivated layer. The thicknesses of the outer layers of CDs-EDA-50 and CDs-EDA-200 are 8 and 12.7 nm. The zeta potentials of CDs, CDs-50, CDs-200, CDs-EDA-50, and CDs-EDA-200 were -12, 6.8, 8.1, 14.7, and 3.2 mV, respectively. The positive zeta potential values after modification of CDs resulted from the re-polymerization of functional groups on surfaced pristine CDs and the passivation of EDA also provided positively charged ammonium groups.

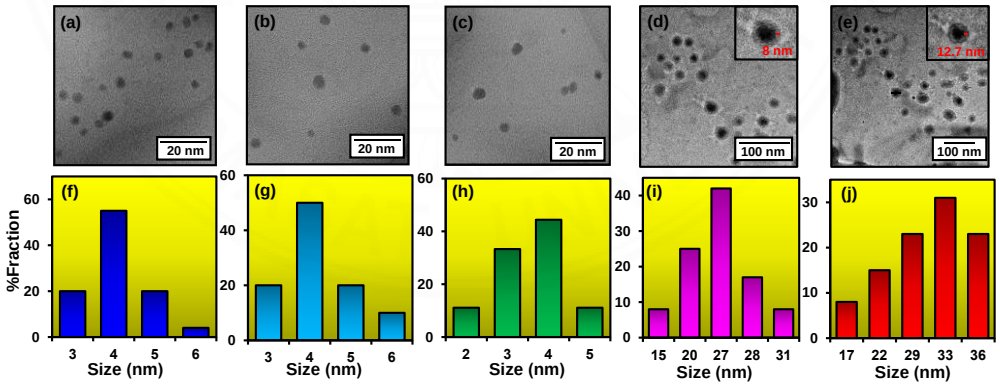

Figure 4.19 TEM images with inset figures showing the interlayer distance of representative (a) CDs, (b) CDs-50, (c) CDs-200, (d) CDs-EDA-50, and (e) CDs-EDA-200. Size distribution of (f) CDs, (g) CDs-50, (h) CDs-200, (i) CDs-EDA-50, and (f) CDs-EDA-200.

(2) Zinc oxide (ZnO) nanoparticles

ZnO nanoparticles were synthesized from zinc acetate dihydrate and sodium hydroxide via the sol-gel method (Figure 4.20a). The SEM image of the synthesized ZnO nanoparticles is shown in Figure 4.20b. The image shows the agglomeration of ZnO nanoparticles, which is similar to the previous report [191]. Furthermore, the crystalline structure and purity of the synthesized ZnO nanoparticles were confirmed by the XRD pattern. The XRD pattern of the synthesized ZnO nanoparticles was shown in Figure 4.20c and compared with that of zincite (COD ID: 2300112) as a benchmark [192]. All the peaks from the synthesized ZnO nanoparticles matched well with those of zincite. Moreover, the XRD result from ZnO nanoparticles reveals no impurity peak, confirming the successful synthesis of ZnO nanoparticles with no detectable impurity by this process. To evaluate the average crystallite size of the synthesized ZnO nanoparticles, the maximum intense (101) peak is utilized using the Debye-Scherrer formula [193], as shown in Equation 9:

$$d = \frac{k\lambda}{\beta \cos\theta} \tag{9}$$

where d is the average crystallite diameter of ZnO nanoparticles, k is the Scherrer constant, which is 0.9 for spherical particles, λ is the wavelength of X-ray (1.5418 Å), β is the full width at half maximum (FWHM), which is determined from the 2θ value of maximum intensity peak, and θ is the Bragg's diffraction angle. The average crystallite size of the synthesized ZnO nanoparticles was calculated to be 22.45 nm.

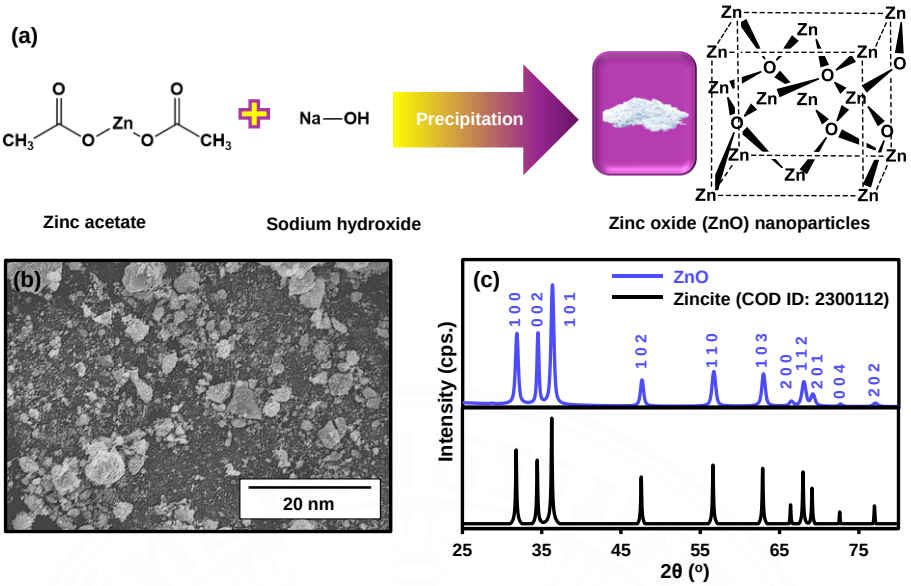

Figure 4.20 (a) Schematic of ZnO nanoparticle synthesis. (b) SEM image of the synthesized ZnO nanoparticles. (c) XRD patterns of the synthesized ZnO nanoparticles and zincite (COD ID: 2300112).

4.3.1.2 Structural characterization

Due to the high energy of gamma irradiation, it has been applied in various ways, including material structural modifications. In this work, we chose this technique to modify CDs in the presence of EDA prepared from polyurethane and applied the modified CDs in the ZnO-based supercapacitors. Interestingly, the gamma-irradiated CDs have never been employed for this application. Several phenomena, including structural modifications, bond breaking, free radical formation, cross-linking, and chain scission, occur when gamma rays interact with the CDs, resulting in the re-polymerization and modification of CDs. Moreover, the modified CDs were highly nitrogen-doped because of the passivation of EDA. Due to the use of polyurethane and EDA containing nitrogen as a precursor and a doping agent, respectively, and sulfuric acid containing sulfur as a reagent for the synthesis of CDs, the obtained CDs were expected to show nitrogen and sulfur in the framework and surface functional groups.

The functional groups on the surface of all prepared CDs including CDs, CDs-50, CDs-200, CDs-EDA-50, and CDs-EDA-200 were investigated using FT-IR spectroscopy. Figure 2a revealed the bands at 1610 cm^{-1} (C=O/C=N) and 1050 cm^{-1} (C-O/C-N) in CDs, CDs-50, CDs-200, CD-s-EDA-50, and CDs-EDA-200. The obvious bands at 3200-2900 cm^{-1} (O-H/N-H/C-H), 1530 cm^{-1} (C=C), and 825 cm^{-1} (N-H wagging) were only detected in the spectra of CDs-EDA-50 and CDs-EDA-200, which were not observed in those of CDs, CDs-50, and CDs-200, confirming that EDA was incorporated in the CDs upon gamma irradiation. The increase in sp^2 hybridized carbon after gamma irradiation and amine passivation was also in an agreement with previous reports [113, 114]. Furthermore, a signal at 1610 cm^{-1} was more apparent in CDs-EDA-50 and CDs-EDA-200, which is an indicative of the imine formation after gamma irradiation/amine passivation [112]. Gamma irradiation in the absence of EDA, on the other hand, did not yield a noticeable change to the FT-IR signals of the CDs-50 and CDs-200 with respect to the CDs. The amine passivation without the assistance of gamma irradiation did not effectively take place. All prepared CDs showed C-S bond at 602 cm^{-1} because of the use of sulfuric acid as a reagent for the synthesis of CDs. The presence of nitrogen-containing groups suggests the successful gamma irradiation and amine passivation of CDs and the presence of polar functional groups on the surface of CDs, such as carbonyl and hydroxyl groups, are responsible for their high solubility in water and polar organic solvents.

To gain more information of the gamma irradiation/amine passivation effects, XPS was also used to characterize all CDs. Figure 1b represented the survey XPS spectra showing four relevant signals of O_{1s}, N_{1s}, C_{1s}, and S_{2p} at 531, 400, 285, and 168 eV, respectively. The nitrogen atomic concentrations of only CDs-EDA-50 and CDs-EDA-200 were above 17%, indicating that EDA was effectively incorporated in the CDs. The high-resolution O_{1s} spectra of all samples showed the presence of C=O, O=C-N, and C-O-C (Figure 2c) whereas the high-resolution N_{1s} spectra revealed the graphitic-N, aliphatic N-C, and N-H groups (Figure 2d). The high-resolution C_{1s} signal of all samples can be deconvoluted into four Gaussian peaks, which are C=C/C-C, C-N, C=O, and C-O (Figure 2e). The C-N and C=O peaks at 286.5 and 288 eV were noticeably more pronounced in the CDs-EDA-50 and CDs-EDA-200, indicating the successful amine passivation under gamma irradiation.

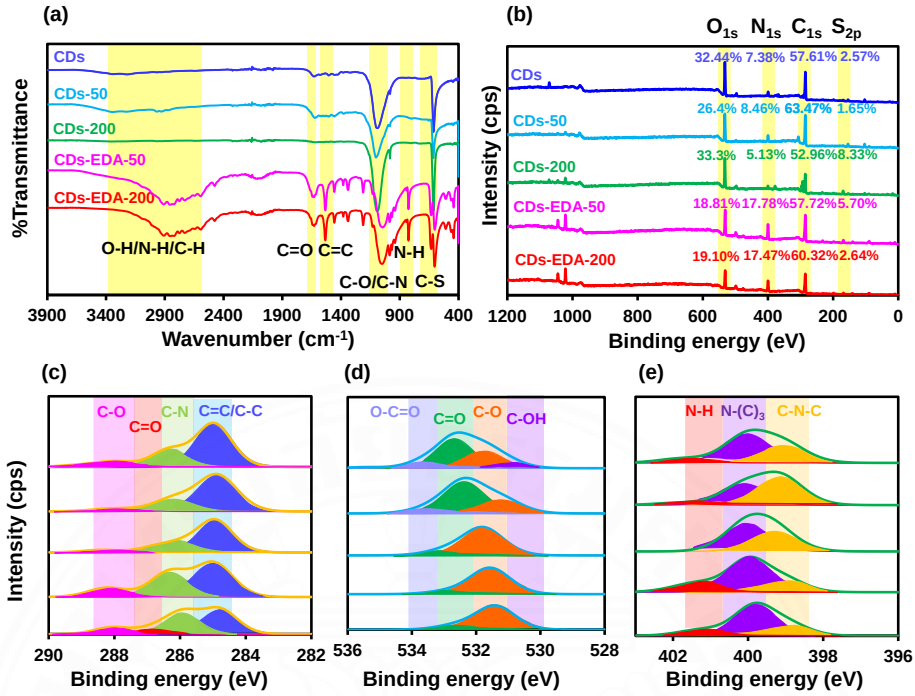

Figure 4.21 (a) FT-IR spectra, (b) survey XPS spectra, (c) C_{1s}, (d) O_{1s}, and (e) N_{1s} spectra of CDs, CDs-50, CDs-200, CDs-EDA-50, and CDs-EDA-200.

4.3.1.3 Optical characterization

Optical absorption of all prepared CDs was investigated using UV-vis spectroscopy. The UV-Vis spectra of CDs, CDs-50, CDs-200, CDs-EDA-50, and CDs-EDA-200 are shown in Figure 4.22a-e. The shoulder absorption peak at 250 nm was assigned to π-π* transition of the aromatic sp^2 carbon while the absorption peak at around 300 nm was caused by the n-π* transition. The n-π* transition was apparent only in CDs-50 and CDs-200 whereas the π-π* transition was dominant in CDs-EDA-50 and CDs-EDA-200. However, both n-π* and π-π* transitions were observed in the CDs. These results revealed that gamma irradiation and amine passivation caused some structural changes in the CDs, leading to a change to UV-vis absorption. The fluorescence emission of all CDs was investigated using fluorescence spectroscopy. The highest fluorescence intensity of CDs, CD-50, CDs-200, CDs-EDA-50, and CDs-EDA-200 was observed at 494, 489, 485, 483, and 477 nm, respectively, when using an excitation wavelength of 380 nm (Figure 4.22f-j). The gamma-irradiated, amine-

passivated CDs showed the blue-shifted fluorescence emission as compared to the unmodified CDs, which has been well known that the amine-passivated CDs dominantly contained blue emissive sites [194, 195]. From the FT-IR, XPS, UV-vis, and fluorescence results, we concluded that the gamma irradiation and amine passivation increased an aromaticity and a change in emissive states in the CDs structure and these would consequently attribute to a change in physical and electrical properties.

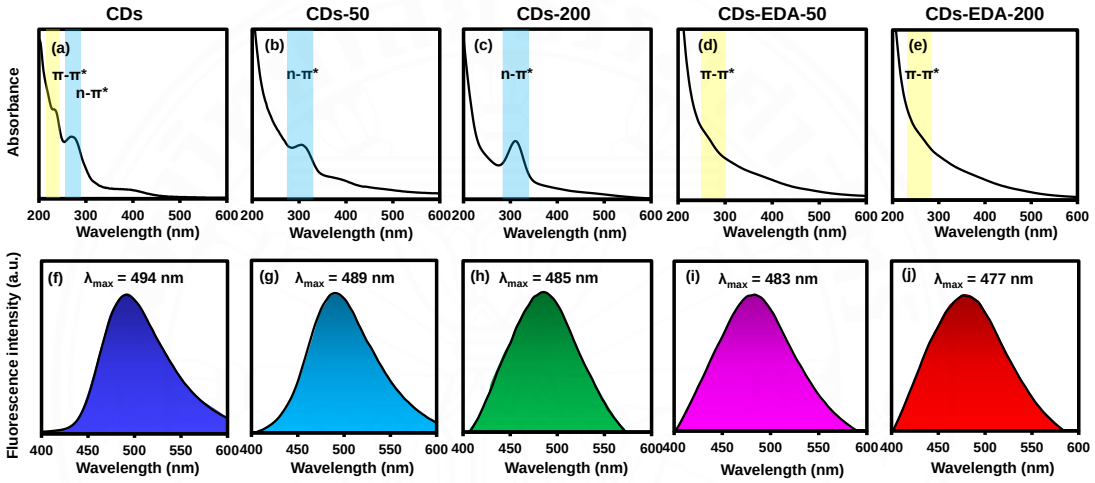

Figure 4.22 UV-vis absorption spectra of (a) CDs, (b) CDs-50, (c) CDs-200, (d) CDs-EDA-50, and (e) CDs-EDA-200. Fluorescence emission spectra of (f) CDs, (g) CDs-50, (h) CDs-200, (i) CDs-EDA-50, and (j) CDs-EDA-200.

4.3.2 Electrochemical measurements

4.3.2.1 Electrochemical measurements of the prepared electrodes

The electrochemical measurements of the prepared electrodes were performed using CV in a potential window ranging from -0.3 to 0.3 V. The CDs, CDs-50, CDs-200, CDs-EDA-50, and CDs-EDA-200 were mixed with ZnO nanoparticles to obtain ZnO-CDs, ZnO-CDs-50, ZnO-CDs-200, ZnO-CDs-EDA-50, and ZnO-CDs-EDA-200 electrodes. The ZnO alone was used as a control electrode. The CV curves of ZnO, ZnO-CDs, ZnO-CDs-50, ZnO-CDs-200, ZnO-CDs-EDA-50, and ZnO-CDs-EDA-200 electrodes are shown in Figure 4.23a, providing the specific

capacitances of 17.89, 25.44, 26.27, 25.42, 34.76, and 55.78 F g^{-1}, respectively, at a scan rate of 5 mV s^{-1}. Therefore, this verified that the gamma-irradiated, amine-passivated CDs significantly improved the supercapacitor performance. Compared to the pristine ZnO electrode, the specific capacitances of ZnO-CDs-EDA-50, and ZnO-CDs-EDA-200 were elevated by 194% and 312%, emphasizing the importance of irradiation dose and amine passivation. However, the gamma irradiation alone without EDA yielded the CDs that were not significantly beneficial to the supercapacitor as compared to a combination of both gamma irradiation and amine passivation. Since the ZnO-CDs-EDA-200 electrode was the best, it was further tested in three different concentrations of KOH solutions as electrolytes, including 1 M, 3 M, and 6 M. The results showed that the 6 M KOH system provided the highest specific capacitance of 55.78 F g^{-1}, while 1 M and 3 M KOH solutions provided the specific capacitances of 34.22 and 34.49 F g^{-1}, respectively (Figure 4.23b). This resulted from the fact that an increase in the concentration of KOH led to an enhancement in ionic conductivity of the electrolyte [196].

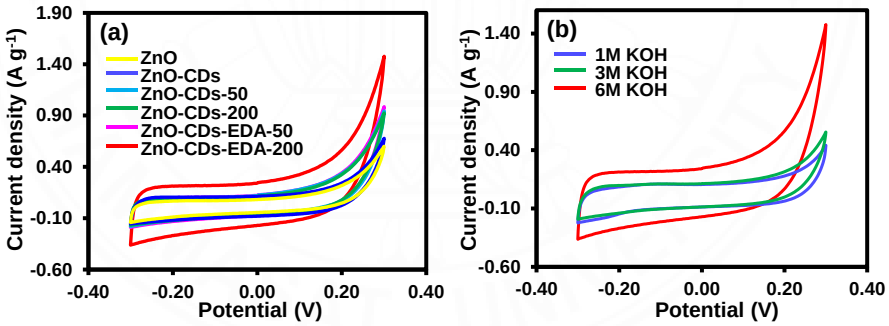

Figure 4.23 CV profiles of (a) ZnO, ZnO-CDs, ZnO-CDs-50, ZnO-CDs-200, ZnO-CDs-EDA-50, and ZnO-CDs-EDA-200 electrodes in 6 M KOH at 5 mV s^{-1}. (b) ZnO-CDs-EDA-200 electrode in 1 M, 3 M, and 6 M KOH at 5 mV s^{-1}.

4.3.2.2 The effects of scan rate and current density on the specific capacitance of the prepared electrodes

To study the effects of scan rate on the specific capacitance of ZnO-CDs-EDA-200 electrode, it was tested using CV at 5, 10, 30, 50, 70, and 100 mV s^{-1} (Figure 4.24a). We found that the specific capacitance decreased with the increasing scan rate. This is because of the limited ion adsorption/desorption and charge transfer processes between electrode and electrolyte at high scan rates. To obtain more electrochemical information, the GCD curves of ZnO-CDs-EDA-200 were measured at different current densities of 0.3, 0.4, 0.5, 0.8, 1, 1.2, and 2 A g^{-1} (Figure 4.24b). As the current density was increased, the charging/discharging time became decreasing for the same reason described above. A small IR drop of about 0.07 V was observed, indicating a low series resistance in the supercapacitors. The charging time is longer than the discharging time, which is an indication of slow faradaic reaction from the ZnO nanoparticles, compared to the EDLC mechanism.

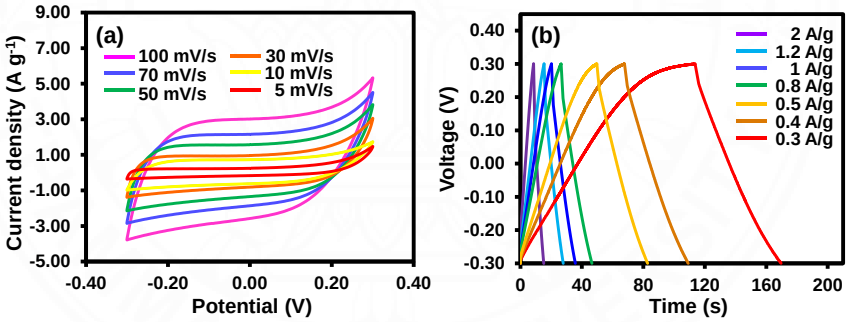

Figure 4.24 (a) CV profiles of ZnO-CDs-EDA-200 electrode in 6 M KOH at 100, 70, 50, 30, 10, and 5 mV s^{-1}. (b) GCD curves of ZnO-CDs-EDA-200 electrode in 6 M KOH at 0.3, 0.4, 0.5, 0.8, 1, 1.2, and 2 A g^{-1}.

4.3.2.3 The series resistance of the prepared electrodes

To evaluate the series resistance of all electrodes, the EIS technique was used. The Nyquist plots of ZnO, ZnO-CDs, ZnO-CDs-50, ZnO-CDs-200, ZnO-CDs-EDA-50, and ZnO-CDs-EDA-200 were shown in Figure 4.25. The intersection point on the x-axis corresponds to the intrinsic ohmic resistance of the

internal resistance or equivalent series resistance (ESR) that originates from the resistance of various sources, such as electrolyte, internal resistance of electrode material, and contact resistance between electrode and electrolyte [197]. The ZnO-CDs-EDA-200 electrode showed the lowest ESR value of 4.21 Ω, providing the lowest internal resistance, while ZnO, ZnO-CDs, ZnO-CDs-50, ZnO-CDs-200, ZnO-CDs-EDA-50 showed the ESR values of 6.77, 6.52, 5.07, 5.98, and 4.80 Ω, respectively. This ranking also agreed well with that of the specific capacitance. These results indicated that the addition of CDs which were modified by gamma irradiation and amine passivation reduced the resistance of the electrodes and suggested some favorable effects offered by the gamma-irradiated, amine-passivated CDs, which will be further verified through several electrochemical analyses below.

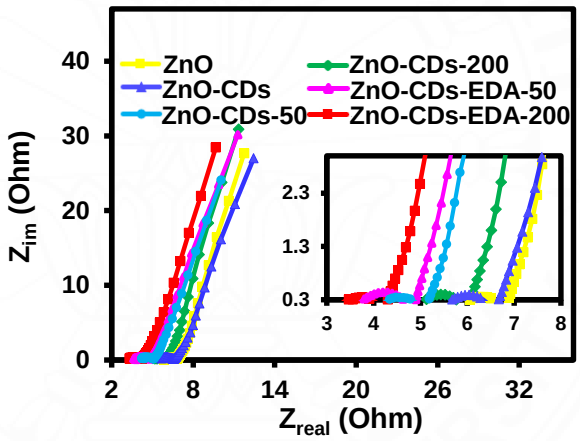

Figure 4.25 Nyquist plot of ZnO, ZnO-CDs, ZnO-CDs-50, ZnO-CDs-200, ZnO-CDs-EDA-50, and ZnO-CDs-EDA-200 electrode in 6 M KOH.

4.3.2.4 The cycling stability of the prepared electrodes

A long cycle life is one of the main factors for supercapacitor operation. The cycling stability was then investigated by GCD at 1 A g^{-1} (Figure 43). It can be seen that the ZnO-CDs-EDA-200 electrode retained 99.87% of the initial capacitance even it was repeated for 8500 cycles, which is considered an excellent cycling stability, while the ZnO, ZnO-CDs, ZnO-CDs-50, ZnO-CDs-200, and ZnO-CDs-EDA-50 electrodes retained 87.41, 90.04, 97.30, 93.78, and 99.71% of their initial

capacitances, respectively. It is clear that the incorporation of gamma-irradiated, amine-passivated CDs improved not only the specific capacitance but also the cycling stability of the supercapacitor. Moreover, this also confirmed a long period of use from our supercapacitors for practical applications.

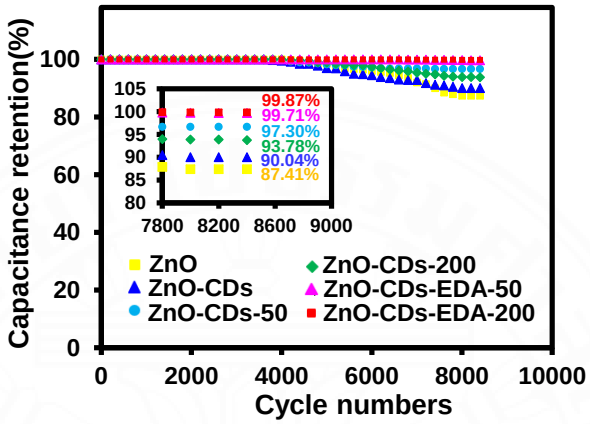

Figure 4.26 Cycling stability of ZnO, ZnO-CDs, ZnO-CDs-50, ZnO-CDs-200, ZnO-CDs-EDA-50, and ZnO-CDs-EDA-200 electrode in 6 M KOH.

4.3.3 Electrochemical analysis of the prepared electrodes

4.3.3.1 Charge storage mechanisms

To deeply gain information on the ion transport and charge storage mechanisms of the electrodes and the effects of gamma-irradiated, amine-passivated CDs, electrochemical analysis was performed using CV profiles with varying scan rate. The ion transport and charge storage can occur via (a) surface-reaction contribution (electric double-layer and near-surface redox reactions) and (b) diffusion-controlled process (ion insertion/extrusion in electrode materials). The relationship between current response (i) and scan rate (v) was studied according to the Cottrell equation (Equation 10) [198].

$$i = \frac{nFAC_o\sqrt{D_o}}{\sqrt{\pi t}} \qquad (10)$$

where *n* is the number of mole electron, *F* is the Faraday's constant, *A* is the electrode area (cm^2), D_o is the diffusion coefficient of the electroactive species ($cm^2\ s^{-1}$), C^0 is the bulk concentration of the electroactive species (mol cm^{-3}), and *t* is the time (s). Equation 10 can be shortened as $i = at^{-1/2}$ where a is a collection of constants. The term $t^{-1/2}$ can be replaced by $v^{1/2}$, providing $i = av^{1/2}$. A general case can be written as Equation 11, which can be used to investigate the contribution of diffusion and surface capacitive processes.

$$i = av^b \tag{11}$$

where a and *b* are variable parameters. The *b*-values can be obtained from the slopes of the plot of log i vs log v (Figure 4.27a). The ideal exponent *b* will have a value of 0.5 for the diffusion-controlled process and 1 for the surface reaction [199]. Clearly, the ZnO-CDs-EDA-200 electrode provided the highest *b*-value (0.8403), followed by ZnO-CDs-EDA-50 (0.8279), ZnO-CDs (0.8237), ZnO-CDs-50 (0.8111), ZnO-CDs-200 (0.8107), and ZnO (0.7765), respectively. This analysis indicates that the both surface- and diffusion-controlled processes contributed to the ion transport and charge storage mechanisms and the gamma-irradiated, amine-passivated CDs further enhanced the surface process as the *b*-values of ZnO-CDs-EDA-50 and ZnO-CDs-EDA-200 were among the highest ones. To further confirm this statement, the peak currents (i_p) and the square root of scan rate ($v^{1/2}$) were plotted based on the Randles-Sevcik diffusion equation (Equation 12) (Figure 4.27b) [200].

$$i_p = 0.436nFAC^0\left(\frac{nFvD_0}{RT}\right)^{\frac{1}{2}} \tag{12}$$

where *R* is the gas constant and *T* is temperature. For an adsorption-controlled process, linear plots of the peak current (i_p) and scan rate (v) were constructed based on Equation 13 [201].

$$i_p = \frac{n^2F^2}{4RT}vA\acute{\Gamma} \tag{13}$$

where $\acute{I}$ refers to the surface coverage of the adsorbed species (mol cm^{-2}).

Both Figures 4.27b and c show high coefficients of determination (R^2), indicating that both surface- and diffusion-controlled processes contributed to the ion transport and charge storage mechanisms, consistent with the Cottrell analysis. Although it is inconclusive to verify the more dominant process using this method, we can still ensure that the ZnO-based supercapacitors with the addition of CDs are neither purely EDLC nor Faradaic process, but a combination of both, which is a unique characteristic of the composite electrodes combining electric double-layer and pseudocapacitve materials.

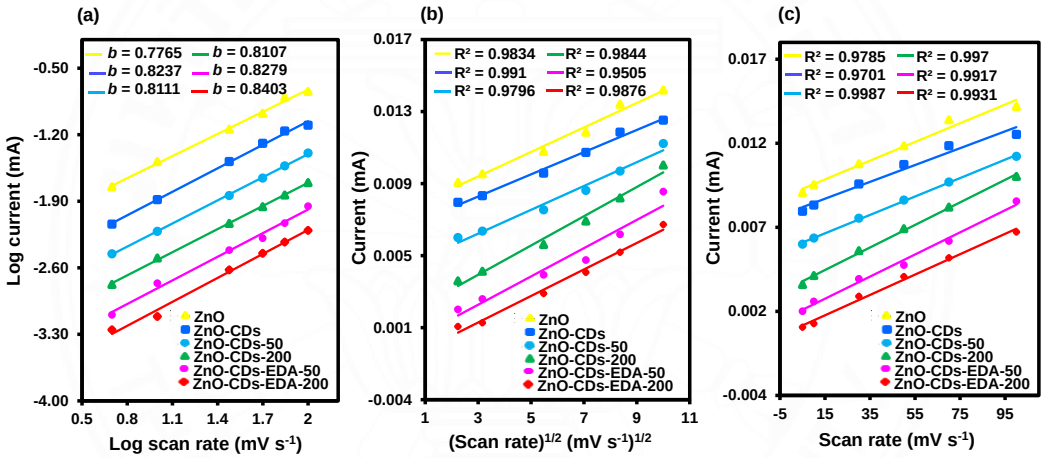

Figure 4.27 Plots of (a) log i vs log v, (b) i vs $v^{1/2}$, and (c) i vs v of ZnO, ZnO-CDs, ZnO-CDs-50, ZnO-CDs-200, ZnO-CDs-EDA-50, and ZnO-CDs-EDA-200 electrodes in 6 M KOH.

To further quantitatively determine the ratio of the capacitive contributions and the effects of CDs on the capacitive performance, the Dunn's method was implemented. The ratio between surface and diffusion contributions can be determined from the relationship between current at a fixed potential, i (V) and a square root of scan rate as shown in the following equations (Equations 14 and 15) [202, 203]:

$$i\,(\mathrm{V}) = k_1 v + k_2 v^{1/2} \qquad (14)$$

$$\frac{i\,(\mathrm{V})}{v^{1/2}} = k_1 v^{1/2} + k_2 \qquad (15)$$

where $k_1$and k_2 are the surface-controlled and diffusion-controlled coefficients, which are obtained from the slope and intercept from the plot of $\frac{i\,(\mathrm{V})}{v^{\frac{1}{2}}}$ vs. $v^{1/2}$. This analysis demonstrated that the surface-controlled capacitance played a larger role than the diffusion-controlled capacitance after the addition of CDs in the electrodes (Figure 4.28a), which was consistent with the results obtained from the Cottrell method. The use of CDs-EDA-200 in the electrode provided the highest surface-controlled coefficient value, which increased from 35.86% to 57.29%, compared to pristine ZnO. Moreover, Figure 4.28b shows that the higher specific capacitances can be observed at lower scan rates. This is attributed to excellent interactions between electrode and electrolyte at low scan rates. The CV curves in Figure 4.28c and d show the comparison between the surface-controlled and diffusion-controlled contribution areas of pristine ZnO and ZnO-CDs-EDA-200 electrodes. The ZnO electrode is diffusion-dominant whereas the ZnO-CDs-EDA-200 electrode is surface-dominant. This is indicative that the gamma-irradiated, amine-terminated CDs assisted some favorable surface effects to ion transport and charge storage that brought about better supercapacitor performance.

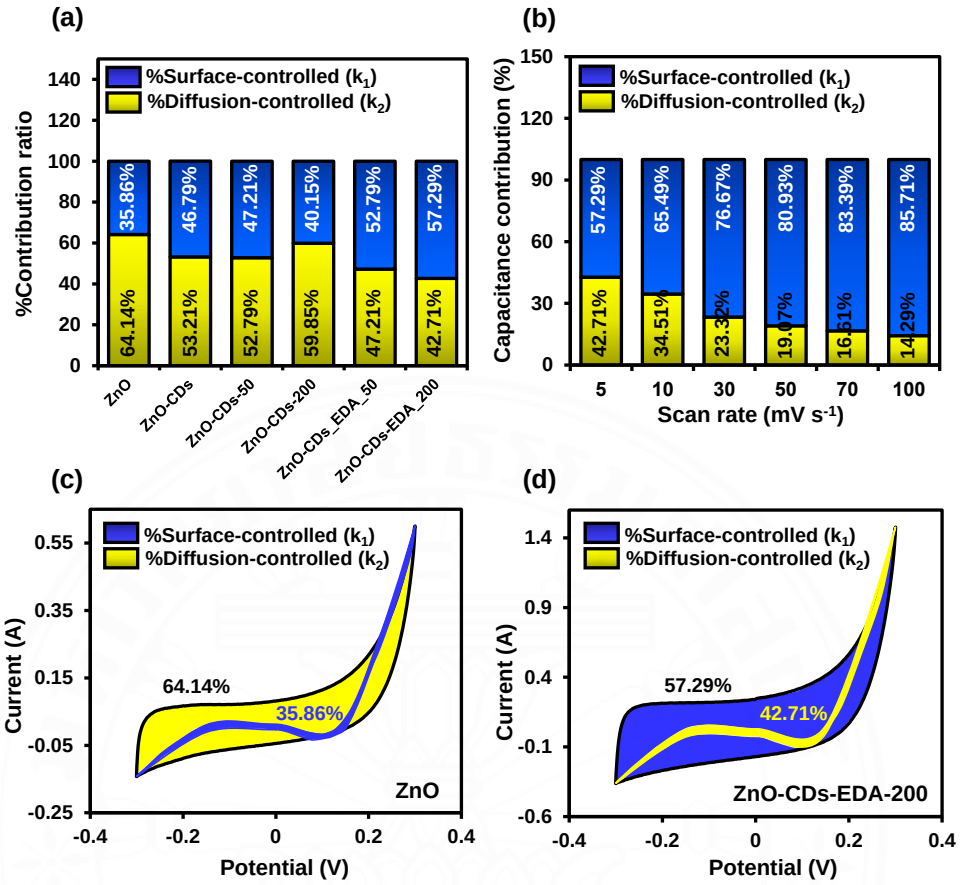

Figure 4.28 Plots of (a) percentage of contribution ratio vs. all samples at 5 mV s^{-1}, (b) percentage of capacitance contribution vs. scan rate, and percentage contribution of surface-controlled and diffusion-controlled processes in CV curves of (c) pristine ZnO and (d) ZnO-CDs-EDA-200 electrodes at 5 mV s^{-1}.

4.3.3.2 The electrochemical performance and the electrochemical surface area (ECSA)

To further investigate the electrochemical performance of the electrodes, the Warburg impedance equation was used as shown in Equation 16 [204].

$$Z_w = \sigma\omega^{-\frac{1}{2}}(1-j) \tag{16}$$

$$\sigma = \frac{RT}{n^2F^2A\sqrt{2}}\left(\frac{1}{\sqrt{D}C^*}\right) \tag{17}$$

where Z_w is the Warburg impedance, σ is the Warburg coefficient, ω is the angular frequency, j is the imaginary unit, and $C^*$is the concentration of electrolyte. It was found that the ZnO-CDs-EDA-200 electrode provided a higher Warburg coefficient of 3.22 Ω s^{-1}, compared to the ZnO electrode (2.98 Ω s^{-1}) (Figure 4.29c). According to Equation 17, the Warburg coefficient is inversely proportional to the diffusion coefficient. This demonstrated that the use of CDs-EDA-200 reduced the ion diffusion coefficient, which is attributed to the increasing of surface-reaction capacitive contribution in the ZnO-CDs-EDA-200 electrode.

Next, the electrochemical surface area (ECSA) of ZnO-CDs-EDA-200 and ZnO electrodes was evaluated [205]. Figure 4.29d depicts that the ZnO-CDs-EDA-200 electrode has a higher ECSA of 168.1 mF cm^{-2} than the ZnO electrode (154 mF cm^{-2}). This clearly confirmed that the use of CDs-EDA-200 increased the electrochemically active sites for charge storage, which led to the enhancement of the specific capacitance of the ZnO-CDs-EDA-200 electrode. From all these analyses, it is conclusive that the gamma-irradiated, amine-passivated CDs promoted surface/interface phenomena that are favorable to the ion transport and charge storage processes and possibly also the electrode mechanical integrity, leading to better specific capacitance and cycling stability.

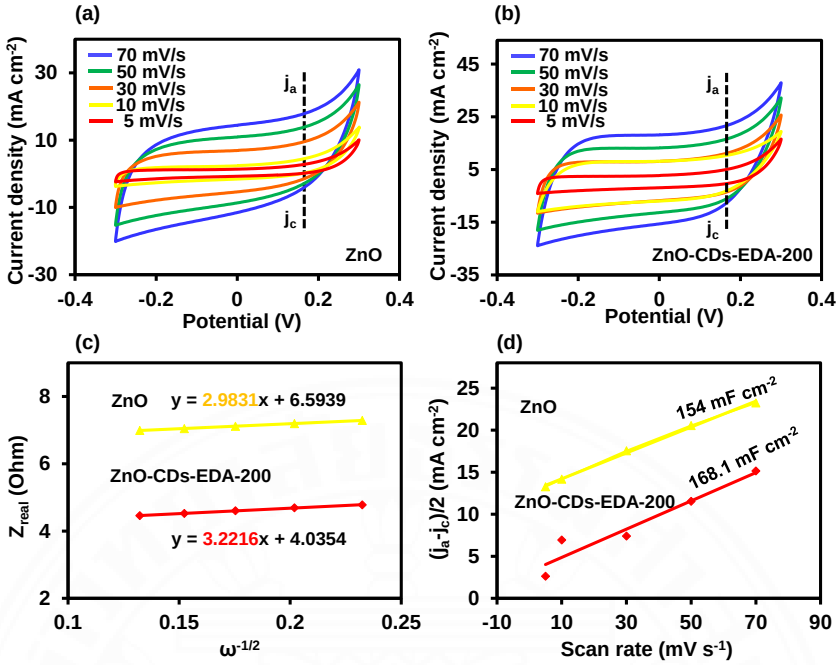

Figure 4.29 CV curves of (a) ZnO and (b) ZnO-CDs-EDA-200 electrodes, (c) and (d) electrochemical surface areas of ZnO and ZnO-CDs-EDA-200 electrodes.

4.3.4 Contact angle measurement

To study the hydrophilic/hydrophobic effects of the prepared electrodes, the contact angles of ZnO, ZnO-CDs, ZnO-CDs-50, ZnO-CDs-200, ZnO-CDs-EDA-50, and ZnO-CDs-EDA-200 electrodes were measured using the electrolyte solution as droplet (Figure 4.30). The ZnO-CDs-EDA-200 electrode showed the smallest contact angle of 29^o while the ZnO, ZnO-CDs, ZnO-CDs-50, ZnO-CDs-200, and ZnO-CDs-EDA-50 electrodes showed the contact angles of 115^o, 112^o, 108^o, 110^o, and 71^o, respectively. Thus, the ZnO-CDs-EDA-200 electrode is the most hydrophilic due to the highest number of ammonium groups on the passivated CDs surface. After 2 seconds, the electrolyte droplet was completely absorbed in the ZnO-CDs-EDA-200 electrode while those still remained on the ZnO, ZnO-CDs, ZnO-CDs-50, ZnO-CDs-200, ZnO-CDs-EDA-50, and ZnO-CDs-EDA-200 electrodes, showing the same trend of contact angles at 45^o, 26^o, 20^o, 24^o, and 11^o, respectively. These results demonstrated that CDs after modified with EDA and gamma irradiation at 200 kGy significantly

increased the hydrophilicity of CDs, improving the wettability of the electrode and electrode/electrolyte interactions. The contact angle measurement also directly supported the specific capacitance and electrochemical analyses above. Based on the results, we can conclude as follows: (1) the gamma-irradiated, amine-passivated CDs provided higher amount of pi electrons and aromaticity in the structure that raised the number of transferred electron and electron mobility for charge transport, (2) they facilitated the surface-controlled process for charge storage and improved the surface-controlled capacitance, and (3) the alteration of surface chemistry by gamma irradiation and amine passivation resulted in better surface wettability and mechanical adhesion of the electrode materials. All of these synergistically gave rise to the favorable interfaces between electrode and electrolyte, giving more electrochemically available sites to enhance the specific capacitance and cycling stability and reduce the resistance of the supercapacitors.

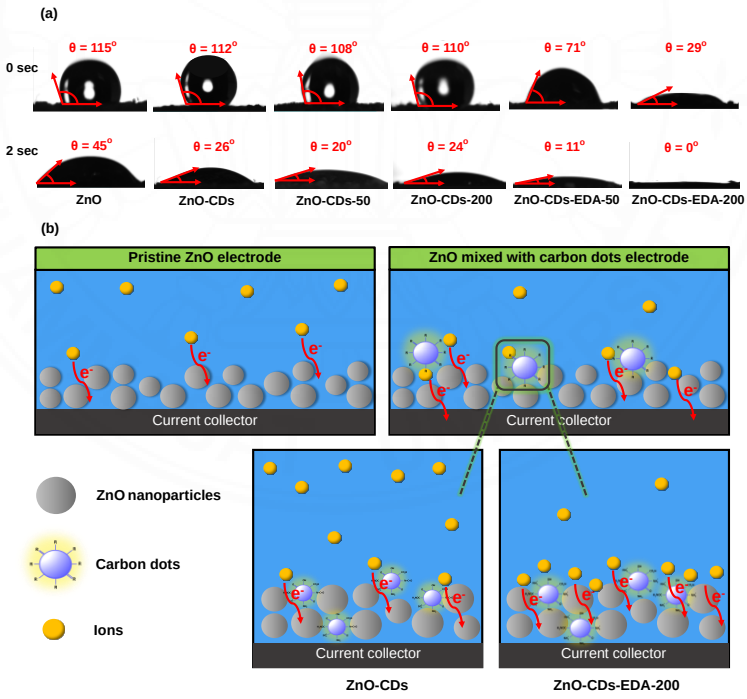

Figure 4.30 (a) Contact angles of ZnO, ZnO-CDs, ZnO-CDs-50, ZnO-CDs-200, ZnO-CDs-EDA-50, and ZnO-CDs-EDA-200 electrodes at 0 and 2 seconds and (b) schematic representation of ion/charge transfer process of the ZnO-CDs and ZnO-CDs-EDA-200 electrodes in 6 M KOH.

CHAPTER 5
CONCLUSIONS AND RECOMMENDATIONS

5.1 Conclusions

Carbon dots are a new class of carbon nanomaterials which are composed of sp^2 and sp^3 hybridizations as well as hydrophilic functional groups, such as hydroxyl, carbonyl, and carboxyl groups on their surface. They have been widely used in various applications, such as bio-imaging, drug delivery, and photocatalysis. Because the contamination of heavy metal ions in the environment is extremely harmful to the environment and human health and the depletion of fossil fuels and the occurrence of global warming have already caused the economic and environmental crisis, it is important to develop a simple, fast, sensitive, and low-cost methodology that could dissolve these problems. Therefore, in this thesis, we applied carbon dots in metal ion sensing and supercapacitor application.

Carbon dots in this thesis were synthesized from polymers, including polyurethane and natural rubber via one-step and two-step, respectively. Their recycling has been of great interest because polyurethane and natural rubber are ones of the most important polymers used in daily life. The carbon dot-derived from polyurethane were successfully prepared via pyrolysis with the addition of sulfuric acid. The resulting carbon dots exhibited green-blue emission under UV illumination with a 24% quantum yield. The carbon dots showed excellent selectivity towards Ni^{2+} ion with a detection limit of 3.14 µM and they also showed excellent recovery rates in a range of 95.64 to 99.22% when detecting in drinking water samples. Moreover, the carbon dots were loaded on filter papers as paper-based sensors for Ni^{2+} detection and shown a limit of detection of 43.3 µM. The results demonstrated that the fluorescence quenching was synergistically due to the formation of non-fluorescent complexes and inner filter effect between Ni^{2+} and carbon dots. The unique interaction between carbon dots and Ni^{2+} was also revealed by the XAS analysis. The carbon dots were proved to be also potent Ni^{2+} adsorbents. One carbon dot can hold up to 182 Ni^{2+} ions, equivalent to 234.8 $mg \cdot g^{-1}$. In addition, the obtained carbon dots were also applied in

supercapacitor application. The carbon dots were successfully modified by gamma irradiation and the addition of EDA. We demonstrated that not only the carbon dots but also a combination of gamma irradiation and amine passivation helped significantly improve the supercapacitor performance. Signifying the impact of irradiation dose, the CDs-EDA-200 gave the best specific capacitance and cycling stability by improving various key factors, including the surface-controlled capacitance, series resistance, ion diffusion coefficient, electrochemical active surface area, wettability, and mechanical adhesion of the electrode. Compared to the pure ZnO electrode, the ZnO-CDs-EDA-200 electrode boosted the specific capacitance by 312% and cycling stability from 87.41 to 99.87% after 8,500 cycles.

The carbon dot-derived from natural rubber was successfully prepared via two-step pyrolysis and hydrothermal method. The prepared carbon dots were formed in the spherical shape in the size range of 1-4 nm and gave blue emission under UV illumination, with a quantum yield of 0.6%. The carbon dots showed effective sensing potential toward Mg^{2+} ions with a detection limit of 4.3 µM. The carbon dots were also tested for their efficiency for Mg^{2+} detection in drinking water samples. The results showed the percentage recovery rates in a range between 97.21 to 99.21%, which is within the excellent range. Moreover, we fabricated paper-based sensors by loading carbon dots on the surface of filter papers and used them as fluorescent substrates for Mg^{2+} sensing, showing a limit of detection of 8.01 µM.

Overall, the synthesis of the carbon dots in this thesis is facile, efficient, low cost, and environmentally friendly, providing a methodology to increase the value of these resources. The obtained carbon dots are useful as effective sensors for metal ion detection and supercapacitor application.

5.2 Recommendations

5.2.1 Carbon dot-derived from polyurethane provided simple Ni^{2+} sensors with high sensitivity, selectivity, accuracy, practicality, and adsorption capacity. The carbon dots should be then applied as a portable tool with high reproducibility for Ni^{2+} detection in a real application.

5.2.2 The information to determine the type of interactions between carbon dot-derived from natural rubber and Mg^{2+} ions are not enough. Therefore, other specialized techniques should be used to characterize to provide more detailed information about the sensing mechanism.

5.2.3 The used polyurethane and natural rubber should be used to synthesize the carbon dots to transform waste materials into useful materials and increase the value of these resources.

REFERENCES

[1] Zhang, Y., H. Jiang, and X. Wang, *Cytidine-stabilized gold nanocluster as a fluorescence turn-on and turn-off probe for dual functional detection of Ag^{+} and Hg^{2+}*. Analytica Chimica Acta, 2015. **870**: p. 1-7.

[2] He, W., Luo, L., Liu, Q., and Chen, Z., *Colorimetric Sensor Array for Discrimination of Heavy Metal Ions in Aqueous Solution Based on Three Kinds of Thiols as Receptors.* Analytical Chemistry, 2018. **90**(7): p. 4770-4775.

[3] Azimi, A., Azari, A., Rezakazemi, M., and Ansarpour, M., *Removal of Heavy Metals from Industrial Wastewaters: A Review.* ChemBioEng Reviews, 2017. **4**(1): p. 37-59.

[4] Yan-Li, M., *Determination of Nickel in Water by Flame Atomic Absorption Spectrometry after Separation/Preconcentration with Exopolymers.* CHINESE JOURNAL OF ANALYTICAL CHEMISTRY, 2011. **39**: p. 1088-1092.

[5] Wang, J.L., *Determination of seven elements in artificial diamond by inductively coupled plasma atomic emission spectrometry.* Yejin Fenxi/Metallurgical Analysis, 2017. **37**: p. 49-53.

[6] Lei, L., Song, H., Zhao, J., Yang, Q., and Chen, Z., *Preparation of gold nanoparticles using pyridine-formaldehyde as a reducing agent and its application in high sensitivity colorimetric detection of Pb^{2+}*. Analytical Methods, 2019. **11**(34): p. 4362-4369.

[7] Zhang, T., Mu, L., She, G., and Shi, W., *2 × 2 Fluorescent sensor array based on SiNWs for analysis of Pb^{2+}, Cd^{2+}, Cr^{3+} and Hg^{2+}*. Journal of Luminescence, 2019. **209**: p. 267-273.

[8] Sang, F., X. Zhang, and F. Shen, *Fluorescent methionine-capped gold nanoclusters for ultra-sensitive determination of copper(II) and cobalt(II), and their use in a test strip.* Microchimica Acta, 2019. **186**(6): p. 373.

[9] Raza, W., Ali, F., Raza, N., Luo, Y., Kwon, E.E, Yang, J., Kumar, S., Mehmood, A., and Kim, K., *Recent advancements in supercapacitor technology*. Nano Energy, 2018. **52**: p. 441-473.

[10] Azizi, S., M. Seifi, and M.B. Askari, *NiFe anchored to reduced graphene oxide as a low-cost and high-performance electrode material for supercapacitor applications.* Physica B: Condensed Matter, 2021. **600**: p. 412606.

[11] Sathish Kumar, Prakash, P., Srinivasan, A., and Karuppiah, C., *A new highly powered supercapacitor electrode of advantageously united ferrous tungstate and functionalized multiwalled carbon nanotubes.* Journal of Power Sources, 2021. **482**: p. 228892.

[12] Ahadian, S. and M. Radisic, *12 - Nanotoxicity*, in *Nanobiomaterials Science, Development and Evaluation*, M. Razavi and A. Thakor, Editors. 2017, Woodhead Publishing. p. 233-248.

[13] Kusuma, J., S. Akash, and R. Geetha Balakrishna, *Transition metal nanohybrid as efficient and stable counter electrode for heterostructure quantum dot sensitized solar cells: A trial.* Solar Energy, 2020. **201**: p. 674-681.

[14] Bakirhan, N.K. and S.A. Ozkan, *Chapter 28 - Quantum Dots as a New Generation Nanomaterials and Their Electrochemical Applications in Pharmaceutical Industry*, in *Handbook of Nanomaterials for Industrial Applications*, C. Mustansar Hussain, Editor. 2018, Elsevier. p. 520-529.

[15] Reddy, S., He, L., Ramakrishana, S., and Luo, H., *Graphene nanomaterials for regulating stem cell fate in neurogenesis and their biocompatibility.* Current Opinion in Biomedical Engineering, 2019. **10**: p. 69-78.

[16] Guo, X. and N. Mei, *Assessment of the toxic potential of graphene family nanomaterials.* Journal of Food and Drug Analysis, 2014. **22**(1): p. 105-115.

[17] Nurulhuda, I., Mazatulikhma, M.Z., Alrokayan, Salman A.H., Khan, Haseeb A., and Rusop, M., *Toxicity Determinants of CNT-PEG/DOX Complex using Carbon Nanotubes Synthesis from Fermented Tapioca.* Materials Today: Proceedings, 2018. **5**: p. S191-S195.

[18] Ye, S., Wang, Y., Jiao, F., Zhang, H., Lin, C., Wu, Y., and Zhang, Q., *The role of NADPH oxidase in multi-walled carbon nanotubes-induced oxidative stress and cytotoxicity in human macrophages.* J Nanosci Nanotechnol, 2011. **11**(5): p. 3773-81.

[19] Xu, X., Ray, R., Gu, Y., Ploehn, Harry J., Gearheart, L., Raker, K., and Scrivens, Walter A., *Electrophoretic Analysis and Purification of Fluorescent Single-*

Walled Carbon Nanotube Fragments. Journal of the American Chemical Society, 2004. **126**(40): p. 12736-12737.

[20] Sagbas, S. and N. Sahiner, *Carbon dots: preparation, properties, and application*. 2019. p. 651-676.

[21] Yoo, D., Park, Y., Cheon, B., and Park, M., *Carbon Dots as an Effective Fluorescent Sensing Platform for Metal Ion Detection.* Nanoscale Research Letters, 2019. **14**(1): p. 272.

[22] de Oliveira, B.P. and F.O.M. da Silva Abreu, *Carbon quantum dots synthesis from waste and by-products: Perspectives and challenges.* Materials Letters, 2021. **282**: p. 128764.

[23] Shen, C.-L., Lou, Q., Liu, K.K., Dong, L., and Shan, C.-X, *Chemiluminescent carbon dots: Synthesis, properties, and applications.* Nano Today, 2020. **35**: p. 100954.

[24] Krishna, N.S., Pathak, A., Suneesh, P.V., and Babu, T.G.S., *Fluorescent detection of aspartate transaminase using N-doped carbon dots.* Materials Today: Proceedings, 2020.

[25] Chu, K.-W., Lee, S.L., Chan, C.-J., and Liu, L., *Recent Progress of Carbon Dot Precursors and Photocatalysis Applications*. Polymers. Vol. 11. 2019: MDPI. 689.

[26] Cong, S., Liu, K., Qiao, F., Song, Y., and Tan, M., *Biocompatible fluorescent carbon dots derived from roast duck for in vitro cellular and in vivo C. elegans bio-imaging*. Methods, 2019. **168**: p. 76-83.

[27] Shariati-Rad, M. and Z. Ghorbani, *Carbon dot-based colorimetric sensor array for the discrimination of different water samples.* Analytical Methods, 2019. **11**(43): p. 5584-5590.

[28] Das, P., Ganguly, S., Agarwal, T., Maity, P., Ghosh, S., Choudhary, S., Gangopadhyay, S., Maiti, T.K., Dhara, S., Banerjee, S., Das, N.C. (2019). Heteroatom doped blue luminescent carbon dots as a nano-probe for targeted cell labeling and anticancer drug delivery vehicle. Materials Chemistry and Physics, (), 121860–. doi:10.1016/j.matchemphys.2019.121860, *Heteroatom doped blue luminescent carbon dots as a nano-probe for targeted cell labeling*

and anticancer drug delivery vehicle. Materials Chemistry and Physics, 2019. **237**: p. 121860.

[29] Kakaei, K., Khodadoost, S., Gholipour, M., and Shouraei, N., *Core-shell polyaniline functionalized carbon quantum dots for supercapacitor.* Journal of Physics and Chemistry of Solids, 2021. **148**: p. 109753.

[30] Yang, Z.-C., Wang, M., Yong, A.M., Wong, S.Y., Zhang, X.-H., Tan, H., Chang, A.Y., Li, X., and Wang, J., *Intrinsically fluorescent carbon dots with tunable emission derived from hydrothermal treatment of glucose in the presence of monopotassium phosphate.* Chemical Communications, 2011. **47**(42): p. 11615-11617.

[31] Pan, D., Zhang, J., Li, Z., and Wu, M., *Hydrothermal Route for Cutting Graphene Sheets into Blue-Luminescent Graphene Quantum Dots.* Advanced Materials, 2010. **22**(6): p. 734-738.

[32] Sun, Y.-P., Zhou, B., Lin, Y., Wang, W., Fernando, K. A. S., Pathak, P., Meziani, M.J., Harruff, B.A., Wang, X., Wang, H, Luo, P.G., Yang, H., Kose, M.E., Chen, B., Veca, M., and Xie, S.-Y., *Quantum-Sized Carbon Dots for Bright and Colorful Photoluminescence.* Journal of the American Chemical Society, 2006. **128**(24): p. 7756-7757.

[33] Peng, J., Gao, W., Gupta, B.K., Liu, Z., Romero-Aburto, R., Ge, L., Song, L., Alemany, L.B., Zhan, X., Gao, G., Vithayathil, S.A., Kaipparettu, B.A., Marti, A.A., Hayashi, T., Zhu, J.-J., and Ajayan, P.M., *Graphene Quantum Dots Derived from Carbon Fibers.* Nano Letters, 2012. **12**(2): p. 844-849.

[34] Liu, H., T. Ye, and C. Mao, *Fluorescent Carbon Nanoparticles Derived from Candle Soot.* Angewandte Chemie International Edition, 2007. **46**(34): p. 6473-6475.

[35] Tao, H., Yang, K., Ma, Z., Wan, J., Zhang, Y., Kang, Z., and Liu, Z., *In Vivo NIR Fluorescence Imaging, Biodistribution, and Toxicology of Photoluminescent Carbon Dots Produced from Carbon Nanotubes and Graphite.* Small (Weinheim an der Bergstrasse, Germany), 2012. **8**.

[36] Sagbas, S. and N. Sahiner, *22 - Carbon dots: preparation, properties, and application*, in *Nanocarbon and its Composites*, A. Khan, et al., Editors. 2019, Woodhead Publishing. p. 651-676.

[37] Sharma, A. and J. Das, *Small molecules derived carbon dots: synthesis and applications in sensing, catalysis, imaging, and biomedicine.* Journal of nanobiotechnology, 2019. **17**(1): p. 92-92.

[38] Zuo, J., Jiang, T., Zhao, X., Xiong, X., Xiao, S., and Zhu, Z., *Preparation and Application of Fluorescent Carbon Dots.* Journal of Nanomaterials, 2015. **2015**: p. 787862.

[39] Anwar, S., Anwar, S., Ding, H., Xu, M., Hu, X., Li, Z., Wang, J., Liu, L., Jiang, L., Wang, D., Dong, C., Yan, M., Wang, Q., Bi, H., Recent Advances in Synthesis, Optical Properties and Biomedical Applications of Carbon Dots. ACS Applied Bio Materials, (), acsabm.9b00112–. doi:10.1021/acsabm.9b00112 , *Recent Advances in Synthesis, Optical Properties, and Biomedical Applications of Carbon Dots.* ACS Applied Bio Materials, 2019. **2**(6): p. 2317-2338.

[40] Chen, B.B., Liu, M.L., Li, C.M., and Huang, C.Z., *Fluorescent carbon dots functionalization.* Advances in Colloid and Interface Science, 2019. **270**: p. 165-190.

[41] Wen, Q.-L., Pu, Z.-F., Yang, Y.-J., Wang, J., Wu, B.-C., Hu, Y.-L., Liu, P., Ling, J., and Cao, Q., *Hyaluronic acid as a material for the synthesis of fluorescent carbon dots and its application for selective detection of Fe^{3+} ion and folic acid.* Microchemical Journal, 2020. **159**: p. 105364.

[42] Li, Y., Lee, J.-Y., Lee, H., Hu, C.-C., Chiu, T.-C., *Highly fluorescent nitrogen-doped carbon dots for selective and sensitive detection of Hg^{2+} and ClO^{-} ions and fluorescent ink.* Journal of Photochemistry and Photobiology A: Chemistry, 2021. **405**: p. 112931.

[43] Deng, Y., Zhao, D., Chen, X., Wang, F., Song, H., and Shen, D., *Long lifetime pure organic phosphorescence based on water soluble carbon dots.* Chemical Communications, 2013. **49**(51): p. 5751-5753.

[44] Baragau, I.-A., Lu, Z., Power, N.P., Morgan, D.J., Bowen, J., Diaz, P., Kellici, S., *Continuous hydrothermal flow synthesis of S-functionalised carbon quantum dots for enhanced oil recovery.* Chemical Engineering Journal, 2021. **405**: p. 126631.

[45] Chai, X., He, H., Fan, H., Kang, X., and Song, X., *A hydrothermal-carbonization process for simultaneously production of sugars, graphene quantum dots, and porous carbon from sugarcane bagasse.* Bioresource Technology, 2019. **282**: p. 142-147.

[46] Atchudan, R., Jebakumar Immanuel Edison, T.N., Shanmugam, M., Perumal, S., Somanathan, T., Lee, Y.R., *Sustainable synthesis of carbon quantum dots from banana peel waste using hydrothermal process for in vivo bioimaging.* Physica E: Low-dimensional Systems and Nanostructures, 2021. **126**: p. 114417.

[47] Singh, H., Bamrah, A., Khatri, M., and Bhardwaj, N., *One-pot hydrothermal synthesis and characterization of carbon quantum dots (CQDs).* Materials Today: Proceedings, 2020. **28**: p. 1891-1894.

[48] Khan, Z.M.S.H., Rahman, R.S., Shumaila, Islam, S., and Zulfequar, M., *Hydrothermal treatment of red lentils for the synthesis of fluorescent carbon quantum dots and its application for sensing* Fe^{3+}. Optical Materials, 2019. **91**: p. 386-395.

[49] Wu, F., Yang, M., Zhang, H., Zhu, S., Zhu, X., and Wang, K., *Facile synthesis of sulfur-doped carbon quantum dots from vitamin B1 for highly selective detection of* Fe^{3+} *ion.* Optical Materials, 2018. **77**: p. 258-263.

[50] Li, C., Zhang, X., Zhang, W., Qin, X., and Zhu, C., *Carbon quantum dots derived from pure solvent tetrahydrofuran as a fluorescent probe to detect pH and silver ion.* Journal of Photochemistry and Photobiology A: Chemistry, 2019. **382**: p. 111981.

[51] Jebakumar Immanuel Edison, T.N., Atchudan, R., Karthik, N., Xiong, D., and Lee, Y.R., *Facile hydrothermal synthesis of nitrogen rich blue fluorescent carbon dots for cell bio-imaging of Candida albicans.* Process Biochemistry, 2020. **88**: p. 113-119.

[52] Hu, C., Yu, C., Li, M., Wang, X., Yang, J., Zhao, Z., Eychmüller, A., Sun, Y.-P., and Qiu, J., *Chemically Tailoring Coal to Fluorescent Carbon Dots with Tuned Size and Their Capacity for Cu(II) Detection.* Small, 2014. **10**(23): p. 4926-4933.

[53] Zhu, H., Wang, X., Li, Y., Wang, Z., Yang, F., and Yang, X., *Microwave synthesis of fluorescent carbon nanoparticles with electrochemiluminescence properties.* Chemical Communications, 2009(34): p. 5118-5120.

[54] Wang, C., Wu, W., Periasamy, A.P., and Chang, H.-T., *Electrochemical synthesis of photoluminescent carbon nanodots from glycine for highly sensitive detection of hemoglobin.* Green Chemistry, 2014. **16**(5): p. 2509-2514.

[55] Sahu, S., Behera, B., Maiti, T.K., Mohapatra, S., *Simple one-step synthesis of highly luminescent carbon dots from orange juice: application as excellent bio-imaging agents.* Chemical Communications, 2012. **48**(70): p. 8835-8837.

[56] Wang, J., C.-F. Wang, and S. Chen, *Amphiphilic Egg-Derived Carbon Dots: Rapid Plasma Fabrication, Pyrolysis Process, and Multicolor Printing Patterns.* Angewandte Chemie International Edition, 2012. **51**(37): p. 9297-9301.

[57] Dong, Y., Shao, J., Chen, C., Li, H., Wang, R., Chi, Y., Lin, X., and Chen, G., *Blue luminescent graphene quantum dots and graphene oxide prepared by tuning the carbonization degree of citric acid.* Carbon, 2012. **50**(12): p. 4738-4743.

[58] Li, H., He, X., Liu, Y., Huang, H., Lian, S., Lee, S.-T., and Kang, Z., *One-step ultrasonic synthesis of water-soluble carbon nanoparticles with excellent photoluminescent properties.* Carbon, 2011. **49**(2): p. 605-609.

[59] Zheng, X.T., Ananthanarayanan, A., Luo, K.T., and Chen, P., *Glowing Graphene Quantum Dots and Carbon Dots: Properties, Syntheses, and Biological Applications.* Small, 2015. **11**(14): p. 1620-1636.

[60] Hsu, P.-C., Shih, Z.-Y., Lee, C.-H., and Chang, H.-T., *Synthesis and analytical applications of photoluminescent carbon nanodots.* Green Chemistry, 2012. **14**(4): p. 917-920.

[61] Dager, A., Uchida, T., Maekawa, T., and Tachibana, M., *Synthesis and characterization of Mono-disperse Carbon Quantum Dots from Fennel Seeds: Photoluminescence analysis using Machine Learning.* Scientific Reports, 2019. **9**(1): p. 14004.

[62] Yang, G., Wan, X., Su, Y.-K., Zeng, X., and Tang, J., *Acidophilic S-doped carbon quantum dots derived from cellulose fibers and their fluorescence*

sensing performance for metal ions in an extremely strong acid environment. Journal of Materials Chemistry A, 2016. **4**(33): p. 12841-12849.

[63] He, H.-T.; Xing, L.-C.; Zhang, J.-S.; Tang, M., *Binding characteristics of Cd^{2+}, Zn^{2+}, Cu^{2+}, and Li^{+} with humic substances: Implication to trace element enrichment in low-rank coals.* Energy Exploration & Exploitation, 2016. **34**(5): p. 735-745.

[64] Song, Z., Chen, X., Gong, X., Gao, X., Dai, Q., Nguyen, T.T., and Guo, M., Minghui, *Luminescent carbon quantum dots/nanofibrillated cellulose composite aerogel for monitoring adsorption of heavy metal ions in water.* Optical Materials, 2020. **100**: p. 109642.

[65] Chauhan, P., Dogra, S., Chaudhary, S., and Kumar, R., *Usage of coconut coir for sustainable production of high-valued carbon dots with discriminatory sensing aptitude toward metal ions.* Materials Today Chemistry, 2020. **16**: p. 100247.

[66] Singh, J., Kaur, S., Lee, J., Mehta, A., Kumar, S., Kim, K.-H., Basu, S., and Rawat, M., *Highly fluorescent carbon dots derived from Mangifera indica leaves for selective detection of metal ions.* Science of The Total Environment, 2020. **720**: p. 137604.

[67] Zhang, L., Wang, Y., Liu, W., Ni, Y., and Hou, Q., *Corncob residues as carbon quantum dots sources and their application in detection of metal ions.* Industrial Crops and Products, 2019. **133**: p. 18-25.

[68] Tiong, A.N.L., Wong, N.K.H., Fong, J.F.Y., Tan, X.W., and Ng, S.M., *A sustainable alternative to synthesis optical sensing receptor for the detection of metal ions.* Optical Materials, 2015. **40**: p. 132-138.

[69] Gupta, Disha Anilbhai; Desai, Mittal L.; Malek, Naved I.; Kailasa, and Suresh Kumar, *Fluorescence detection of Fe^{3+} ion using ultra-small fluorescent carbon dots derived from pineapple (Ananas comosus): Development of miniaturized analytical method.* Journal of Molecular Structure, 2020. **1216**: p. 128343.

[70] Pandey, S.C., Kumar, A., and Sahu, S.K., *Single Step Green Synthesis of Carbon Dots from Murraya koenigii leaves; A Unique Turn-off Fluorescent contrivance for Selective Sensing of Cd (II) ion.* Journal of Photochemistry and Photobiology A: Chemistry, 2020. **400**: p. 112620.

[71] Kailasa, S.K., Ha, S., Baek, S. H., Phan, L.M.T., Kim, S., Kwak, K., Park, and T. J., *Tuning of carbon dots emission color for sensing of Fe3+ ion and bioimaging applications.* Materials Science and Engineering: C, 2019. **98**: p. 834-842.

[72] Arumugam, N. and J. Kim, *Synthesis of carbon quantum dots from Broccoli and their ability to detect silver ions.* Materials Letters, 2018. **219**: p. 37-40.

[73] Gu, D., Hong, L., Zhang, L., Liu, H., and Shang, S., *Nitrogen and sulfur co-doped highly luminescent carbon dots for sensitive detection of Cd (II) ions and living cell imaging applications.* Journal of Photochemistry and Photobiology B: Biology, 2018. **186**: p. 144-151.

[74] Zhao, C., Li, X., Cheng, C., and Yang, Y., *Green and microwave-assisted synthesis of carbon dots and application for visual detection of cobalt(II) ions and pH sensing.* Microchemical Journal, 2019. **147**: p. 183-190.

[75] Sahoo, N.K., Das, S., Jana, G.C., Aktara, M.N., Patra, A., Maji, A., Beg, M., Jha, P.K., and Hossain, M., *Eco-friendly synthesis of a highly fluorescent carbon dots from spider silk and its application towards Hg (II) ions detection in real sample and living cells.* Microchemical Journal, 2019. **144**: p. 479-488.

[76] Zhao, X., Liao, S., Wang, L., Liu, Q., and Chen, X., *Facile green and one-pot synthesis of purple perilla derived carbon quantum dot as a fluorescent sensor for silver ion.* Talanta, 2019. **201**: p. 1-8.

[77] Sahu, V. and F. Khan, *Synthesis of bovine serum albumin capped boron-doped carbon dots for sensitive and selective detection of Pb(II) ion.* Heliyon, 2020. **6**(5): p. e03957.

[78] Abdolmohammad-Zadeh, H., Z. Azari, and E. Pourbasheer, *Fluorescence resonance energy transfer between carbon quantum dots and silver nanoparticles: Application to mercuric ion sensing.* Spectrochimica Acta Part A: Molecular and Biomolecular Spectroscopy, 2021. **245**: p. 118924.

[79] Jing, N., Tian, M., Wang, Y., and Zhang, Y., *Nitrogen-doped carbon dots synthesized from acrylic acid and ethylenediamine for simple and selective determination of cobalt ions in aqueous media.* Journal of Luminescence, 2019. **206**: p. 169-175.

[80] Sarkar, C., Chowdhuri, A.R., Kumar, A., Laha, D., Garai, S., Chakraborty, J., and Sahu, S.K., *One pot synthesis of carbon dots decorated carboxymethyl cellulose- hydroxyapatite nanocomposite for drug delivery, tissue engineering and Fe^{3+} ion sensing.* Carbohydrate Polymers, 2018. **181**: p. 710-718.

[81] Devi, N. and S.S. Ray, *Performance of bismuth-based materials for supercapacitor applications: A review.* Materials Today Communications, 2020. **25**: p. 101691.

[82] Murray, D. and J. Hayes, *Cycle Testing of Supercapacitors for Long-Life Robust Applications.* Power Electronics, IEEE Transactions on, 2015. **30**: p. 2505-2516.

[83] Chen, Y., Zhang, X., Xu, C., and Xu, H., *The fabrication of asymmetry supercapacitor based on MWCNTs/MnO_2/PPy composites.* Electrochimica Acta, 2019. **309**: p. 424-431.

[84] Yeo, T., Shin, D., Shin, J., Hwang, H., Seo, B., Lee, J., and Choi, W., *DC-field-driven combustion waves for one-step fabrication of reduced manganese oxide/multi-walled carbon nanotube hybrid nanostructures as high-performance supercapacitor electrodes.* Journal of Materials Chemistry, 2017. **5**: p. 24707-24719.

[85] Jayachandran, M., Kishore Babu, S., Maiyalagan, T., Rajadurai, N., and Vijayakumar, T., *Activated carbon derived from bamboo-leaf with effect of various aqueous electrolytes as electrode material for supercapacitor applications.* Materials Letters, 2021. **301**: p. 130335.

[86] Majumdar, D., N. Baugh, and S.K. Bhattacharya, *Ultrasound assisted formation of reduced graphene oxide-copper (II) oxide nanocomposite for energy storage applications.* Colloids and Surfaces A: Physicochemical and Engineering Aspects, 2017. **512**: p. 158-170.

[87] Pröbstle, H., C. Schmitt, and J. Fricke, *Button cell supercapacitors with monolithic carbon aerogels.* Journal of Power Sources, 2002. **105**(2): p. 189-194.

[88] Augustyn, V., P. Simon, and B. Dunn, *Pseudocapacitive oxide materials for high-rate electrochemical energy storage.* Energy & Environmental Science, 2014. **7**(5): p. 1597-1614.

[89] Faraji, S. and F. Ani, *Microwave-assisted synthesis of metal oxide/hydroxide composite electrodes for high power supercapacitors – A review.* Journal of Power Sources, 2014. **263**: p. 338–360.

[90] Lv, H., Gao, X., Xu, Q., Liu, H., Wang, Y.-G., and Xia, Y., *Carbon Quantum Dot-Induced MnO_2 Nanowire Formation and Construction of a Binder-Free Flexible Membrane with Excellent Superhydrophilicity and Enhanced Supercapacitor Performance.* ACS Applied Materials & Interfaces, 2017. **9**(46): p. 40394-40403.

[91] Zhang, X., Wang, J., Liu, J., Wu, J., Chen, H., and Bi, H., *Design and preparation of a ternary composite of graphene oxide/carbon dots/polypyrrole for supercapacitor application: Importance and unique role of carbon dots.* Carbon, 2017. **115**: p. 134-146.

[92] Zhao, T., Peng, X., Zhao, X., Hu, J., Jiang, T., Lu, X., Zhang, H., Li, T., and Ahmad, I., *Preparation and performance of carbon dot decorated copper sulphide/carbon nanotubes hybrid composite as supercapacitor electrode materials.* Journal of Alloys and Compounds, 2020. **817**: p. 153057.

[93] M. Ramani, Bala S. Haran, Ralph E. White, Branko N. Popov, and Ljubomir Arsov, *Studies on activated carbon capacitor materials loaded with different amounts of ruthenium oxide.* Journal of Power Sources, 2001. **93**: p. 209-214.

[94] Sarkodie, B., Hu, Y., Bi, W., Jiang, J., and Li, C., *Promotional effects of CuxO on the activity of Cu/ZnO catalyst toward efficient CO oxidation.* Applied Surface Science, 2021. **548**: p. 149241.

[95] Li, A.-K., Wu, W.-T., Kao, C.-C., and Chang, R.P.H., *Synthesis of Monodispersed ZnO Nanoparticles and their Luminescent Properties.* Key Engineering Materials, 2003. **247**: p. 405-410.

[96] Khan, S. A., Zain, Z. M., Mansoor, M., Mahfuz, M. M. H., Rahman, A., Rashid, M. A. N., and Rais, M. S., *Performance investigation of ZnO/PVA nanocomposite film for organic solar cell.* Materials Today: Proceedings, 2021.

[97] Wei, J.-S., Zhu, Z.-Y., Zhao, X., Song, T.-B., Huang, J.-H., Zhang, Y.-X., Liu, X., Chen, L., Niu, X.-Q., Wang, Y.-G., and Xiong, H.-M., *Self-assembled ZnO-carbon dots anode materials for high performance nickel-zinc alkaline batteries.* Chemical Engineering Journal, 2021. **425**: p. 130660.

[98] Kavitha, T. and S. Kumar, *Multifunctionalities enabled by the synergistic effects of mesoporous carbon dots and ZnO nanorods.* Materials Research Express, 2021.

[99] Ahmed, F., Almutairi, G., AlOtaibi, B., Kumar, S., Arshi, N., Hussain, S. G., Umar, A., Ahmad, N., and Aljaafari, A., *Binder-Free Electrode Based on ZnO Nanorods Directly Grown on Aluminum Substrate for High Performance Supercapacitors.* Nanomaterials, 2020. **10**(10).

[100] Tsai, J.-H., Tsai, M.-C., Sung, C.-Y., and Huang, P.-T., *Significant increase in current density of inverted polymer solar cells by induced-crystallization of sol-gel ZnO embedded with ZnO-NP*. Organic Electronics, 2020. **86**: p. 105891.

[101] Zhang, H., Yang, D., Ji, Y., Ma, X., Xu, J., and Que, D., *Low Temperature Synthesis of Flowerlike ZnO Nanostructures by Cetyltrimethylammonium Bromide-Assisted Hydrothermal Process.* The Journal of Physical Chemistry B, 2004. **108**(13): p. 3955-3958.

[102] Hu, X., Y.-J. Zhu, and S.-W. Wang, *Sonochemical and Microwave-Assisted Synthesis of Linked Single-Crystalline ZnO Rods.* Materials Chemistry and Physics, 2004. **88**: p. 421-426.

[103] Shaheen, I., Ahmad, K.S., Zequine, C., Gupta, R.K., Thomas, A.G., and Azad Malik, M., *Sustainable synthesis of organic framework-derived ZnO nanoparticles for fabrication of supercapacitor electrode.* Environmental Technology, 2022. **43**(4): p. 605-616.

[104] He, X., Yoo, J., Lee, M., and Bae, J., *Morphology engineering of ZnO nanostructures for high performance supercapacitors: Enhanced electrochemistry of ZnO nanocones compared to ZnO nanowires.* Nanotechnology, 2017. **28**.

[105] Oliveira, A.P.A., Hochepied, J.-F., Grillon, F., and Berger, M.H., *Controlled Precipitation of Zinc Oxide Particles at Room Temperature.* Chemistry of Materials, 2003. **15**(16): p. 3202-3207.

[106] Wang, J., Chen, R., Xiang, L., and Komarneni, S., *Synthesis, properties and applications of ZnO nanomaterials with oxygen vacancies: A review.* Ceramics International, 2018. **44**.

[107] Cai, D., Huang, H., Wang, D., Liu, B., Wang, L., Liu, Y., Li, Q., and Wang, T., *High-Performance Supercapacitor Electrode Based on the Unique ZnO@Co_3O_4 Core/Shell Heterostructures on Nickel Foam.* ACS Applied Materials & Interfaces, 2014. **6**(18): p. 15905-15912.

[108] Budimir, M., Marković, Z., Jovanović, D., Vujisić, M., Mičušík, M., Danko, M., Kleinová, A., Švajdlenková, H., Špitalský, Z., and Marković, B.T., *Gamma ray assisted modification of carbon quantum dot/polyurethane nanocomposites: structural, mechanical and photocatalytic study.* RSC Advances, 2019. **9**(11): p. 6278-6286.

[109] Montanari, L., Costantini, M., Signoretti, E.C., Valvo, L., Santucci, M., Bartolomei, M., Fattibene, P., Onori, S., Faucitano, A., Conti, B., and Genta, I., *Gamma irradiation effects on poly(dl-lactictide-co-glycolide) microspheres.* Journal of Controlled Release, 1998. **56**(1): p. 219-229.

[110] Jovanovic, S., Syrgiannis, Z., Markovic, Z., Bonasera, A., Kepic, D., Budimir, M., Milivojevic, D., Spasojevic, V., Dramicanin, M., Pavlović, V., and Todorovic Markovic, B., *Modification of Structural and Luminescence Properties of Graphene Quantum Dots by Gamma Irradiation and Their Application in a Photodynamic Therapy.* ACS Applied Materials & Interfaces, 2015. **7**(46): p. 25865-25874.

[111] Dumée, L.F., Feng, C., He, L., Yi, Z., She, F., Peng, Z., Gao, W., Banos, C., Davies, J.B., Huynh, C., Hawkins, S., Duke, and Mikel C.; Gray, Stephen; Hodgson, Peter D.; Kong, Lingxue, *Single step preparation of meso-porous and reduced graphene oxide by gamma-ray irradiation in gaseous phase.* Carbon, 2014. **70**: p. 313-318.

[112] Jovanovic, S., Dorontic, S., Jovanovic, D., Ciasca, G., Budimir, M., Bonasera, A., Scopelliti, M., Markovic, O., and Todorovic Markovic, B., *Gamma irradiation of graphene quantum dots with ethylenediamine: Antioxidant for ion sensing.* Ceramics International, 2020. **46**(15): p. 23611-23622.

[113] Hola, K., Bourlinos, A.B., Kozak, O., Berka, K., Siskova, K.M., Havrdova, M., Tucek, J., Safarova, K., Otyepka, M., Giannelis, E.P., and Zboril, R., *Photoluminescence effects of graphitic core size and surface functional groups*

in carbon dots: COO^- induced red-shift emission. Carbon, 2014. **70**: p. 279-286.

[114] Štengl, V., Bakardjieva, S., Henych, J., Lang, K., and Kormunda, M., *Blue and green luminescence of reduced graphene oxide quantum dots.* Carbon, 2013. **63**: p. 537-546.

[115] Lu, K., Li, C., Wang, H., Li, Y., Zhu, ., and Ouyang, Y., *Effect of gamma irradiation on carbon dot decorated polyethylene-gold@ hydroxyapatite biocomposite on titanium implanted repair for shoulder joint arthroplasty.* Journal of Photochemistry and Photobiology B: Biology, 2019. **197**.

[116] Budimir, M., Marković, Z., Vajdak, J., Jovanović, S., Kubat, P., Matej Mičušik, P.H, Danko, M., Barras, A., Milivojević, D., Špitalsky, Z., Boukherroub, R., and Todorović Marković, B., *Enhanced visible light-triggered antibacterial activity of carbon quantum dots/polyurethane nanocomposites by gamma rays induced pre-treatment.* Radiation Physics and Chemistry, 2021. **185**: p. 109499.

[117] Manvi, P.K., Beckers, M., and Mohr, B., *Chapter 3 - Polymer fiber-based biocomposites for medical sensing applications*, in *Materials for Biomedical Engineering*, V. Grumezescu and A.M. Grumezescu, Editors. 2019, Elsevier. p. 57-88.

[118] Chattopadhyay, D.K. and K.V.S.N. Raju, *Structural engineering of polyurethane coatings for high performance applications.* Progress in Polymer Science, 2007. **32**(3): p. 352-418.

[119] Madbouly, S.A. and J.U. Otaigbe, *Recent advances in synthesis, characterization and rheological properties of polyurethanes and POSS/polyurethane nanocomposites dispersions and films.* Progress in Polymer Science, 2009. **34**(12): p. 1283-1332.

[120] Howard, G.T., *Biodegradation of polyurethane: a review.* International Biodeterioration & Biodegradation, 2002. **49**(4): p. 245-252.

[121] Calvo-Correas, T., Ugarte, L., Trzebiatowska, P.J., Sanzberro, R., Datta, J., Corcuera, M.A., and Eceiza, A., *Thermoplastic polyurethanes with glycolysate intermediates from polyurethane waste recycling.* Polymer Degradation and Stability, 2017. **144**: p. 411-419.

[122] Manioudakis, J., Victoria, F., Thompson, C.A., Brown, L., Movsum, M., Lucifero, R., and Naccache, R., *Effects of nitrogen-doping on the photophysical properties of carbon dots.* Journal of Materials Chemistry C, 2019. **7**(4): p. 853-862.

[123] Xu, E., Campanella, O.H., Ye, X., Jin, Z., Liu, D., and BeMiller, J.N., *Advances in conversion of natural biopolymers: A reactive extrusion (REX)–enzyme-combined strategy for starch/protein-based food processing.* Trends in Food Science & Technology, 2020. **99**: p. 167-180.

[124] Ginting, E.M., Bukit, N., Frida, E., and Bukit, B.F., *Microstructure and thermal properties of natural rubber compound with palm oil boilers ash for nanoparticle filler.* Case Studies in Thermal Engineering, 2020. **17**: p. 100575.

[125] Puskas, J. and B. Barkakaty, *Natural rubber (NR) biosynthesis: Perspectives from polymer chemistry.* Chemistry, Manufacture and Applications of Natural Rubber, 2014: p. 30-67.

[126] Subramaniam, A., *The chemistry of natural rubber latex.* Immunology and Allergy Clinics of North America, 1995. **15**(1): p. 1-20.

[127] Hu, Y. and Z. Gao, *Sewage sludge in microwave oven: a sustainable synthetic approach toward carbon dots for fluorescent sensing of para-Nitrophenol.* J. Hazard. Mater., 2020. **382**: p. 121048.

[128] Hu, Y., Gao, Z., Yang, J., Chen, and H.,Han, L., *Environmentally benign conversion of waste polyethylene terephthalate to fluorescent carbon dots for "on-off-on" sensing of ferric and pyrophosphate ions.* J. Colloid Interface Sci., 2019. **538**: p. 481-488.

[129] Wang, T., Wang, A., Wang, R., Liu, Z., Sun, Y., Shan, G., Chen, Y., and Liu, Y., *Carbon dots with molecular fluorescence and their application as a "turn-off" fluorescent probe for ferricyanide detection.* Sci. Rep., 2019. **9**(1): p. 10723.

[130] Permatasari, F.A., Fukazawa, H., Ogi, T., Iskandar, F., and Okuyama, K., *Design of pyrrolic-N-rich carbon dots with absorption in the first near-infrared window for photothermal therapy.* ACS Appl. Nano Mater., 2018. **1**(5): p. 2368-2375.

[131] Zulfajri, M., Gedda, G., Chang, C.-J., Chang, Y.-P., and Huang, G.G., *Cranberry beans derived carbon dots as a potential fluorescence sensor for selective detection of Fe(III) ions in aqueous solution.* ACS omega, 2019. **4**(13): p. 15382-15392.

[132] Dela Cruz, M.I.S., Thongsai, N., de Luna, M.D.G., In, I., and Paoprasert, P., *Preparation of highly photoluminescent carbon dots from polyurethane: Optimization using response surface methodology and selective detection of silver (I) ion.* Colloids Surf. A Physicochem. Eng. Asp., 2019. **568**: p. 184-194.

[133] Liu, H., Zhang, Y., Liu, J.H., Hou, P., Zhou, J., and Huang, C.Z., *Preparation of nitrogen-doped carbon dots with high quantum yield from Bombyx mori silk for Fe(III) ions detection.* RSC Adv., 2017. **7**(80): p. 50584-50590.

[134] Xu, Q., Pu, P., Zhao, J., Dong, C., Gao, C., Chen, Y., Chen, J., Liu, Y., and Zhou, H., *Preparation of highly photoluminescent sulfur-doped carbon dots for Fe(III) detection.* J. Mater. Chem. A, 2015. **3**(2): p. 542-546.

[135] Yang, H., He, L., Long, Y., Li, H., Pan, S., Liu, H., and Hu, X., *Fluorescent carbon dots synthesized by microwave-assisted pyrolysis for chromium(VI) and ascorbic acid sensing and logic gate operation.* Spectrochim. Acta A Mol. Biomol. Spectrosc. , 2018. **205**: p. 12-20.

[136] Dong, Y., Pang, H., Yang, H., Guo, C., Shao, J., Chi, Y., Li, C.M., and Yu, Ting, *Carbon-based dots Co-doped with nitrogen and sulfur for high quantum yield and excitation-independent emission.* Angew. Chem. Int. Ed., 2013. **52**(30): p. 7800-7804.

[137] Gao, F., Ma, S., Li, J., Dai, K., Xiao, X., Zhao, D., and Gong, W., *Rational design of high quality citric acid-derived carbon dots by selecting efficient chemical structure motifs.* Carbon, 2017. **112**: p. 131-141.

[138] Das, P., Maity, P.P., Ganguly, S., Ghosh, S., Baral, J., Bose, M., Choudhary, S., Gangopadhyay, S., Dhara, S., Das, A., Banerjee, S., and Das, N.C., *Biocompatible carbon dots derived from κ-carrageenan and phenyl boronic acid for dual modality sensing platform of sugar and its anti-diabetic drug release behavior.* Int. J. Biol. Macromol., 2019. **132**: p. 316-329.

[139] Huang, K., He, Q., Sun, R., Fang, L., Song, H., Li, L., Li, Z., Tian, Y., Cui, H., and Zhang, J., *Preparation and application of carbon dots derived from cherry blossom flowers.* Chem. Phys. Lett., 2019. **731**: p. 136586.

[140] Prathumsuwan, T., Jaiyong, P., In, I., Paoprasert, P., *Label-free carbon dots from water hyacinth leaves as a highly fluorescent probe for selective and sensitive detection of borax.* Sens. Actuators B Chem. , 2019. **299**: p. 126936.

[141] Chu, K.-W., Lee, S.L., Chang, C.-J., and Liu, L., *Recent Progress of Carbon Dot Precursors and Photocatalysis Applications.* Polymers, 2019. **11**(4): p. 689.

[142] Zhao, Y., S. Zuo, and M. Miao, *The effect of oxygen on the microwave-assisted synthesis of carbon quantum dots from polyethylene glycol.* RSC Advances, 2017. **7**(27): p. 16637-16643.

[143] Huang, J., Yin, X.-Y., Yang, J.-Y., and Guo, M.-L., *Solid protonic acids and luminescent carbon dots derived from waste expanded polystyrene.* Materials Letters, 2014. **117**: p. 112-115.

[144] Ren, X., Liu, J., Meng, X., Wei, J., Liu, T., and Tang, F., *Synthesis of Ultra-Stable Fluorescent Carbon Dots from Polyvinylpyrrolidone and Their Application in the Detection of Hydroxyl Radicals.* Chemistry, an Asian journal, 2014. **9**.

[145] Tao, S., Song, Y., Zhu, S., Shao, J., and Yang, B., *A new type of polymer carbon dots with high quantum yield: From synthesis to investigation on fluorescence mechanism.* Polymer, 2017. **116**: p. 472-478.

[146] Gong, Y. and H. Liang, *Nickel ion detection by imidazole modified carbon dots.* Spectrochimica acta. Part A, Molecular and biomolecular spectroscopy, 2019. **211**: p. 342-347.

[147] Alizadeh, K. and N. Rad, *A new optical sensor for selective monitoring of nickel ion based on a hydrazone derivative immobilized on the triacetyl cellulose membrane.* J. Anal. Bioanal. Tech., 2016. **7**.

[148] Sahani, M.K., Singhal, D., Singh, A.K., Jain, A.K., Singh, U.P., and Narang, S., *Potentiometric sensor for the nanoscale monitoring of Ni^{2+} ion in environmental samples by the fabrication of coated pyrolytic graphite electrode based on a novel C–C-coupled compound.* Int. J. Environ. Anal. Chem. , 2016. **96**(12): p. 1170-1187.

[149] Hamidi, N., T. Alizadeh, and M. Madani, *A novel potentiometric Ni^{2+}-sensor based on a Ni^{2+} ion-imprinted polymer.* Anal. Bioanal. Electrochem., 2018. **10**(2): p. 281-291.

[150] Almaquer, F.E.P., J.S.Y. Ricacho, and R.L.G. Ronquillo, *Simple and rapid colorimetric sensing of Ni(II) ions in tap water based on aggregation of citrate-stabilized silver nanoparticles.* Sustain. Environ. Res., 2019. **29**(1): p. 23.

[151] Feng, J., Jin, W., Huang, P., and Wu, F., *Highly selective colorimetric detection of Ni^{2+} using silver nanoparticles cofunctionalized with adenosine monophosphate and sodium dodecyl sulfonate.* J. Nanopart. Res., 2017. **19**(9): p. 306.

[152] Li, H., Z. Cui, and C. Han, *Glutathione-stabilized silver nanoparticles as colorimetric sensor for Ni^{2+} ion.* Sens. Actuators B Chem., 2009. **143**(1): p. 87-92.

[153] Alizadeh, K. and N. Rad, *A New Optical Sensor for Selective Monitoring of Nickel Ion Based on A Hydrazone Derivative Immobilized on the Triacetyl Cellulose Membrane.* Journal of Analytical & Bioanalytical Techniques, 2016. **7**.

[154] Sahani, M.K., Singhal, D., Singh, A.K., Jain, A.K., Singh, U.P., and Narang, S., *Potentiometric sensor for the nanoscale monitoring of Ni^{2+} ion in environmental samples by the fabrication of coated pyrolytic graphite electrode based on a novel C–C-coupled compound.* International Journal of Environmental Analytical Chemistry, 2016. **96**(12): p. 1170-1187.

[155] Feng, J., Jin, W., Huang, P., and Wu, F., *Highly selective colorimetric detection of Ni^{2+} using silver nanoparticles cofunctionalized with adenosine monophosphate and sodium dodecyl sulfonate.* Journal of Nanoparticle Research, 2017. **19**(9): p. 306.

[156] Hamidi, N., T. Alizadeh, and M. Madani, *A Novel Potentiometric Ni2+-Sensor based on a Ni^{2+} Ion-Imprinted Polymer.* ANALYTICAL & BIOANALYTICAL ELECTROCHEMISTRY, 2018. **10**(2): p. 281-291.

[157] Li, H., Z. Cui, and C. Han, *Glutathione-stabilized silver nanoparticles as colorimetric sensor for Ni^{2+} ion.* Sensors and Actuators B: Chemical, 2009. **143**(1): p. 87-92.

[158] Almaquer, F.E.P., J.S.Y. Ricacho, and R.L.G. Ronquillo, *Simple and rapid colorimetric sensing of Ni(II) ions in tap water based on aggregation of citrate-stabilized silver nanoparticles.* Sustainable Environment Research, 2019. **29**(1): p. 23.

[159] Gong, Y. and H. Liang, *Nickel ion detection by imidazole modified carbon dots.* Spectrochimica Acta Part A: Molecular and Biomolecular Spectroscopy, 2019. **211**: p. 342-347.

[160] Zu, F., Yan, F., Bai, Z., Xu, J., Wang, Y., Huang, Y., and Zhou, X., *The quenching of the fluorescence of carbon dots: A review on mechanisms and applications.* Microchim. Acta, 2017. **184**: p. 1-16.

[161] Thongsai, N., Nagae, Y., Hirai, T., Takahara, A., Uchiyama, T., Kamitani, K., and Paoprasert, P., *Multifunctional nitrogen-doped carbon dots from maleic anhydride and tetraethylenepentamine via pyrolysis for sensing, adsorbance, and imaging applications.* Sens. Actuators B Chem., 2017. **253**: p. 1026-1033.

[162] Aziz, S.B., Abdullah, O., Brza, M.A.; Azawy, A.K., and Tahir, D.A., *Effect of carbon nano-dots (CNDs) on structural and optical properties of PMMA polymer composite.* Results Phys., 2019. **15**: p. 102776.

[163] Adsetts, J.R., Zhang, R., Yang, L., Chu, K., Wong, J., Love, D.A., and Ding, Z., *Efficient white electrochemiluminescent emission from carbon quantum dot films.* Front. Chem. , 2020. **8**(865).

[164] Varunkumar, K., Hussain, R., Hegde, G., and Ethiraj, A.S., *Effect of calcination temperature on Cu doped NiO nanoparticles prepared via wet-chemical method: structural, optical and morphological studies.* Mater. Sci. Semicond. Process., 2017. **66**: p. 149-156.

[165] Onundi, Y.B., Mamun, A.A., Khatib, M.F.Al, and Ahmed, Y. M., *Adsorption of copper, nickel and lead Ions from synthetic semiconductor industrial wastewater by palm shell activated carbon.* Int. J. Environ. Sci. Technol., 2010. **7**: p. 751-758.

[166] Çelebi, H., G. Gök, and O. Gök, *Adsorption capability of brewed tea waste in waters containing toxic lead(II), cadmium (II), nickel (II), and zinc(II) heavy metal ions.* Sci. Rep., 2020. **10**(1): p. 17570.

[167] Shrestha, R.M., Varga, M., Varga, I., Yadav, A.P., Pokharel, B.P., and Pradhananga, R.R. *Removal of Ni (II) from aqueous solution by adsorption onto activated carbon prepared from Lapsi (Choerospondias axillaris) seed stone*. in *Journal of the Institute of Engineering*. 2014.

[168] Zhang, X. and X. Wang, *Adsorption and desorption of nickel(II) ions from aqueous solution by a lignocellulose/montmorillonite nanocomposite.* PLoS One, 2015. **10**(2): p. e0117077-e0117077.

[169] Pivarčiová, L., Rosskopfova, O., Galambos, M., and Rajec, P., *Sorption of nickel on chitosan.* J. Radioanal. Nucl. Chem. , 2014. **300**(1): p. 361-366.

[170] Rehr, J.J. and R.C. Albers, *Theoretical approaches to x-ray absorption fine structure.* Reviews of Modern Physics, 2000. **72**(3): p. 621-654.

[171] Bunker, G., *Introduction to XAFS: a practical guide to X-ray absorption fine structure spectroscopy*. 2010: Cambridge University Press.

[172] Rane, S.S., Ajameri, A., Mody, R., and Padmaja, P., *Development and validation of RP-HPLC and RP-UPLC methods for quantification of parathyroid hormones (1-34) in medicinal product formulated with meta-cresol.* J. Pharm. Anal., 2012. **2**(2): p. 136-142.

[173] Herculano, R.D., Queiroz, A.A.A., Kinoshita, A., Oliveira Jr, O.N., and Graeff, C.F.O., *On the release of metronidazole from natural rubber latex membranes.* Mater. Sci. Eng. C 2011. **31**(2): p. 272-275.

[174] Mohapatra, S. and G.B. Nando, *Chemical modification of natural rubber in the latex stage by grafting cardanol, a waste from the cashew industry and a renewable resource.* Ind. Eng. Chem. Res., 2013. **52**(17): p. 5951-5957.

[175] Aielo, P.B., Borges, F.A., Romeira, K.M., Miranda, M.C.R., Arruda, L.B., L. Filho, P.N., and Drago, B.C.; Herculano, Rondinelli D., *Evaluation of Sodium Diclofenac Release Using Natural Rubber Latex as Carrier.* Materials Research, 2014. **17**: p. 146-152.

[176] Kookarinrat, C. and P. Paoprasert, *Versatile one-pot synthesis of grafted-hydrogenated natural rubber.* Iran. Polym. J., 2015. **24**(2): p. 123-133.

[177] Khairol Anuar, N.K., Tan H.L., Lim, Y.P., Soaib, M.S., and Abu Bakar, N.F., *A review on multifunctional carbon-dots synthesized from biomass waste:*

design/ fabrication, characterization and applications. Front. Energy Res., 2021. **9**(67).

[178] Wang, R., X. Wang, and Y. Sun, *One-step synthesis of self-doped carbon dots with highly photoluminescence as multifunctional biosensors for detection of iron ions and pH.* Sens. Actuators B Chem., 2017. **241**: p. 73-79.

[179] Liu, X., Yang, C., Zheng, B., Dai, J., Yan, L., Zhuang, Z., Du, J., Guo, Y., and Xiao, D., *Green anhydrous synthesis of hydrophilic carbon dots on large-scale and their application for broad fluorescent pH sensing.* Sens. Actuators B Chem., 2018. **255**: p. 572-579.

[180] Liu, W., Li, C., Sun, X., Pan, W., and Wang, J., *Carbon-dot-based ratiometric fluorescent pH sensor for the detections of very weak acids assisted by auxiliary reagents that contribute to the release of protons.* Sens. Actuators B Chem., 2017. **244**: p. 441-449.

[181] Gupta, V.K., Mergu, N., Kumawat, L.K., and Singh, A.K., *Selective naked-eye detection of Magnesium (II) ions using a coumarin-derived fluorescent probe.* Sensors and Actuators B: Chemical, 2015. **207**: p. 216-223.

[182] Zhang, L., Chen, S., Zhao, Q., and Huang, H., *Carbon dots as a fluorescent probe for label-free detection of physiological potassium level in human serum and red blood cells.* Anal. Chim. Acta, 2015. **880**: p. 130-135.

[183] Wei, W., Xu, C., Ren, J., Xu, B., and Qu, X., *Sensing metal ions with ion selectivity of a crown ether and fluorescence resonance energy transfer between carbon dots and graphene.* Chem. Commun., 2012. **48**(9): p. 1284-1286.

[184] Gohari, H., *Determination of magnesium in blood serum by using carbon paste ion selective electrode based on multi-walled carbon nanotubes and nano silicon.* Anal. Bioanal. Chem., 2016. **1**: p. 001-006.

[185] Zhu, J., Y. Qin, and Y. Zhang, *Magnesium-selective ion-channel mimetic sensor with a traditional calcium ionophore.* Anal. Chem., 2010. **82**(1): p. 436-440.

[186] Kim, D.-Y., S. Shinde, and G. Ghodake, *Colorimetric detection of magnesium (II) ions using tryptophan functionalized gold nanoparticles.* Sci. Rep., 2017. **7**(1): p. 3966.

[187] Lü, H., Zhao, Y., Ma, J., Li, J., Wang, H., and Lu, Z., *Eletrochemical detection of magnesium ions using PVC membrane trapped chlorophyll a molecules.* Mol. Cryst. Liq. Cryst., 2001. **371**(1): p. 391-396.

[188] Sadhanala, H.K., S. Pagidi, and A. Gedanken, *High quantum yield boron-doped carbon dots: a ratiometric fluorescent probe for highly selective and sensitive detection of Mg^{2+} ions.* J. Mater. Chem. C, 2021. **9**(5): p. 1632-1640.

[189] Kim, D.-Y., S. Shinde, and G. Ghodake, *Colorimetric detection of magnesium (II) ions using tryptophan functionalized gold nanoparticles.* Scientific Reports, 2017. **7**(1): p. 3966.

[190] Sadhanala, H.K., S. Pagidi, and A. Gedanken, *High quantum yield boron-doped carbon dots: a ratiometric fluorescent probe for highly selective and sensitive detection of Mg^{2+} ions.* Journal of Materials Chemistry C, 2021. **9**(5): p. 1632-1640.

[191] Selvakumar, M., Krishna Bhat, D., Manish Aggarwal, A., Prahladh Iyer, S., Sravani, G., *Nano ZnO-activated carbon composite electrodes for supercapacitors.* Physica B: Condensed Matter, 2010. **405**(9): p. 2286-2289.

[192] Sowa, H. and H. Ahsbahs, *High-pressure X-ray investigation of zincite ZnO single crystals using diamond anvils with an improved shape.* Journal of Applied Crystallography - J APPL CRYST, 2006. **39**: p. 169-175.

[193] Bindu, P. and S. Thomas, *Estimation of lattice strain in ZnO nanoparticles: X-ray peak profile analysis.* Journal of Theoretical and Applied Physics, 2014. **8**(4): p. 123-134.

[194] Wang, S., D.-S. Yang, and F. Yang, *Nitrogen-induced shift of photoluminescence from green to blue emission for xylose-derived carbon dots.* Nano Express, 2020. **1**(2): p. 020018.

[195] Nallayagari, A.R., Sgreccia, E., Pizzoferrato, R., Cabibbo, M., Kaciulis, S., Bolli, E., Pasquini, L., Knauth, P., and Di Vona, M.L., *Tuneable properties of carbon quantum dots by different synthetic methods.* Journal of Nanostructure in Chemistry, 2021.

[196] Zhao, Y., Hao, M., Wang, Y., Sha, Y., and Su, L., *Effect of electrolyte concentration on the capacitive properties of NiO electrode for supercapacitors.* Journal of Solid State Electrochemistry, 2016. **20**(1): p. 81-85.

[197] Zhang, X., Wang, X., Jiang, L., Wu, H., Wu, C., and Su, J., *Effect of aqueous electrolytes on the electrochemical behaviors of supercapacitors based on hierarchically porous carbons.* Journal of Power Sources, 2012. **216**: p. 290-296.

[198] Sathiya, M., Prakash, A. S., Ramesha, K., Tarascon, J−M., and Shukla, A. K., *V_2O_5-Anchored Carbon Nanotubes for Enhanced Electrochemical Energy Storage.* Journal of the American Chemical Society, 2011. **133**(40): p. 16291-16299.

[199] Li, L., Zhang, N., Zhang, M., Zhang, X., and Zhang, Z., *Flexible $Ti_3C_2T_x$/PEDOT:PSS films with outstanding volumetric capacitance for asymmetric supercapacitors.* Dalton Transactions, 2019. **48**(5): p. 1747-1756.

[200] Aristov, N. and A. Habekost, *Cyclic Voltammetry - A Versatile Electrochemical Method Investigating Electron Transfer Processes.* World Journal of Chemical Education, 2015. **3**(5): p. 115-119.

[201] Supchocksoonthorn, P., Thongsai, N., Wei, W., Gopalan, P., and Paoprasert, P., *Highly sensitive and stable sensor for the detection of capsaicin using electrocatalytic carbon dots grafted onto indium tin oxide.* Sensors and Actuators B: Chemical, 2021. **329**: p. 129160.

[202] Liu, J., Wang, J., Xu, C., Jiang, H., Li, C., Zhang, L., Lin, J., and Shen, Z.X, *Advanced Energy Storage Devices: Basic Principles, Analytical Methods, and Rational Materials Design.* Advanced Science, 2018. **5**(1): p. 1700322.

[203] Shao, J., Zhou, X., Liu, Q., Zou, R., Li, W., Yang, J., and Hu, J., *Mechanism analysis of the capacitance contributions and ultralong cycling-stability of the isomorphous MnO_2@MnO_2 core/shell nanostructures for supercapacitors.* Journal of Materials Chemistry A, 2015. **3**(11): p. 6168-6176.

[204] Lee, Y.-S. and K.-S. Ryu *Study of the lithium diffusion properties and high rate performance of $TiNb_6O_{17}$ as an anode in lithium secondary battery*. Scientific reports, 2017. **7**, 16617.

[205] Liu, X., Zhai, Z.-Y., Chen, Z., Zhang, L.-Z., Zhao, X.-F., Si, F.-Z., and Li, J.-H., *Engineering Mesoporous NiO with Enriched Electrophilic Ni^{3+} and O^- toward Efficient Oxygen Evolution.* Catalysts, 2018. **8**(8).

APPENDICES

APPENDIX A

POLYURETHANE-DERIVED CARBON DOTS AS Ni^{2+} SENSOR

Calculation of adsorbent capacity

Diameter of carbon dots $\approx$ 4 nm $\therefore$ Radius of carbon dots $\approx$ 2 nm

$$\therefore \text{Area} = 4\pi R^2 = 4\pi(2^2) = 50.27\ \text{nm}^2/\text{carbon dot}$$

From experiment: 2 mL of Ni^{2+} and 2 mL of carbon dots (0.05 mg·mL^{-1})

The saturation concentration of Ni^{2+} on carbon dots in 200 µM

$$\text{Number of } Ni^{2+}\text{ions} = (200 \times 10^{-6}\text{M})(2 \times 10^{-3}\ \text{L})\left(6.03 \times 10^{23}\ \frac{\text{ions}}{\text{mol}}\right)$$

$$= 2.41 \times 10^{17}\ \text{ions}$$

$$\text{Weight of carbon dots} = \left(0.05\ \frac{\text{mg}}{\text{mL}}\right)(2\ \text{mL}) = 0.1\ \text{mg}$$

Assuming

$$\text{Density of carbon dots} \approx \text{Density of graphite} = 2.26\ \frac{\text{g}}{\text{cm}^3}$$

$$2.26\ \frac{\text{g}}{\text{cm}^3} = \frac{0.1 \times 10^{-3}\text{g}}{(\text{number of carbon dots}) \times \frac{4}{3}\pi(2 \times 10^{-7}\ \text{cm})^3}$$

$$\text{Number of carbon dots} = 1.32 \times 10^{15}\ \text{particles}$$

$$\text{Surface coverage}\left(\frac{\text{ions}}{\text{nm}^2}\right) = \frac{2.41 \times 10^{17}\ \text{ions}}{(1.32 \times 10^{15}\ \text{particles})(50.27\ \text{nm}^2)} = 3.63\ \text{ions/nm}^2$$

$$\text{Adsorption capacity}\left(\frac{\text{mg}}{\text{g}}\right) = \frac{\text{Weight of } Ni^{2+}}{\text{Weight of carbon dots}}$$

$$= \frac{(200 \times 10^{-6}\text{M})(2 \times 10^{-3}\ \text{L})(58693\ \frac{\text{mg}}{\text{mol}})}{0.1 \times 10^{-3}\ \text{g}} = 234.8\ \frac{\text{mg}}{\text{g}}$$

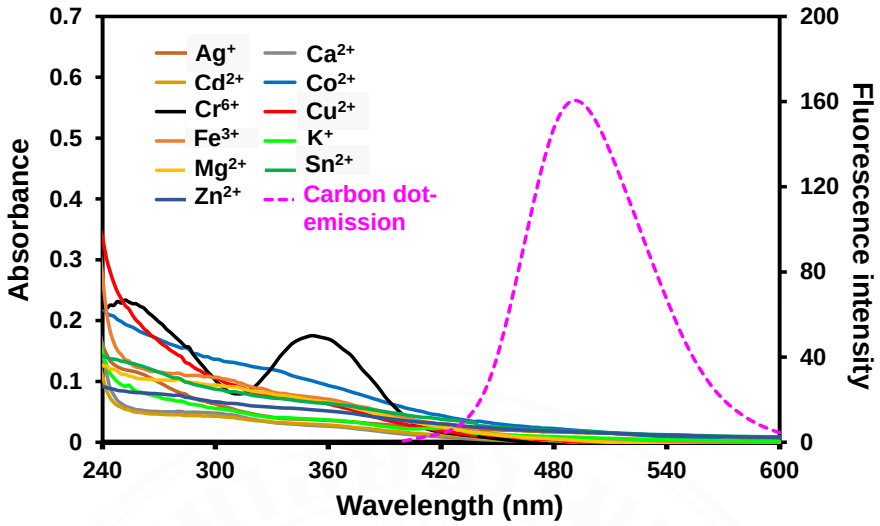

Figure A1. UV-vis absorption of metal ions and fluorescence emission spectrum of carbon dots.

BIOGRAPHY

Name	Kulpriya Phetcharee
Educational Attainment	2017: Bachelor of Science (Chemistry), Thammasat University, Thailand
Scholarship	2019-2022: The Thailand Graduate Institute of Science and Technology (TGIST: SCA-CO-2559-2322-TH), National Science and Technology Development Agency (NSTDA).

Publications

Kulpriya Phetcharee, Natee Sirisit, Penphitcha Amonpattaratkit, Jedsada Manyam, and Peerasak Paoprasert. High-performance Mg^{2+} sensors based on natural rubber-derived, label-free carbon dots. ChemistrySelect.

Kulpriya Phetcharee, Natee Sirisit, Jedsada Manyam, Peerasak Paoprasert. Highly sensitive Ni^{2+} sensors based on polyurethane-derived, label-free carbon dots with high adsorption capacity. ChemistrySelect, 2021, 6(31), 7964-7971.